NKS-418
ISBN 978-87-7893-507-6

Barsebäck as a Research and Development Platform, Extraction and Analysis of Service-aged and Irradiated Reactor Pressure Vessel Material

Pål Efsing[1,4]
Magnus Boåsen[1]
Ulla Ehrnstén[2]
Sebastian Lindqvist[2]
Mattias Thuvander[3]
Kristina Lindgren[3]
Jenny Roudén[4]

[1] Department of Solid Mechanics, Royal Institute of Technology (KTH)
SE-10044 Stockholm Sweden
[2] VTT Technical Research Centre of Finland Ltd, PO Box 1000
FI-02044 VTT, Helsinki, Finland
[3] Chalmers University of Technology, Department of Physics
SE-41296, Göteborg, Sweden
[4] Ringhals AB, SE-43285 Väröbacka, Sweden

February 2019

Abstract

As part of the NKS-R program, VTT, Chalmers University of Technology and KTH has performed a baseline study to analyze the as-aged material properties of the retired reactor pressure vessel, RPV, from Barsebäck unit 2. The current phase included the actual extraction of samples from the RPV of Barsebäck 2, formulation of a preliminary test matrix and continued work to set the scope for future R&D activities related to fracture mechanical testing and microstructural evaluation of aged low alloy steel typical of the operating nuclear power plants in the Nordic countries. Due to the nature of the work, the NKS-project is connected to a number of adjacent activities, including support from the Finnish Nuclear Safety Program, the SAFIR-program, the Swedish Radiation Safety Authority SSM and Swedish Centre for Nuclear Technology, SKC and Energiforsk.

In 2018, base-line microstructural work was finalized of using Light Optical, Scanning Electron and Transmission Electron methodologies to complement the previous high resolution Atom Probe Tomography work. Further the preparation of the mechanical testing of the retrieved samples have proceeded. A literature review of constraint effects on fracture mechanical testing and a suggested preliminary test matrix has also been presented.

Kristina Lindgren, Chalmers University of Technology successfully defended her Ph.D. thesis performed with-in the scope of the project in December 2018.

Key words

Low alloy steel, irradiation effects, fracture toughness, ductile to brittle transition temperature, constraint effects, high resolution microscopy, microstructural characterization

NKS-418
ISBN 978-87-7893-507-6
Electronic report, February 2019

NKS Secretariat
P.O. Box 49
DK - 4000 Roskilde, Denmark
Phone +45 4677 4041
www.nks.org
e-mail nks@nks.org

Barsebäck as a Research and Development Platform, Extraction and Analysis of Service-aged and Irradiated Reactor Pressure Vessel Material

Final Report from the NKS-R BREDA-RPV 2018 activity

(Contract: NKS_R_2016_118)

Pål Efsing[1,4], Magnus Boåsen[1]
Ulla Ehrnstén[2], Sebastian Lindqvist[2]
Mattias Thuvander[3], Kristina Lindgren[3]
Jenny Roudén[4]

[1] Department of Solid Mechanics, Royal Institute of Technology (KTH), SE-100 44 Stockholm Sweden
[2] VTT Technical Research Centre of Finland Ltd, PO Box 1000, FI-02044 VTT, Espoo, Finland
[3] Chalmers University of Technology, Department of Physics, SE-412 96, Göteborg, Sweden
[4] Ringhals AB, SE-43285 Väröbacka, Sweden

Table of contents

1. Introduction

As part of the NKS-R program in 2018, VTT, Chalmers University of Technology, and KTH have continued the efforts outlined in the summary report from 2016 [Efsing et al. 2016] regarding extraction, mechanical and microstructural testing, and analysis of materials from a retired reactor pressure vessel, RPV. The objective of the study is to increase the current knowledgebase on correctness of the existing surveillance programs, as well as the influence of long time thermal ageing of the materials. During 2016, a baseline study to prepare the basis for a test program to analyze the as-aged material properties of the RPV from Barsebäck unit 2 was performed. During 2017 the progress of the program mainly concerned the extraction methodology. This part of the work has been fully financed by Ringhals AB, Forsmark Kraftgrupp AB and OKG AB as part of an umbrella project under the auspices of Energiforsk with Monika Adsten as the primary program manager. During 2018 the actual extraction of the material took place with follow on activities related to obtaining the permission from the Swedish and Finnish radiation protection authorities to allow for shipping of the specimens from Sweden to Finland for mechanical testing.

In 2018 three deliverables of the preparatory actions have been completed and published. The reports are appended to this report.

The key deliverable during BREDA-RPV 2018 is the preliminary test matrix which is the suggested scope for testing of the aged material [Boåsen 2019]. In addition to this, a literature review of the state of the art regarding constraint effects and fracture toughness has been prepared [Lindqvist 2018] as well as a baseline study of the microstructural features in un-irradiated material of the material that will be studied later [Tapper 2019]. The sum of these reports lay a firm foundation for future work with the irradiated and thermally aged material.

The key project milestone for 2018 was the extraction of the samples from the RPV at Barsebäck. This was completed in the first half of 2018. After this, the samples have been transported to Ringhals for activity measurements and removal of the stainless steel cladding on the inner surface. The objective for the removal of the cladding is to minimize the dose during both future transports and testing of the material. The samples are ready to be shipped from Ringhals to VTT when the permits from the national regulatory safety commissions, the SSM and STUK are completed and the hot-cell laboratory of VTT can receive the samples. Samples to be investigated by high resolution microscopy/atom probe tomography have been extracted while the samples were at Ringhals and will be transported to Chalmers when the appropriate permits have been obtained.

An important part of the project is be part of the knowledge build-up and retainment of a new generation of researchers in the field. Three Ph.D. students have been financed by the BREDA-program and the adjacent SAFIR, SSM, SKC and Energiforsk programs. The first Ph. D. student, Kristina Lindgren, defended her thesis successfully in December 2018 at Chalmers University of Technology [Lindgren 2018] and is currently part of the program in a post-doctoral position to complete the remaining parts of the high resolution microscopy study.

2. Literature review on Constraint and Fracture toughness

The report [Lindqvist 2018] lays a firm foundation for the mechanical testing by gathering and critically reviewing the current state of the art regarding constraint effects on fracture mechanical testing. It includes a description of the different constraint parameters and the

effect of constraint on fracture toughness. Engineering friendly methods for assessing the effect of constraint on the reference temperature T_0 are presented. The constraint difference between an elliptical surface crack and conventional fracture toughness specimens was estimated to cause a 25-30 °C shift in T_0.

Additionally, two models for predicting the cumulative probability of failure by cleavage fracture are briefly reviewed and applied to datasets from the open literature. This shows the generally better predictions of the experiments of the non-local weakest link model at constant temperatures. But as the master curve methodology carries the capability of making predictions across varying temperatures it is used in the final estimation of specimen size and temperature requirements for fracture testing of constraint effects. Potential risks related to testing such as pre-cracking problems and bimodal tendencies are also addressed in this report.

It was found that C(T) and SEN(B) specimens as high and low constraint configurations of size W = 10 mm and B = 5 mm will most likely be appropriate for testing of the constraint effects on fracture toughness in the case of a limited availability of material.

The full report is found in Appendix 1.

3. Preliminary mechanical test matrix for the BREDA/BRUTE project

The report [Boåsen 2019] outlines the proposed test matrix for evaluating the effect of irradiation and thermal ageing on the mechanical properties of service-aged RPV-material. It is proposed that the test matrix includes testing of miniature Compact Tension, C(T), and Single Edge Notch Bend, SE(B) specimens to evaluate ductile and cleavage fracture behaviour and the influence of constraint on the mechanical properties. In addition to this the proposed testing will include Charpy-V impact test specimens, microstructural samples, hardness measurements and tensile test specimens to fully categorize the mechanical properties of the aged material.

The report further outlines the use of the trepans cut from the RPV and how the material sampling is suggested to proceed.

The full report is appended to this report as Appendix 2.

4. Microstructural characterization on non-irradiated Barsebäck RPV material: Transmission electron microscopy study

In order to produce a baseline of the microstructure to the material that is extracted from the RPV, un-irradiated samples from the archive material of the RPV-welds were studied using Scanning and Transmission electron microscopy. The study has verified the occurrence of four different types of particles that were observed and characterized based on size distribution and composition. The objective is to be able to compare to the microstructure of the samples collected from the actual RPV, and to the particles initiating brittle fracture.

The full report is appended to this report as Appendix 3.

5. Conclusions

Samples have been extracted from the RPV of Barsebäck Unit 2 to allow for testing of the mechanical and microstructural properties of service-aged material. The results will be

compared to data from the surveillance program of the RPV. Two important mile-stones of the project were completed in 2018, i.e. the extraction of the material from the RPV in Barsebäck, and the preparation of a preliminary test matrix for the material once it has been transported to VTT.

The current state of the art regarding the influence of constraint on fracture properties have been summarized and reviewed with the objective to lay a firm foundation for the envisaged testing.

Unirradiated samples have been further analysed microstructurally to complete the baseline testing, encompassing methods from light optical microscopy to atom probe tomography, thus enabling a comprehensive basis to understand the as-irradiated microstructure in the following steps.

Kristina Lindgren successfully defended her thesis in December 2018, thus representing the first Ph.D. thesis involving the material from the BREDA-project.

6. References

Boåsen M. et. al, Preliminary mechanical test matrix for the BREDA-BRUTE project, VTT Research Report VTT-R-06849-18, 2019, 24 pages

Efsing P et al., Barsebäck as research and development platform, extraction and analysis of reactor pressure vessel material, Final report for the BREDA2016 activity

Efsing P., Status report – NKS project RPV-BREDA: NKS_R_2016_118, 2018-10-25

Lindgren K., Effects of irradiation and thermal ageing on the nanoscale chemistry of steel welds, Ph.D. Thesis presented at Chalmers University of technology 2018-12-11

Lindqvist S. and Boåsen M., BREDA: Constrain and Fracture, 2018, 41 pages

Tapper U., Microstructural characterization of non-irradiated Barsebäck RPV material: Transmission electron microscopy study, VTT Research report, VTT-R-00041-19, 2019, 16 pages

Acknowledgements

NKS conveys its gratitude to all organizations and persons who by means of financial support or contributions in kind have made the work presented in this report possible.

The support from the Finnish nuclear safety program, the SAFIR2018-program, the Swedish Radiation Safety Authority and the Swedish Centre for Nuclear Technology, SKC and finally the Swedish Nuclear Power Plants permit holders and owners (Ringhals AB, Forsmarks Kraftgrupp AB, OKG AB, Vattenfall AB and Uniper) for the work is gratefully acknowledged. Some of the adjacent work is part of a research program coordinated by Energiforsk with Monika Adsten as the program manager

Disclaimer

The views expressed in this document remain the responsibility of the author(s) and do not necessarily reflect those of NKS. In particular, neither NKS nor any other organization or body supporting NKS activities can be held responsible for the material presented in this report.

Appendices

1. Boåsen M. et. al, Preliminary mechanical test matrix for the BREDA-BRUTE project, VTT Research Report VTT-R-06849-18, 2019, 24 pages

2. Lindqvist S. and Boåsen M., BREDA: Constraint and Fracture, 2018, 41 pages

3. Tapper U., Microstructural characterization of non-irradiated Barsebäck RPV material: Transmission electron microscopy study, VTT Research report, VTT-R-00041-19, 2019, 16 pages

Bibliographic Data Sheet **NKS- 418**

Title	Barsebäck as a Research and Development Platform, Extraction and Analysis of Service-aged and Irradiated Reactor Pressure Vessel Material
Author(s)	Pål Efsing[1,4], Magnus Boåsen[1] Ulla Ehrnstén[2], Sebastian Lindqvist[2] Mattias Thuvander[3], Kristina Lindgren[3] Jenny Roudén[4]
Affiliation(s)	[1] Department of Solid Mechanics, Royal Institute of Technology (KTH), SE-10044 Stockholm Sweden [2] VTT Technical Research Centre of Finland Ltd, PO Box 1000, FI-02044 VTT, Helsinki, Finland [3] Chalmers University of Technology, Department of Physics, SE-41296, Göteborg, Sweden [4] Ringhals AB, SE-43285 Väröbacka, Sweden
ISBN	978-87-7893-507-6
Date	February 2019
Project	NKS-R / BREDA-RPV
No. of pages	8
No. of tables	0
No. of illustrations	0
No. of references	6

Abstract
max. 2000 characters

As part of the NKS-R program, VTT, Chalmers University of Technology and KTH has performed a baseline study to analyze the as-aged material properties of the retired reactor pressure vessel, RPV, from Barsebäck unit 2. The current phase included the actual extraction of samples from the RPV of Barsebäck 2, formulation of a preliminary test matrix and continued work to set the scope for future R&D activities related to fracture mechanical testing and microstructural evaluation of aged low alloy steel typical of the operating nuclear power plants in the Nordic countries. Due to the nature of the work, the NKS-project is connected to a number of adjacent activities, including support from the Finnish Nuclear Safety Program, the SAFIR-program, the Swedish Radiation Safety Authority SSM and Swedish Centre for Nuclear Technology, SKC and Energiforsk.

In 2018, base-line microstructural work was finalized of using Light

Optical, Scanning Electron and Transmission Electron methodologies to complement the previous high resolution Atom Probe Tomography work. Further the preparation of the mechanical testing of the retrieved samples have proceeded. A literature review of constraint effects on fracture mechanical testing and a suggested preliminary test matrix has also been presented.

Kristina Lindgren, Chalmers University of Technology successfully defended her Ph.D. thesis performed with-in the scope of the project in December 2018.

Key words

Low alloy steel, irradiation effects, fracture toughness, ductile to brittle transition temperature, constraint effects, high resolution microscopy, microstructural characterization

RESEARCH REPORT

VTT-R-06849-18

Preliminary mechanical test matrix for the BREDA/BRUTE-project

Authors: Magnus Boåsen[b], Sebastian Lindqvist[a] Jari Lydman[a], Pentti Arffman[a], Pål Efsing[b,c], Jenny Rouden[c], Ulla Ehrnstén[a]

[a]*VTT Technical Research Centre of Finland Ltd, PO Box 1000, FI-02044 VTT*

[b]*Department of Solid Mechanics, Royal Institute of Technology (KTH), SE-100 44 Stockholm Sweden*

[c]*Ringhals AB, 432 85 Väröbacka*

Confidentiality: Restricted to SAFIR2018

Report's title	
Preliminary mechanical test matrix for the BREDA-BRUTE project	
Customer, contact person, address SAFIR2018, RG6 State Nuclear Waste Management Fund (VYR) and VTT Technical research Centre of Finland Ltd	**Order reference** Dno 33/2018
Project name Barsebäck RPV material used for true evaluation of embrittlement	**Project number/Short name** 118066 /BRUTE2018
Author(s) Sebastian Lindqvist, Magnus Boåsen, Jari Lydman, Pentti Arffman, Pål Efsing, Jenny Roudén, Ulla Ehrnstén	**Pages** 24/
Keywords Pressure vessel, mechanical testing, Barsebäck RPV	**Report identification code** VTT-R-06849-18

Summary

The test matrix comprise of miniature C(T) and SE(B) specimen for cleavage, ductile fracture and constraint testing, Charpy-V specimens for impact testing, tensile specimens for the main objective of the BRUTE (Barsebäck RPV material used for true evaluation of embrittlement) project is to determine the mechanical and microstructural properties of Barsebäck 2 reactor pressure vessel (RPV) weld in accordance with the objectives set out in the BREDA (Barsebäck REsearch&Development Arena) project. This document describes the current plans for mechanical testing of the materials included in the project, i.e., trepans removed from the Barsebäck 2 RPV beltline region and head as well as surveillance material and accelerated irradiated material. The test matrix is preliminary to enable adjustments based on results gained. Also the extent of mechanical testing need prioritisation and adjustment during the course of the project, to make the most with the materials available with the resources available.

The test matrix comprise of miniature C(T) and SE(B) specimen for cleavage, ductile fracture and constraint testing, Charpy-V specimens for impact testing, tensile specimens for mechanical properties determination in addition to slide-slabs for hardness and microstructural investigation.

Of the eight trepans included in this test matrix it is possible to perform more than 1500 mechanical tests.

Confidentiality	Confidential

Stockholm 10.1.2019

Written by	Reviewed by	Accepted by
Magnus Boåsen PhD student, KTH	Ulla Ehrnstén Principal Scientist	Sami Penttilä Research Team Leader

VTT's contact address
Kivimiehentie 3, PO Box 1000, 02044 VTT

Distribution (customer and VTT)
SAFIR2018 RG6, authors, BREDA advisory board, VTT nuclear materials database, VTT archive (signed paper version)

Preface

The main objective of the BRUTE (Barsebäck RPV material used for true evaluation of embrittlement) project is to determine the mechanical and microstructural properties of Barsebäck 2 reactor pressure vessel (RPV) weld in accordance with the objectives set out in the BREDA (Barsebäck REsearch&Development Arena) project. This document describes the current plans for mechanical testing of the materials included in the project, i.e., trepans removed from the Barsebäck 2 pressure vessel beltline region and head as well as surveillance material and accelerated irradiated material. The test matrix is preliminary to enable adjustments based on results gained. Also the extent of mechanical testing need prioritisation and adjustment during the course of the project, to make the most with the materials available with the resources available.

This document is Deliverable 3.2 in the BRUTE project.

Espoo 10.1.2019

Authors

Contents

1. Introduction

Barsebäck 2 (B2) was a boiling water reactor (BWR) that started operation in 1977 and was decommissioned in 2005. Following this, the BREDA project (Barsebäck REsearch&Development Arena) was initiated in 2016 with the purpose to assess the ageing of the reactor pressure vessel (RPV). In the BREDA project, cylindrical trepans with a diameter of 200 mm were extracted from beltline welds subjected to a neutron irradiation from the beltline as well as from welds from the RPV head. This extraction was completed during 2018. The BRUTE project (Barsebäck RPV material used for true evaluation of embrittlement) was launched in 2018 as part of the SAFIR2018 programme, and an application for its continuation in the SAFIR2022 programme has been submitted. BRUTE is a project pioneering the new infrastructure of the Centre for Nuclear Safety (CNS) at VTT, Technical Research Centre of Finland, by performing investigations (mechanical and microstructural) on the B2 trepans in accordance with the objectives of the BREDA project.

Ensuring safe operation and the life time of the RPV is one of the most important tasks for nuclear power plants (NPPs). The RPV is regarded as a non-replaceable component, which thus means that condition of the RPV must be known to ensure safe nuclear power production. Furthermore, fracture of the RPV is not acceptable and must be prevented. Radiation-induced embrittlement the most pronounced ageing mechanism of the RPV base materials and especially of the welds in the beltline region. This causes an increase in the ductile to brittle transition temperature (DBTT). The DBTT must have a safety margin with respect to the lowest possible operating temperature and pressure of the RPV in connection, e.g., to an emergency scenarios. The embrittlement is monitored through a surveillance program, in which mechanical test specimens are placed in the reactor at a position with higher fast neutron flux than the RPV, i.e., with a lead factor. A prognosis of the RPV behaviour is made based on the mechanical test results obtained from these specimens and internationally available data, and this is used in the safety assessment to ensure safe NPP operation.

Traditionally, impact testing has been the backbone of surveillance programs. As the methods and applicability of fracture toughness has developed since commissioning of the earliest generations of NPPs, more analyses using fracture toughness as the material property is used in the structural integrity analyses for the RPV. No fracture toughness specimens were, though, inserted in the earliest surveillance capsules. With today's experimental techniques it is possible to re-constitute specimens from already tested specimens into sub-sized specimens or use miniature specimens without reconstitution, from which fracture toughness can be measured and it is then possible to back-fit data in order to study the evolution of fracture toughness over irradiation time.

Several of the Nordic NPP RPVs, including the B2 RPV, has been welded using a high-Ni, high-Mn weld filler material, which in the 70s and early 80s rightfully was considered to be a good choice to achieve good initial properties with good toughness and low ductile to brittle temperature, while the understanding of the role of especially Ni on the embrittlement rate was not well developed. Since then, a high Ni-content has been observed to enhance the embrittlement caused by radiation.

The BREDA and BRUTE-projects presents a unique opportunity for material characterization in terms of correlating the testing within the surveillance program to that of the actual RPV, correlating results from different tests (especially impact and fracture toughness testing) as well as to investigate other key research questions pertaining to materials and structural integrity research, especially for Nordic RPVs. One of these questions is the role of the constraint effect on fracture toughness and its relation to ageing/embrittlement.

The objectives of the mechanical test programme within the BREDA/BRUTE project are the following:

- Investigating the transferability between the fracture toughness properties of the RPV and the surveillance test specimens.
- Understanding the effect of flux and fluence on the shift in ductile-to-brittle transition temperature.
- Understanding the effect of irradiation embrittlement on the fracture mechanical crack tip constraint.
- Identifying the factors affecting the fracture toughness properties in thickness direction.
- Determining the shift in ductile-to-brittle transition temperature due to thermal embrittlement versus the shift due to the combined effect of thermal embrittlement and irradiation.

Through the experimental work conducted in BREDA/BRUTE, a better understanding is obtained of the above mentioned issues.

The outline of this report is as follows: First, in Section 2a description of the available materials from B2 is given, trepans and surveillance specimens. Section 3 gives a brief overview of the mechanical test methods that are to be used to fulfil the test matrix. Section 4 gives a brief overview of the microstructural methods that are to be used for characterizing the materials. The content of Section 5 describes specimen extraction and related cutting of the trepans, and presents a preliminary specimen cut out plan. Finally, the preliminary test matrix and priority of testing is presented in Section 6.

The mechanical test matrix presented in this document is designated as preliminary, to allow for possible changes based on results and only fine tuning is foreseen during the progress of the project. Also the extent of mechanical testing need prioritisation and adjustment during the course of the project, to make the most with the materials available with the resources available.

2. Overview of the available materials

The BRUTE project includes three types of materials, i.e., B2 trepans, surveillance material and material, which has been irradiated in an accelerated manner to high fluence, mimicking about 300 years of B2 operation.

The B2 RPV has an inner diameter of 5.2 m, a total height of 20.8 m, and a weight of 520 t. The nominal wall thickness of the RPV varies between about 126 and 70 mm, being thinner in the head region compared to the beltline region. Preliminary measurements of the trepans show that the wall thickness in the beltline regions is about 130 mm. The B2 RPV is made from plates (i.e., not forged rings as later RPVs) made from SA 533 Gr B Cl. 1 material and has been welded using submerged arc welding using a weld filler metal which is high in Mn and Ni, similar to e.g. B1, O2, O3, Ol1, Ol2, F1, F2, F3, R3 and R4. The chemical composition of the B2 and some other RPV weld metals is presented in Table 1.

Table 1. Chemical composition of B2 and some other RPV weld metals (wt-%).

Plant	C	Si	Mn	P	S	Cr	Mo	Ni	Cu	Co
B2	0.084	0.22	**1.53**	0.011	0.004	0.13	0.45	**1.47**	0.064	0.008
R3	0.052	0.21	**1.46**	0.009	0.006	0.07	0.50	**1.58**	0.08	0.015
R4	0.068	0.14	**1.35**	0.015	0.004	0.04	0.50	**1.66**	0.05	0.010
Ol2	0.052	0.26	**1.28**	0.005	0.018	0.07	0.47	**1.32**	0.09	0.020

The weld is an X-weld, i.e. the welding has been performed from both sides. The root of the first weld has been removed before welding the second weld, and thus the X-weld does not contain a weld root, but only a change in the welding orientation. An example of an X-weld can be seen in Figure 1. The maximum width of the weld is about 35 mm, and the minimum about 25 mm. These measures must be confirmed from the trepans before cutting, as they may wary from trepan to trepan.

When the surveillance samples were manufactured, blanks were cut from welded plate blocks similar to the RPV weld. The surveillance impact test specimens with 10x10x55 mm dimensions, have been cut perpendicular to the inner surface of the RPV/block. Thus, they all contain base material in addition to weld metal, the amount of which is dependent on at which depth of the plate the blanks were cut, and thus the width of the weld at this location.

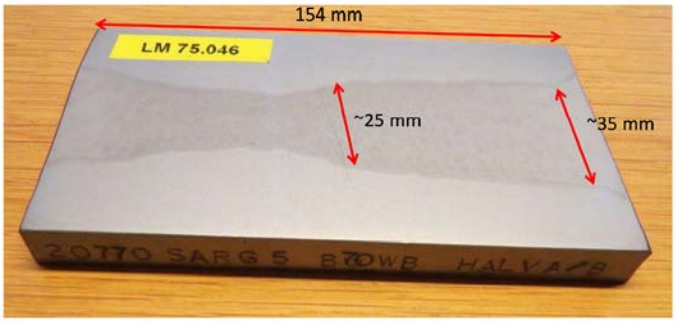

Figure 1. A macrograph of a weld specimen done before welding of the actual RPV, showing the nominal dimensions of the B2 weld [3]

Totally 14 trepans have been removed from the B2 RPV, as depicted in Figure 2, i.e., four from the beltline region and 10 from the RPV head region. Each trepan has a diameter of about 197 mm, is through-wall, and weighs about 40 kg. Before transport for testing, the inner surface cladding will be removed at the Ringhals site, where the trepans were transported to after removal from the B2 RPV. Details about the trepans are presented in Table 2. Eight trepans, i.e., four from the beltline region and four from the head region are included in the test matrix described in this report.

A detailed plan for marking of the trepans, and all specimens prepared from these will be developed and reported before any cutting is done. However, a decision has been made to identify the trepans with letters, instead of the longer weld and trepan number. The test specimens are small in size, and therefore there is a need to simplify the specimen identification coding as much as possible, though still keeping track of all specimens without a risk of confusion.

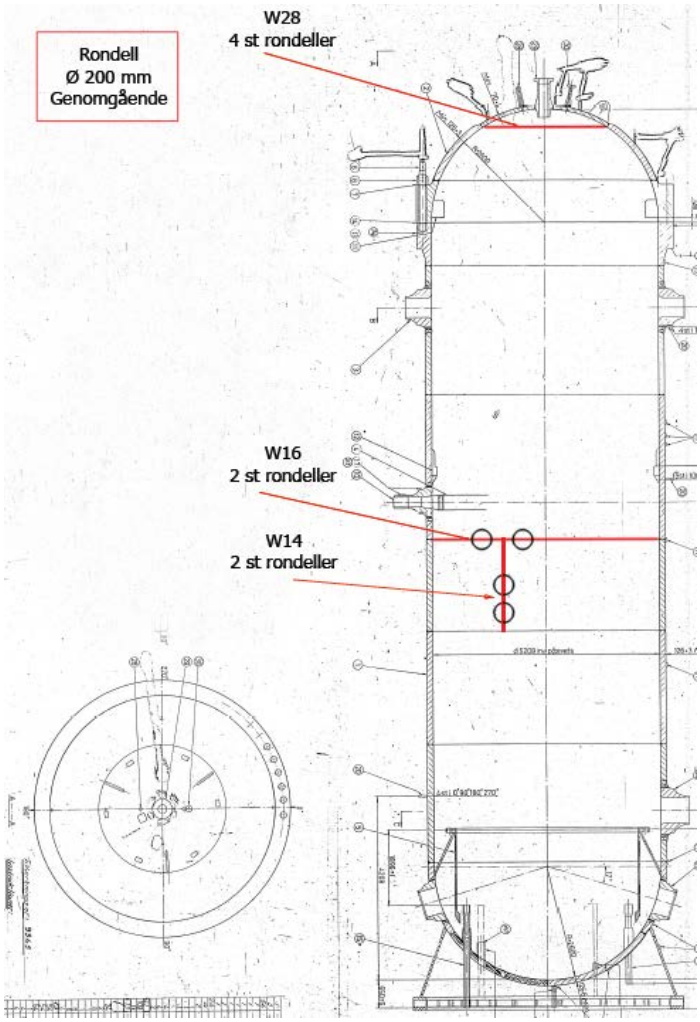

Figure 2. Extraction locations of the trepans

Table 2. Details of the trepans.

Weld	Weld location	Trepan	Identification code for testing	Maximum fluence ϕt/(10^{17} n/cm^2), E>1 MeV
W28	Head, circumferential, upper	W28-1	A	0
W28		W28-2	B	0
W28		W28-3	C	0
W28		W28-4	D	0
W16	Beltline, circumferential	W16-1	E	0.144
W16		W16-2	F	0.290
W14	Beltline, longitudinal	W14-1	G	4.83
W14		W14-2	H	7.94

In addition, 3 untested Charpy-V specimens from chain C are available from the surveillance programme for B2, as well as 3 untested Charpy-V specimens from the accelerated testing campaign, from chain G, as detailed in Table 3. These are utilized in the project to obtain a fracture toughness based trend curve for the B2 surveillance weld metal.

Table 3. Identification information and fluence of the six untested Charpy-V specimens included in the BRUTE project.

Chain	Box	Position in box	Specimen code*	Maximum fluence ϕt/(10^{17} n/cm^2), E>1 MeV
C	B78	G	BGD3	10.2
C	B78	H	BGN3	10.2
C	B78	I	BGF8	10.2
G	B112	G	BGB4	587
G	B112	H	BGJ8	587
G	B112	I	BGM6	587

∗The third letter in the specimen code assigns the weld plate from which the surveillance specimen is cut, while the number assigns the depth of specimen in the weld. This affects also how much weld the ChV specimen includes, being widest in numbers 1 and 9 (about 75%), and shortest in specimens with number 5 (about 25%).

2.1. Consideration for cutting of the trepans

The material has been extracted as cylindrical trepans with a diameter of Ø197 and a thickness that is about 135 mm in the beltline region and less than 80 mm in the RPV head region. The trepans has been extracted from different weldments which are denoted WX-n, where W signifies weld and X signifies the weld number and n is the trepan number, used in this project.

In order to achieve maximum use of the extracted material, it is necessary to carefully plan specimen cut-out from the trepans. As a large part of this project relates to the comparison between the surveillance program and the RPV, it is necessary to follow the outlines of ASTM E185 (Standard Practice for Design of Surveillance Programs for Light-Water Moderated Nuclear Power Reactor Vessels) when preparing the cutting plan for the specimens. The main precaution that needs to be accounted for is the position in the trepan from which the specimens is taken. Related to the base metal, specimens should not be extracted from the mid-thickness region. Regarding the weld metal, specimens may be extracted from any position throughout the weld except for positions within 13 mm of a root or surfaces of the weld. The B2 welds are X-welds, i.e., the welding has been performed from both sides. The root of the first weld has been removed before welding the second weld, and thus the X-weld does not contain a weld root, but only a change is welding orientation.

The consequence of the above for the trepans is interpreted as follows: 13 mm from the inner and outer surfaces of the trepan is not representative of the average weld metal, at least not without confirmation from microstructural and hardness measurements. Confirmation of the representativeness of the area, where the two welds meet, shall also be made before this area is included in the test matrix to represent the weld metal. However, testing of all areas of the materials shall be evaluated. One of the milestones for BRUTE2019 is update the test matrix, and the need to test also the HAZ material shall be evaluated then, based on results from the first trepan, for testing either within BRUTE or in another test programme.

In accordance with the surveillance program standard, the region around $^1/_4$T is reserved for Charpy-V specimens, and this applies here to one of the W28 trepans and all of the other trepans. One of the project goals is, however, to investigate the attenuation of fluence in more detail, and therefore it is optimal to cut as close as reasonable to the inner surface, i.e., at the location of the highest fluence. This should be done on a slice, cut less than 13 mm from the surface, provided that the microstructural and hardness characterisation show that the material is similar to the material at ¼ thickness. Pictures showing the appearance of some of the trepans and how slices can be cut are shown in Figure 3 - Figure 6. Before cutting, the location and size of the weld in each trepans must be identified with millimetre precision. Marks have been made on the outer surface of the RPV at the location of the weld to facilitate the periodic NDE campaigns performed during the NPP operation. This is,

however, not enough as basis for the cutting. Preliminary information from Ringhals indicates that the weld is readily seen on the surface of the trepans after chemical treatment, Figure 5.

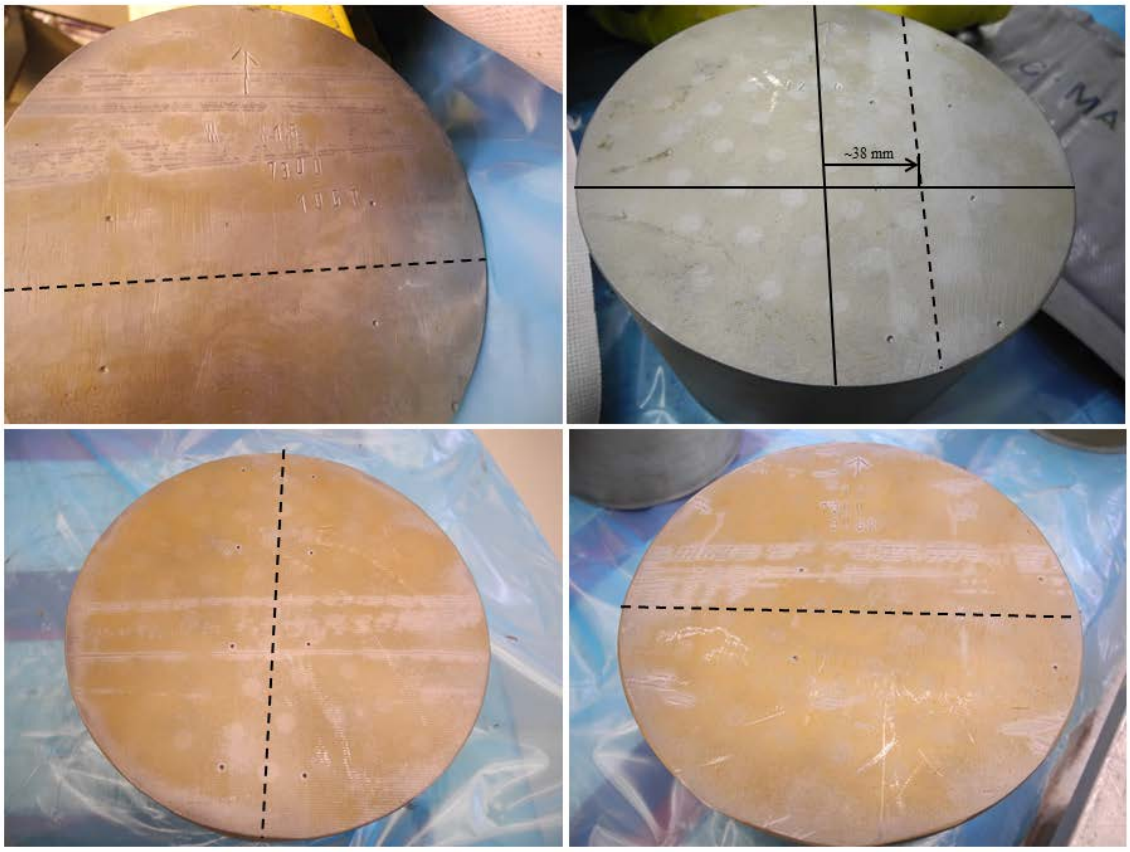

Figure 3. Overview of the trepans extracted from the RPV, dashed line indicates weld position

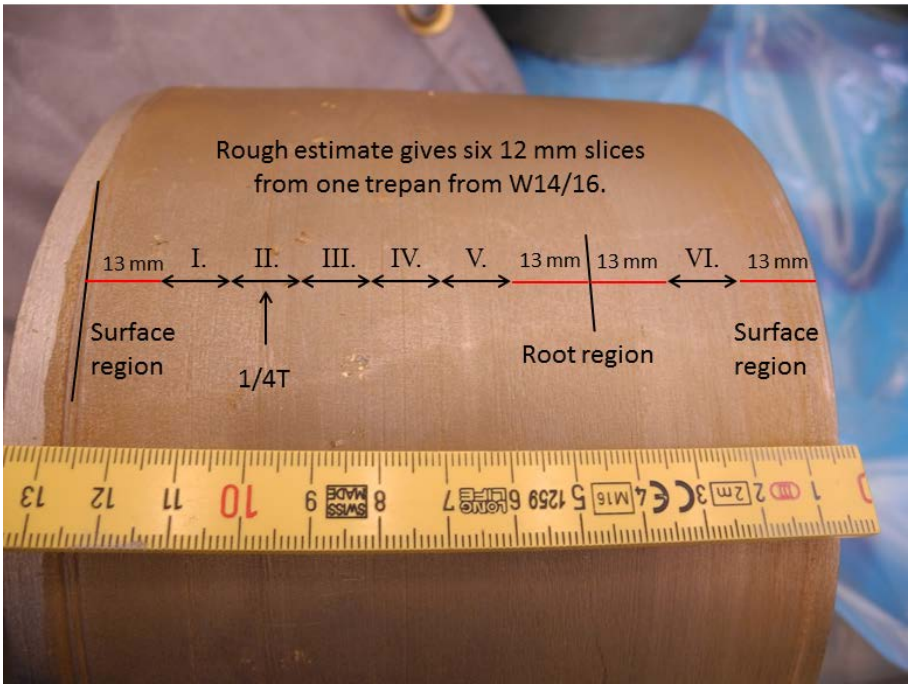

Figure 4. Estimate of the maximum amount of slices that can be manufactured from one RPV trepan

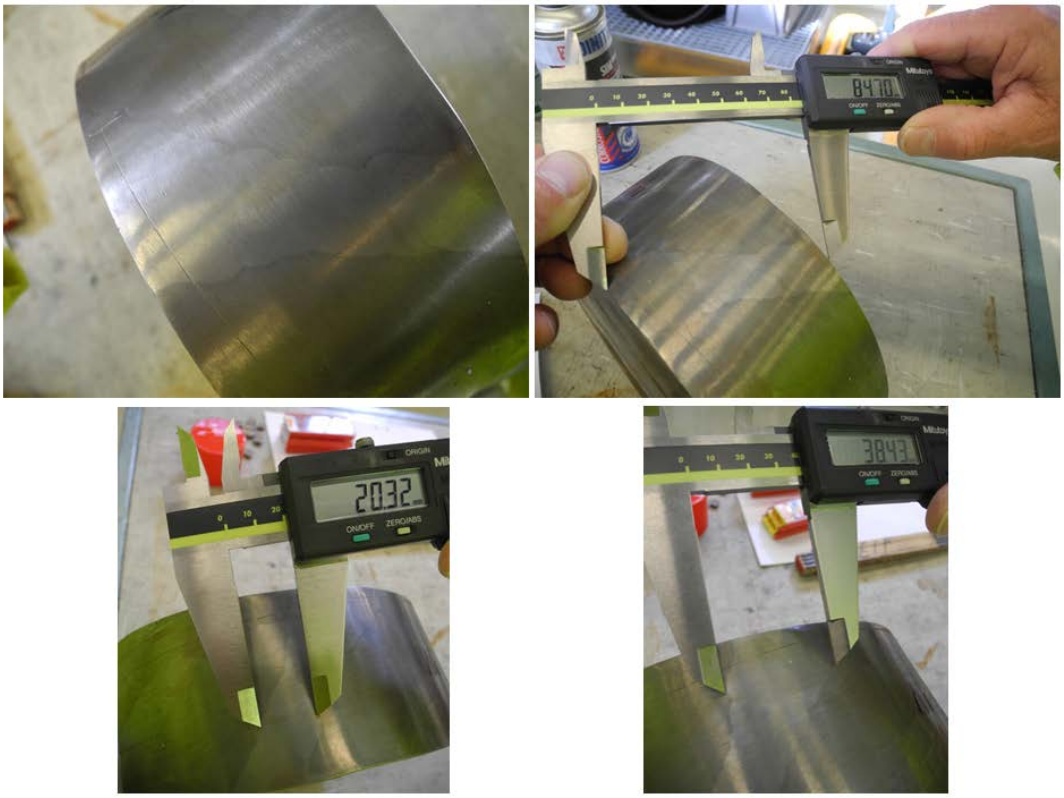

Figure 5. Overview of the trepans extracted from the RPVH, note the inclined weld and the smaller thickness compared to the trepans from the RPV beltline region

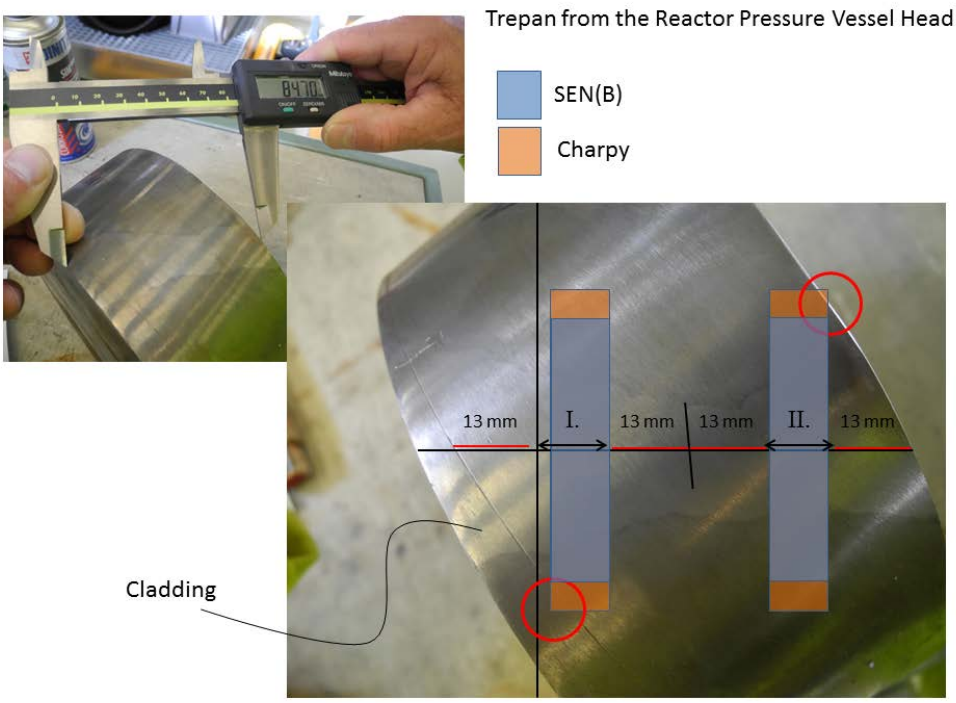

Figure 6. Estimate of slices that can be manufactured from one RPVH trepan

3. Mechanical testing

This section will detail what mechanical properties are planned for testing, with which type of specimens this will done, how many specimens are required for each test type and other requirements there may be on the testing procedure. The purpose of this section is not to detail the testing procedure, but in brief review the reason to and the basic requirements for the testing. The test matrix will be updated in BRUTE2019, based on the results from the first trepan.

3.1. Cleavage fracture testing

Cleavage or brittle fracture is a key issue in the assessment of RPV-integrity. In order to gain insight into the fracture properties of the extracted material, characterizing the cleavage fracture properties is pertinent. This type of testing is carried out using pre-cracked fracture mechanical test specimens, e.g. C(T) or SEN(B) specimens, and is typically characterized according to ASTM E1921. The testing is highly sensitive to temperature and specimen size, so care must be taken in the preparation of specimens and testing procedures. In this project, emphasis will be put on this type of testing and it will be carried out in two manners as described in the following.

1. Testing according to ASTM E1921 in order to find the reference temperature T_0 for ferritic steels in the transition range. This will be carried out by utilizing C(T)-specimens defined by W = 8 mm and B = 4 mm. Testing can be carried out at multiple temperatures per the recommendations in E1921. One key aspect of this testing is to compare the obtained results to results from the surveillance program where C(T)-specimens made from Charpy specimens (from the surveillance and accelerated irradiation programmes) are to be tested for T_0. It is judged that at least 12 valid specimens are needed in order to find T_0, therefore, a good margin would be to have 20 specimens per investigated material state, i.e. base or

weld metal, and fluence level. This testing will be done at several positions throughout the depth of the trepans, each depth corresponding to different fluence level.

2. Testing for ageing effects on the constraint sensitivity on the extracted material. This will be carried out by testing two specimen types with different crack lengths (differing crack tip constraint) at the same testing temperature. The specimen types that will be used are C(T) and SEN(B) defined by W = 10 mm and B = 5 mm, and a/W = 0.5 and a/W = 0.15 respectively. The temperature for testing will be estimated based on the T_0-results from point 1 above. It is pertinent that the testing temperature is chosen so that the measuring capacity of the specimen embraces the estimated toughness distribution. This testing is in all other respects carried out as per the recommendations in ASTM E1921. Tensile tests are required at the temperature of fracture testing in order to model the results in the analysis of the testing. It is judged that around 12-20 specimens will be needed per crack length, resulting in 24-40 specimens per material state, i.e. base or weld metal, and fluence level. It is important to understand that the results from the C(T)-specimens in this type of testing can be used to produce the same results as point 1 above, i.e. this point is an extension of point 1 with the difference that these specimens should be tested at one single temperature. This testing should be done from at least one slice through the depth of the trepan, preferably from two slices.

Specimens intended for use in testing are seen in Figure 7, and details of the cleavage fracture testing are summarised in Table 4.

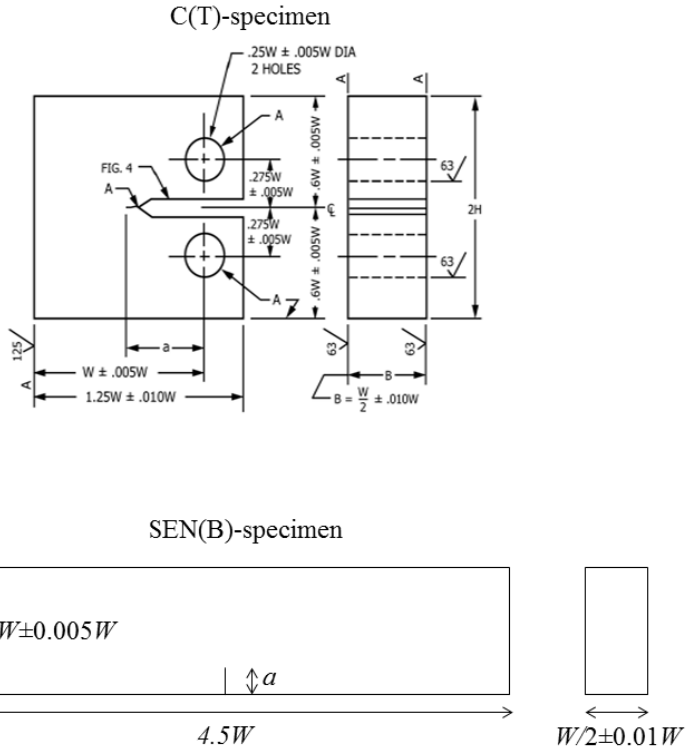

Figure 7. C(T) and SEN(B)-specimens to be used for cleavage fracture testing

Table 4. Details of the cleavage fracture tests.

Test method	Nominal location of the slice from the RPV/cladding interface	Specimen type	Maximum number of specimens per slice	Test temperature	Orientation of the specimens	Objectives	Risks
1. T_0 ASTM E1921	13 mm, ¼ thickness, ¾ thickness, possibly < 13 mm	C(T) *W* = 8 mm *B* = 4 mm *a* = 4 mm	Weld: 20 Base: 20	Multiple	T-S (circumferential welds) L-S (longitudinal welds)	T_0 through the depth of the trepans. Comparison to surveillance material.	Too many invalid specimens. Controlled by testing 20 specimens.
2. Constraint effects on fracture toughness	Close to ¼ thickness	C(T) *W* = 10 mm *B* = 5 mm *a* = 5 mm SEN(B) *W* = 10 mm *B* = 5 mm *a* = 1.5 mm	Weld: 40 Base: 40	Single	T-S (circumferential welds) L-S (longitudinal welds)	Effect of aging on constraint sensitivity. Comparison between fluence levels.	Selecting wrong temperature for testing. Should fulfil temperature requirements and measuring capacity at the same time. Will be based on results from 1.

3.2. Impact testing

Impact testing is carried out using V-notched specimens measuring 10×10×55 mm, according to standard ASTM E23. Instrumented testing is recommended to be performed according to ASTM E636. The results from impact testing are given as the energy absorbed by the specimen when struck by the hammer. Quantities of interest are typically the impact energies at specific temperatures, and the so-called upper shelf energy where the fracture is fully ductile.

As the surveillance program is mainly centred on impact testing this is a key issue in the current test matrix in order to gain insight into the transferability between the surveillance program and the B2 RPV. These specimens shall be cut-out from $^1/_4$T according to ASTM E185, that is from one-fourth of the thickness of the trepan, similar to what is done during manufacturing, measured from the inside of the pressure vessel. It is judged that around 15 specimens will be required in order to do a full characterization, Table 5. A drawing of a Charpy-V impact test specimen is presented in Figure 8.

Table 5 Details of the Charpy-V impact tests

Nominal location of the slice from the RPV/cladding interface	**Specimen type**	**Maximum number of specimens per slice**	**Test tempe-rature**	**Orientation of the specimens**	**Objectives**	**Risks**
1/4T = 130 mm/4 = 32.5 mm, this position is found in the second slice which is at a depth of 25 mm from the cladding interface	Charpy-V 10×10×55 mm	Weld: 15 Base: 15	Multiple	T-S (circumferential welds) L-S (longitudinal welds)	Absorbed energy at varying temperature for different fluence levels. T_{41J} T_{68J} Upper shelf energy	Not capturing the upper shelf behaviour properly

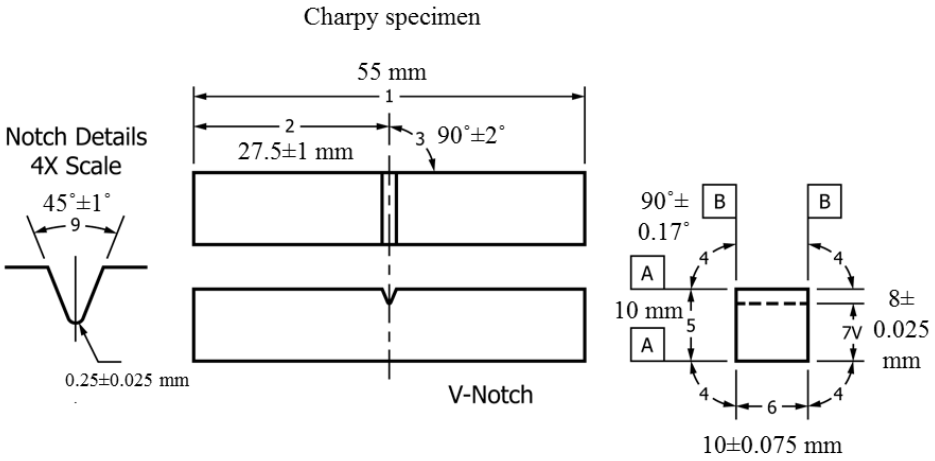

Figure 8. V-notched Charpy impact test specimen

3.3. Ductile fracture testing

Another fracture mechanism apart from the brittle or cleavage fracture mechanism, is ductile fracture. This occurs at higher temperatures, above the ductile-to-brittle transition temperature and is related to the upper shelf (energy) in the Charpy-V impact testing. In the ASME BPVC III (Rules for Construction of Nuclear Facility Components-Division 3-Containments for Transportation & Storage of Spent Nuclear Fuel & High Level Radioactive Material & Waste), the ductile fracture toughness is taken as 220 MPa√m. However, this is likely affected by irradiation embrittlement.

Testing for the ductile fracture properties is to be carried out using 10 mm thick and 20 mm wide SE(B)-specimens. Quantities of interest are the initiation fracture toughness J_{IC} and the *J-R* curve as described in ASTM E1820. It is judged that 3-5 specimens are needed per material state, i.e. base or weld metal, and fluence level. The testing should be carried out at both room temperature and reactor operating temperature. The specimens for ductile fracture testing are extracted from a separate trepan at a depth of ¼ thickness. However, the testing of the ductile fracture toughness properties are not prioritized as high as testing of the cleavage properties. The prioritization is discussed in detail in section 6.

3.4. Tensile and hardness testing

Irradiation embrittlement manifests as nano-scale changes in the microstructure of the material. These changes alters the mechanical properties of the material, specifically by hardening the material and thus increasing yield strength, and is also likely to result in a decreased work hardening. These changes are judged to be key issue of investigation in the current test matrix. In order to gain insight into these changes, tensile and hardness testing is to be carried out on the different material states.

The tensile testing is carried out using flat specimens with a cross-section of 1×2 mm and a gauge length of 8 mm, the total length of the specimens is 20 mm. Typically three tensile tests are performed and the results are averaged. Four tensile specimens are therefore suggested to be included from each slice and temperature. The preliminary tensile test matrix is presented in Table 6 and the drawing of a tensile test specimens is seen in Figure 9.

The hardness testing is to be carried out on a long side-slab that is taken from the length of the trepan, measuring 4-5x130x60 mm, Figure 10. The length of the side-slab is smaller for the RPV head trepans. A hardness profile is established through the length of the trepan, in both the base and weld metal, characterizing the effects of the decreasing radiation dose. The side-slab will be cut in pieces (probably three), to accommodate to the available grinding and polishing equipment, which is under procurement. Macrohardness measurements are performed through-wall, using HV10. Measurements along three lines is planned. Micro-hardness measurements are additionally performed at different locations through the wall using HV1 or HV0.3 to achieve information about the hardness of the local microstructure and changes thereof due to irradiation. These measurements are performed using a matrix with more than 50 points.

This side-slab is also used for other types of characterization such as chemical composition, macrostructure and microstructure. Determination of the chemical composition is still optional, as the equipment is not yet purchased. The macro- and microstructure examinations are performed using a light optical microscope, LOM, and will give information about the weld bead structure and dimensions, and on the microstructure of the different structures in the weld metal, i.e., the as-welded bead structure, the re-heated weld bead structure and possible twice reheated structures, etc.

Table 6. Preliminary tensile and hardness test matrix.

Test method	Nominal location of the slice from the RPV/cladding interface	Specimen	Number of specimens per slice and T	Test temperature	Orientation of the specimens	Objective
Tensile according to ISO 6892-1	13 mm ¼ thickness, ¾ thickness	Flat *B* = 1 mm *W* = 2 mm *L* = 20 mm L_{gauge} 8 mm	Weld: 4 x 3 Base: 4 x 3	Multiple: 1. same test temperature as for constraint, 2. 300 °C, 3: room temperature	The gauge length is in the loading direction of the fracture toughness specimens	Stress-strain curve, yield strength, ultimate tensile strength through the depth of the trepans for different temperatures and fluence levels
Hardness	A through thickness strip	Longitudinal strip	1 per trepan Minimum thickness: 4 mm	Room temperature		Hardness profile through depth of the trepans and fluence levels

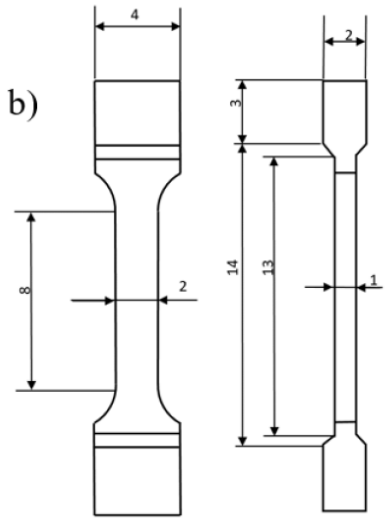

Figure 9. Drawing of a tensile specimen

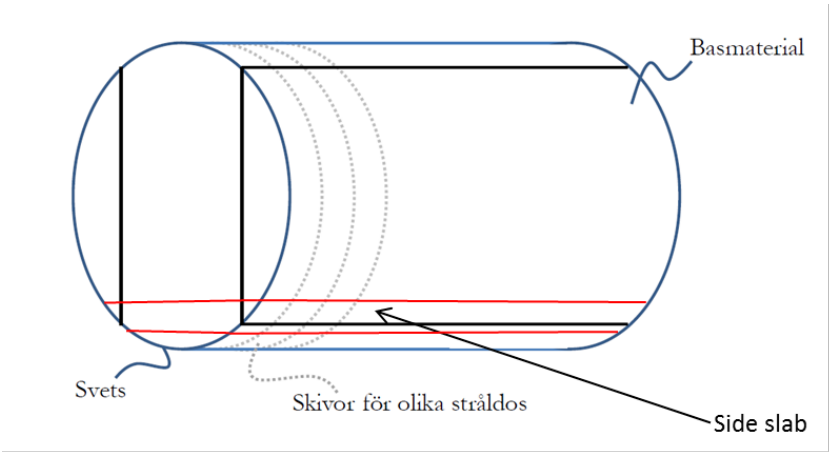

Figure 10. Locations of weld metal (svets), base material (basmaterial) and a side slab. Plates (skivor) with different fluence are cut from the trepan, and some are indicated in the drawing.

4. Other types of material characterization

The preliminary plan for both hardness as well as microstructural investigations have been presented in [2]. The main objective of the microstructural investigations is to further develop the understanding of factors affecting brittle fracture, such as local changes in the microstructure, secondary particles, straightness of the prefatigue crack front, changes in the nano-structure of the material, i.e., clustering, etc. The following investigations are planned:

- Investigations of the fracture surfaces from the mechanical tests using scanning electron microscopy (SEM) and energy dispersive analyser (EDS), especially those with brittle fracture, from which the primary initiation site will be determined. Both halves are investigated.

- LOM and SEM/EDS investigations of cross-section from the mechanical test specimens with brittle fracture at the location of initiation to determine the macro- and microstructure at the initiation site. One half is used for the cross-section, while the other half can be used for FIB investigations.

- Focussed Ion Beam, FIB, investigations of the initiation sites to determine the detailed structure of the initiator using especially transmission electron microscopy.

- Transmission electron microscope investigations to determine the precipitates in the materials and compare these with the determined initiators. Possible changes due to irradiation will also be investigated.

- Specimens will be cut for Atom Probe Tomography, APT, investigations within the BREDA project at Chalmers University. APT is used to determine the nano-scale changes from irradiation.

5. Material availability

5.1. Cutting of trepans

In order to study all of the above described mechanical properties, several slices will be needed from the trepans. At least six slices per trepan from the W14 and W16 trepans are expected. From the W28 trepans 2 slices per trepan are expected due to the shorter trepans.

A preliminary extraction of specimens from the trepans is presented in Figure 11 to Figure 14 below, in which the welds have been set to have a width of 25 mm in all estimations. This is considered to be a conservative weld width as the weld in the trepans generally is wider. All specimens have been placed with a distance corresponding to the machining by the EDM of 0.3 mm. The slices considered below are the ones that will be the most material consuming. Slices containing fewer specimens will be possible to manufacture and therefore these are not illustrated in this document. Further, the specimens should be extracted from varying positions (up and down in figures below) within the weld, this is however not illustrated in the figures below. This is to ensure that the entire weld is sampled in the testing.

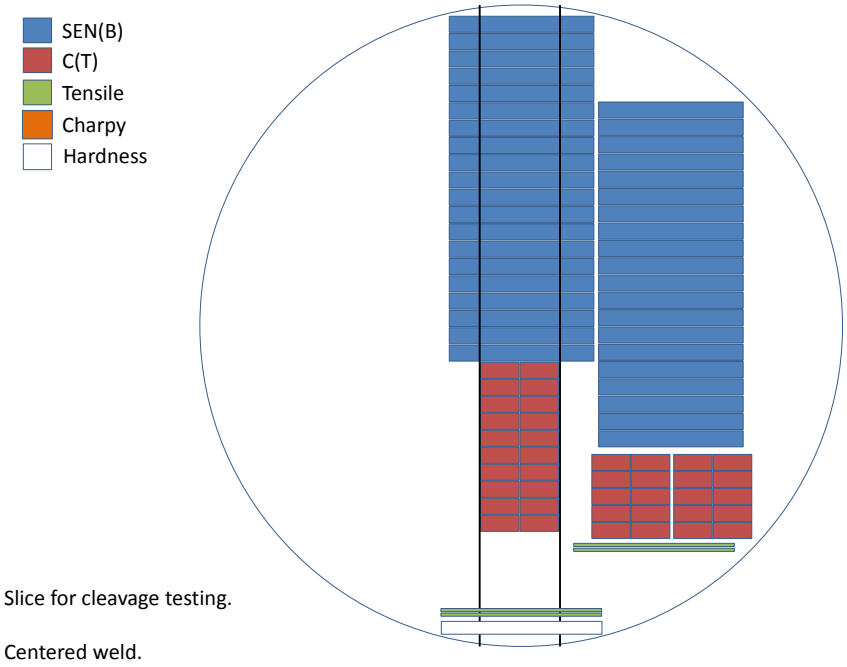

Figure 11. Estimated placement of specimens in one trepan slice for cleavage fracture testing

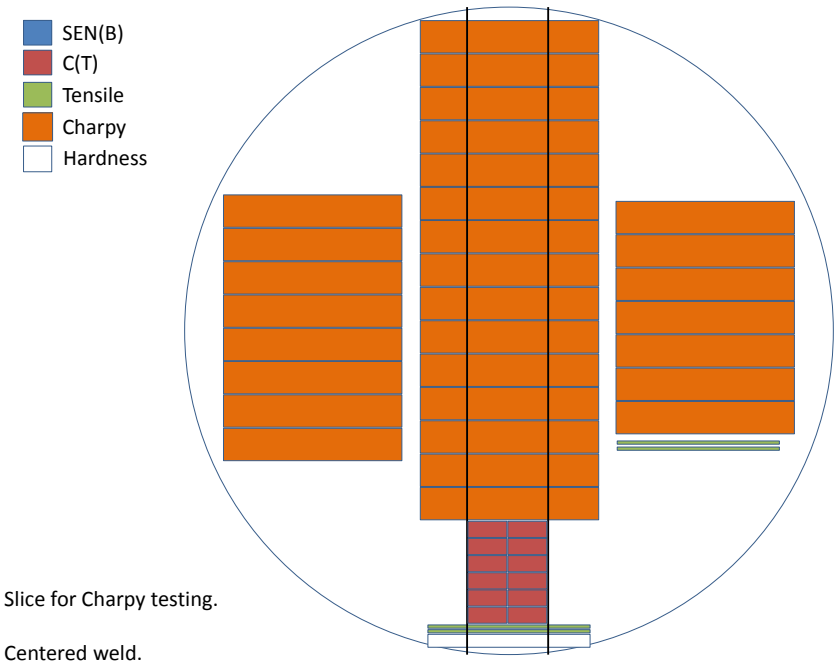

Figure 12. Estimated placement of specimens in one trepan slice for Charpy-V impact testing.

As can be seen in Figure 3, one of the W14 trepans contains an off-centre weld, this can be accounted for as seen in Figure 13 and Figure 14.

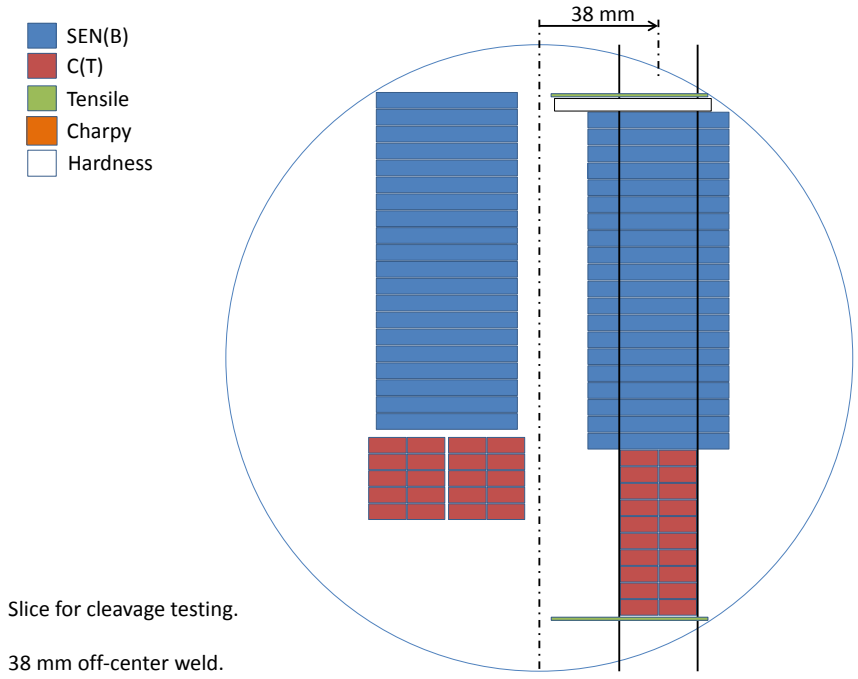

Figure 13. Estimated placement of specimens in one trepan slice containing an off-centre weld for cleavage fracture testing

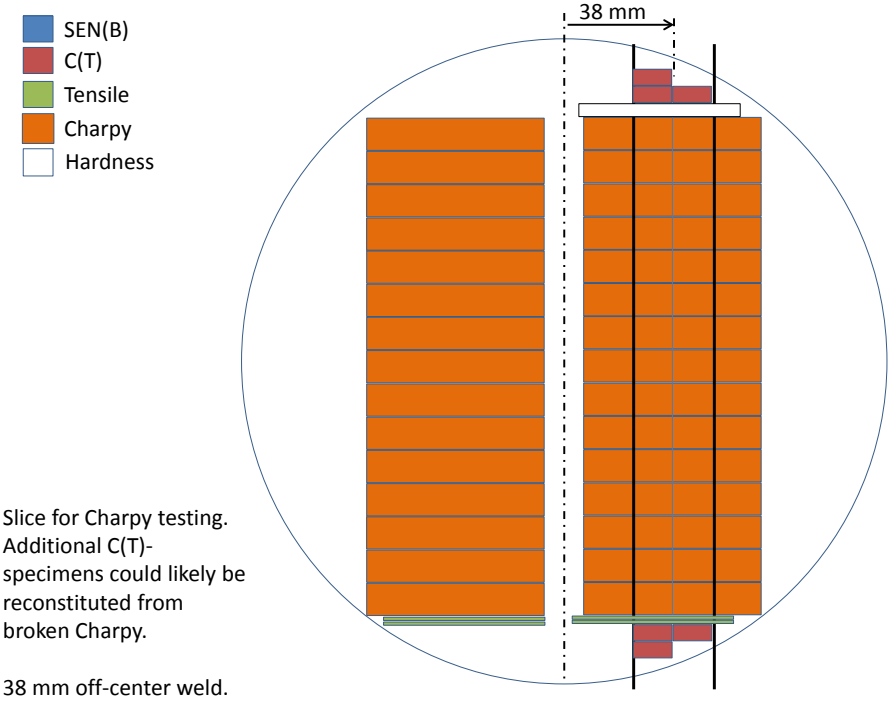

Figure 14. Estimated placement of specimens in one trepan slice containing an off-centre weld for Charpy-V impact testing.

Due to the large size of the trepans (∅200 x 135mm) in relation to the maximum height of a specimen in the electric discharge machine, EDM, with which the cutting will be done, the diameter of trepans must first be reduced, by removing some of the base material, before slices from the weld can be cut, Figure 15. After this slices from the weld and base material can be cut, as depicted in Figure 16. Schematic cutting plans of the slices for different specimens is further depicted in Figure 17 and Figure 18.

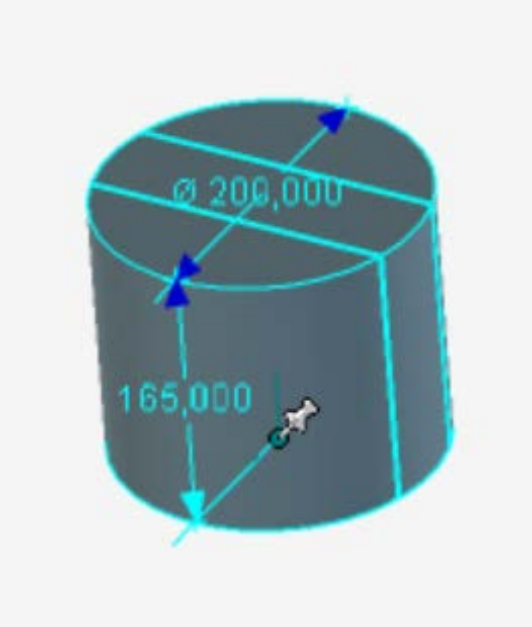

Figure 15. Initial cutting to be enable cutting of slices in the EDM at VTT

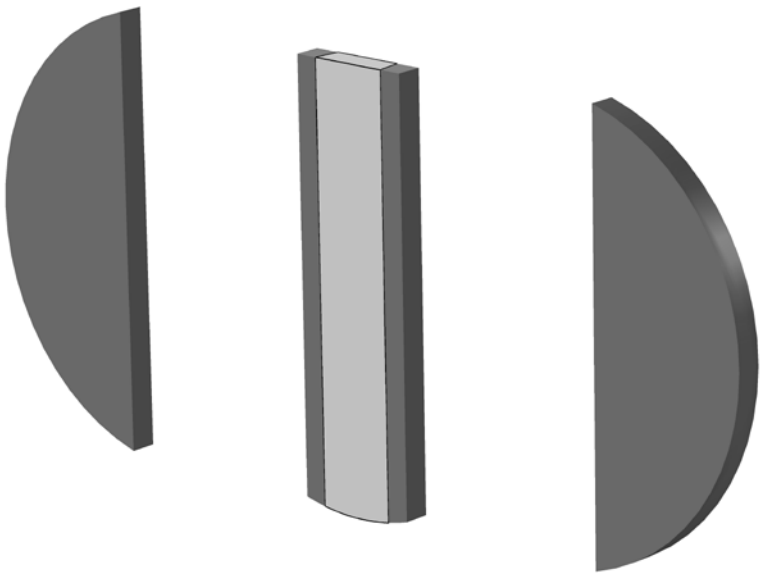

Figure 16. Slices for specimen manufacturing.

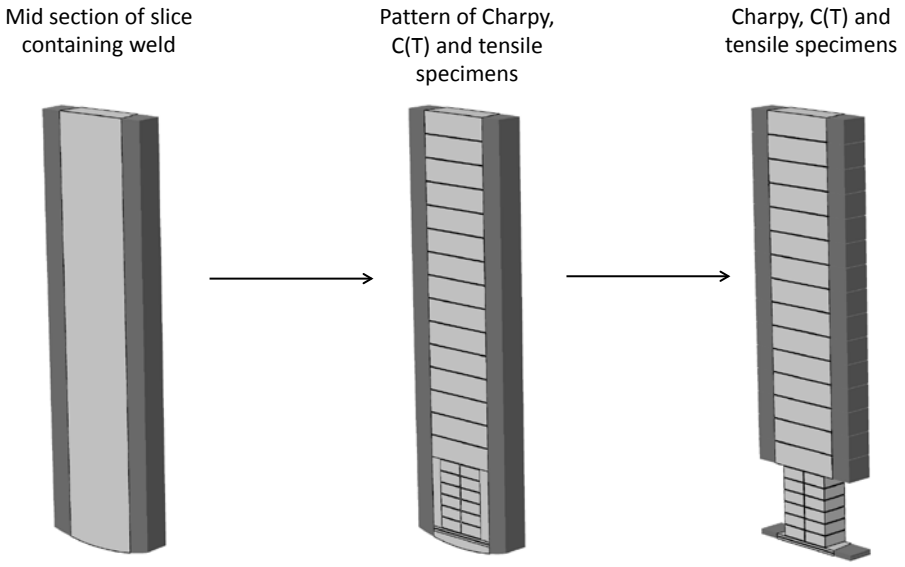

Figure 17 Division of mid slice for Charpy-V, C(T) and tensile specimen manufacturing.

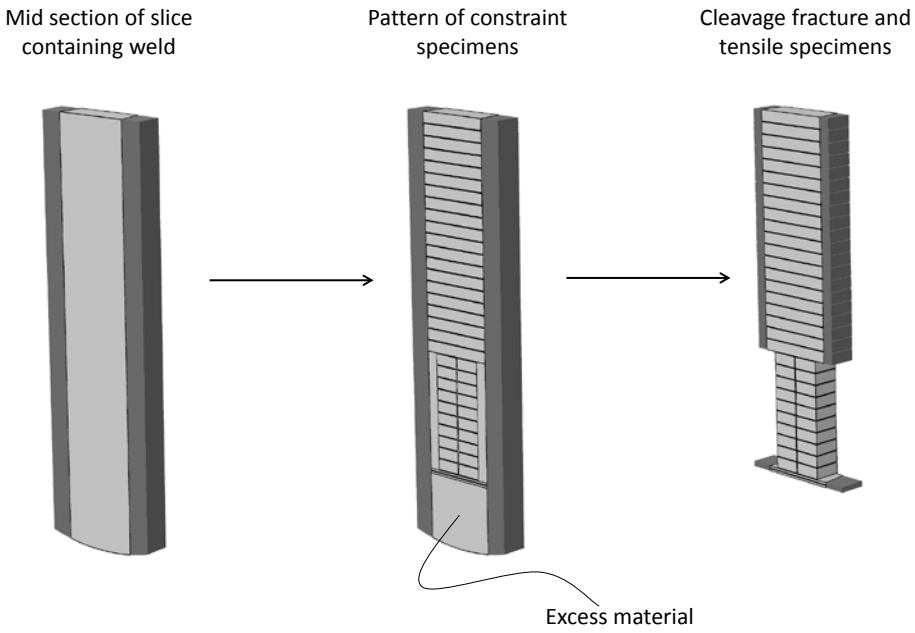

Figure 18. Division of mid slice for cleavage fracture specimen manufacturing.

5.2. Surveillance and accelerated irradiation campaign specimens

The totally six Charpy-V specimens from B2 surveillance program (3 specimens) and from the accelerated irradiation campaign (3 specimens) are used for determining the fracture toughness properties at various fluence. Main objective is to compare T_0 between the RPV and surveillance program and to establish data from high fluence material. The fracture toughness properties are determined using miniature C(T) specimens extracted from the

Charpy-V specimens. The crack of the fracture toughness specimens is in the same orientation as the notch of Charpy-V specimens, Figure 19. The Charpy-V specimens are etched before cutting of the miniature C(T) specimens so that the size of the weld can be determined and used for making a cutting plan, taking into account that the crack of the C(T) specimens shall be placed in the weld metal. As many specimens as possible are tested at each fluence. 12-16 specimens are aimed for. The miniature C(T) specimens are extracted from Charpy-V specimens tested at the lower shelf.

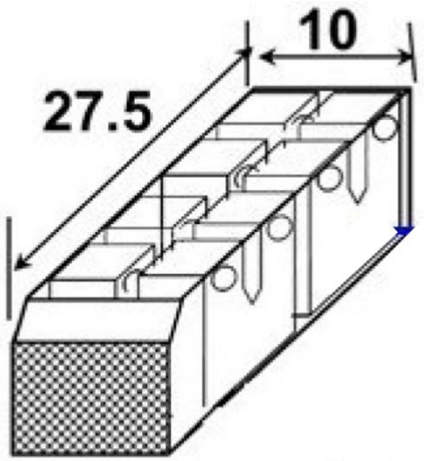

Figure 19. Principle for cutting of miniature C(T) specimens from a Charpy-V specimen. Only half of a Charpy-V specimen is depicted in the Figure.

6. Test matrix and priority

6.1. Trepan material

In this preliminary test matrix, it is assumed that four slices will be used per RPV-trepan for the testing described in Section 3. Experimental work is never 100% successful, and one must have enough redundancy in a realistic test matrix. In the case of the RPVH-trepans, a total of eight slices will be possible to manufacture from all of the four reference trepans based on the estimate in Figure 6. Hence, this also gives a redundancy for this material, given that four slices will be used for the test matrix.

For efficient use of available resources in relation to all possible tests, an overall priority list for the testing is outlined here:

1. Testing of trepan W14-2

1.1. However, applying the principle of prudence, testing will start with the non-irradiated trepan W28-1 to gain experience of cutting and testing trepans in a new environment. Pre-tests on non-BRUTE material is performed in advance, but BRUTE is still the first project to employ the new infrastructure.

2. Testing of weld metal properties
3. Testing of the Charpy-V specimens from the surveillance programme
4. Testing welds of other trepans

4.1. The trepans with higher fluence are prioritized higher than those with lower.

5. Testing of base metal properties
6. Testing of ductile fracture toughness properties.

In addition, the testing planned for each trepan is prioritized according to Table 7.

Table 7. Priority (1, 2 or 3) of tests for each trepan.

Priority	Test method	Slice	Comment
1	Cleavage fracture T_0	I, II	First and 1/4T slices
2	Cleavage fracture constraint	III, VI	First slice has higher priority, second slice can be used to find T_0 from the C(T)-specimens leaving a possibility to test low constraint specimens at a later point
2	Charpy-V impact testing	II	1/4T slice
1	Tensile	I, II, III, VI	
1	Hardness	Separate longitudinal slice	
3	Cleavage fracture T_0	< 13 mm	Dependent on hardness and microstructure characterisation results

The estimated number of specimens from four slices from one beltline RPV-trepan is as follows:

1. Cleavage fracture 1. T_0: I×20 + II×20 + VI×20 = 60 pcs.
2. Cleavage fracture 2. Constraint: III×40 + (VI×20) = 40 pcs.
3. Charpy-V: II×15 = 15 pcs.
4. Ductile fracture: I×3 = 3 pcs.
5. Tensile test: I×4 + II×4 + III×4 + VI×4 = 16 pcs.
6. Hardness: 1 pcs.

Considering this for both the weld metal and base material this results in 2×(60 + 40 + 15 + 3 + 16) + 1 = 269 specimens per beltline RPV-trepan. With four trepans from the beltline region, this sums up to a total of 1076 specimens on irradiated B2 material.

The RPVH with a slanted and non-centred weld presents a more complicated scenario for specimen manufacturing. Whole Charpy-specimen will not likely fit with a centred weld in the specimen, but hopefully the SEN(B)-specimens will fit. Regarding the issue of the Charpy-specimens, it might be possible to take these as smaller pieces from the weld that are then welded to end tabs as when reconstitution of broken specimens is done or do testing with sub-sized Charpy specimens. Estimating the number of specimen from four slices from two RPVH-trepans:

7. Cleavage fracture 1. T_0: I×20 + III×20 + IV×20 = 60 pcs.
8. Cleavage fracture 2. Constraint: II×40 = 40 pcs.
9. Charpy-V: I×15 = 15 pcs.
10. Ductile fracture: III×3 = 3 pcs.
11. Tensile test: I×4 + II×4 + III×4 + IV×4 = 16 pcs.
12. Hardness: 2 pcs.

Considering this for weld metal and base material this results in 2×(60 + 40 + 15 + 3 + 16) + 2= 270 specimens per two RPVH-trepans. With four trepans from the head region this number is doubled, i.e., 540 specimens.

The total number of mechanical test specimens for the eight trepans from the beltline and head region is thus 1076+540=1616 specimens.

7. Timeline

The BRUTE project has two corner stones, i.e., 1) pioneering the new hot cell infrastructure of the Centre for Nuclear Safety and 2) performing the testing on the B2 materials. This has the consequence that no timeline is set for the testing, yet. Work remain to be performed before testing on B2 materials can be performed in its full extent, and very little knowledge on realistic times for the different steps in the testing sequence is available. In this respect the BRUTE project is different from a traditional project producing test data and data evaluation. The BRUTE SAFIR2022 proposal for year 2019 has stated, that 2019 will be year when better understanding of the timeline for the testing shall be achieved. The proposal has also a milestone, “Agreement on updated test matrix based on existing results”, i.e., this report will be updated when the results from the first trepan are available.

References

1 Planman, T. Background and overview of mechanical testing methods to be used in BRUTE, VTT Research Report VTT-R-02227-18, 25.5.2018, 13p.

2 Lydman, J., Tapper, U., Ehrnstén, U. Characterization plan for Barsebäck 2 trepan BRUTE deliverable 2.1, 6.4.2018, 19p.

3 Boåsen, M., Efsing, P., Roudén, J., Lindgren, K., Thuvander, M., Ehrnstén, U., Lindqvist, S., Wallin, K. Underlag för materialuttag ur Barsebäck 2.

Appendix 2 - NKS-R BREDA-RPV

Constraint and fracture toughness

Deliverable for NKS project: BREDA-RPV, Barsebäck RPV trepan, NKS_R_2016_118

Sebastian Lindqvist[1]
Magnus Boåsen[2]

[1]VTT Technical Research Centre of Finland Ltd, PO Box 1000, FI-02044 VTT [2]
[2]Department of Solid Mechanics, Royal Institute of Technology (KTH), SE-100 44 Stockholm Sweden

Summary

In this report, the constraint methodology is reviewed including a description of the different constraint parameters and the effect of constraint on fracture toughness. Engineering friendly methods for assessing the effect of constraint on T0 are presented. The constraint difference between an elliptical surface crack and conventional fracture toughness specimens was estimated to cause a 25-30 °C shift in T0.

Additionally, two models for predicting the cumulative probability of failure by cleavage fracture are briefly reviewed and applied to datasets from the open literature. This shows the generally better predictions of the experiments of the non-local weakest link model at constant temperatures. But as the master curve methodology carries the capability of predictions across varying temperatures it is used in the final estimation of specimen size and temperature requirements for fracture testing of constraint effects. Potential risks related to testing such as pre-cracking problems and bimodal tendencies are also addressed in this report.

It was found that C(T) and SEN(B) specimens as high and low constraint configurations of size W = 10 mm and B = 5 mm will most likely be appropriate for testing of constraint effects on fracture toughness in the case of a limited availability of material.

Preface

This report is related to the BREDA project. The main goal in BREDA project is to estimate how well the surveillance programme describes the ageing behaviour of reactor pressure vessel. In BREDA, samples are harvested from Barsebäck (Sweden) reactor pressure vessel. The fracture mechanical properties of the RPV samples will be compared to the existing results from surveillance programme of Barsebäck. The experimental investigations focus on the weld metal, as the weld metals are the limiting materials from a Long Term Operation, LTO, perspective.

This report focuses on the effect of constraint on fracture toughness. There is an interest in BREDA project and also in the SAFIR programme to investigate the effect of constraint on fracture toughness. This work focuses on describing the background for the constraint effect in fracture mechanics. It is important to understand how the constraint can be described and what is the effect on key mechanical parameters important for assessing the safety of nuclear power plants e.g. ductile-to-brittle transition temperature. This work focuses also on determining a suitable specimen size to investigate the constraint effect for the Barsebäck material.

The report is intended for persons with some previous background in fracture mechanics. The introduction section gives a basic overview of constraint and fracture toughness models. After that, the constraint parameters and the effect of constraint on fracture toughness are described in detail. Finally, the modelling of constraint and selection of a suitable specimen for characterization of the effect of constraint on fracture toughness is discussed. The report contains a lot of information, therefore, the report is recommended to be read one section at time with breaks in between.

Table of Contents

1 Introduction

Fracture toughness can be described as material's ability to resist crack propagation. The quantity defining fracture toughness can take on several different forms, most commonly by the stress intensity factor K_I, the energy release rate G, or the J-integral. All of these quantities can be related to the loading and deformation of the volume directly ahead of the crack tip. In steels and other metallic alloys crack propagation generally occurs in two distinctly different mechanisms, either through ductile fracture, or through brittle/cleavage fracture. This report will mainly deal with the latter mechanism related to ferritic steels and how this mechanism is affected by crack tip constraint.

1.1 Why is it important to take into account the effect of constraint on fracture toughness?

Ideally, K_I and J-integral should uniquely describe the critical stress and strain fields ahead of a sharp crack at fracture. However, in reality the constraint, i.e. stress triaxiality, affects the obtained fracture toughness. Constraint is affected by the specimen configuration, crack depth, absolute ligament size, section thickness, specimen size and loading. Therefore, the obtained fracture toughness is geometry and configuration dependent.

In fracture toughness testing standards, the fracture toughness is usually determined with specimens that maximize crack-tip constraint, by using deeply cracked, relatively thick, bend loaded specimens. A high constraint results in a conservative estimate of the fracture toughness of a material. In real structures, the cracks are typically small relative to other dimensions, the cracks are three dimensional and the loading is predominately tensile. These factors alone or in combination, decrease the crack tip constraint, and thus increase the fracture toughness compared to the one obtained with conventional fracture toughness specimens. With conventional fracture toughness specimens, some variation will exist in the obtained fracture toughness depending on the used specimen geometry, loading condition, specimen type, size, and crack length. These variations are small compared to the difference between the fracture toughness obtained with conventional specimens and the fracture toughness of structures.

Currently, in safety analyses, the conservatism resulting from using conventional test specimens is accepted and the obtained fracture toughness is used as such for structural integrity analysis. Alternatively, the constraint difference between the structure and the fracture toughness specimen can be assessed, and the fracture toughness can be adjusted accordingly. Different constraint theories have been developed to assess the constraint difference. These theories should be used for assessing the effect of constraint on the J-R curves, and on the master curve and the associated reference temperature T_0.

1.2 Models for cleavage fracture in ferritic steels

1.2.1 Master curve methodology

One of the most widely used weakest link models for describing cleavage fracture in ferritic steels is the model commonly referred to as the master curve. The model has its name from being able to capture the temperature effects as well as the statistical size effect associated with cleavage fracture. The probabilistic model relies on the self-similar stress fields ahead of a sharp crack governed by the elastic stress intensity factor K_I. This results in a 3-parameter Weibull distribution with a constant shape parameter for the cumulative failure probability of

cleavage fracture which emerges as a result from the self-similar crack tip fields. The cumulative probability of failure is expressed as

$$P_{\mathrm{f}} = 1 - \exp\left[-\frac{B}{B_0}\left(\frac{K_{\mathrm{I}} - K_{\min}}{K_0 - K_{\min}} \right)^4 \right], \tag{1}$$

where B is the specimen thickness, B_0 is a reference thickness taken as 25.4 mm, $K_{\min}$ is a minimum fracture toughness taken as 20 MPa$\sqrt{\mathrm{m}}$, and K_0 is a temperature dependent reference fracture toughness at a probability of failure of 63.2 % defined for a specimen of size B_0. The reference fracture toughness K_0 is given by

$$K_0 = 31 + 77\exp\left[0.019\left(T - T_0 \right) \right] \text{ MPa}\sqrt{\mathrm{m}}, \tag{2}$$

where T is the temperature and T_0 is the reference temperature for ferritic steels in the transition region. From (1) follows a relation for size predictions which can be written on the form

$$K_{Jc_x} = K_{\min} + \left[K_{Jc_0} - K_{\min} \right]\left(\frac{B_0}{B_x} \right)^{1/4}, \tag{3}$$

where fracture toughness with subscript corresponds to the specimen size of the same subscript.

The reference temperature T_0 is found from fracture test carried out at a single or at multiple temperatures. Specimens with thickness other than 25.4 mm are first rescaled to 25.4 mm using (3) and then used to estimate T_0. Details regarding censoring of data, specimen capacity and temperature requirements can be found in ASTM E1921 (ASTM International, 2016).

In the master curve methodology, the elastic T-stress quantifies the effect of crack tip constraint through a connection to the reference temperature T_0 and the assumption that the shape of the master curve remains unchanged by loss of constraint. The effect of a positive T-stress was found to be insignificant with respect to the cleavage fracture toughness since the positive T-stresses are not that large, whereas negative T-stress appears to affect the master curve in a nearly linear relation with respect to T_0. The T-stress at the plastic limit load is to be used as explored by Wallin (Wallin, 2001) and (Wallin, 2007). The T-stress adjusted K_0 takes on the form

$$K_0 = 31 + 77\exp\left[0.019\left(T - T_0 - A\frac{\Delta T_{\mathrm{stress}}}{\sigma_{\mathrm{Y}}} \right) \right] \text{ MPa}\sqrt{\mathrm{m}}, \tag{4}$$

where the difference of the T-stress between the specimen configuration used to determine T_0 and the analyzed structure should be used, the factor A has been found by Wallin to be yield stress dependent and can be written on the forms

$$A = \begin{cases} 40\ ^{\circ}\mathrm{C} \text{ for } \sigma_{\mathrm{Y}} < 600\,\mathrm{MPa} \\ \dfrac{\sigma_{\mathrm{Y}}}{12\,\mathrm{MPa}/^{\circ}\mathrm{C}} \text{ for } T_{\mathrm{stress}} < 300\,\mathrm{MPa} \end{cases}. \tag{5}$$

In a realistic structure, a defect will vary significantly from that of a laboratory specimen. Most likely the size and the shape of the defect will differ from that of a straight crack front. This might give rise to a temperature variation, as well as a varying constraint along the crack front. In order to handle this, the crack front quantities needs to be integrated according to

$$P_f = 1 - \exp\left[-\int_0^s \left(\frac{K_{J\Phi} - K_{min}}{K_{0\Phi} - K_{min}} \right)^4 \frac{ds}{B_0} \right], \tag{6}$$

where s is the crack front coordinate and subscript Φ indicates local crack front quantities which are integrated to give the failure probability.

A more advanced form of the master curve is the bimodal master curve. The incorporation of two competing toughness distributions within the same material volume forms the basis of the bimodal master curve. This results in the failure probability as

$$P_f = 1 - p_a \exp\left[-\frac{B}{B_0} \left(\frac{K_I - K_{min}}{K_{0_1} - K_{min}} \right)^4 \right] - (1 - p_a) \exp\left[-\frac{B}{B_0} \left(\frac{K_I - K_{min}}{K_{0_2} - K_{min}} \right)^4 \right]. \tag{7}$$

Which has three parameters, the two reference toughnesses K_{01} and K_{02} (or T_{01} and T_{02}) and the occurrence probability p_a. The bimodal master curve imposes complications to the fitting procedure which are detailed in (Wallin, et al., 2004) and (Wallin, 2011).

1.2.2 Non-Local weakest link model for cleavage fracture

Models that evaluate the probability of failure from the local crack tip fields, i.e. stress and strain directly are commonly referred to as local models. Several models exist, but in this report only one model will be considered. The model developed by Kroon and Faleskog (Kroon & Faleskog, 2002) has been shown to be able to predict the probability of failure by cleavage fracture both qualitatively and quantitatively, which is why it has been chosen to represent the so called local models in this report. The model has been successfully applied to both cleavage fracture tests with no prior ductile tearing Faleskog et al. (Faleskog, et al., 2004) and tests with ductile tearing prior to final failure by cleavage fracture Kroon et al. (Kroon , et al., 2008). The model has also been scrutinized by Hohe et al. (Hohe, et al., 2008) and (Hohe, et al., 2010) where this model was found to be very capable of predicting constraint effects on cleavage fracture.

The model was developed on the basis that microcracks nucleate as a consequence of slip induced cracking of a second phase brittle particle, such as a grain boundary carbide. Moreover, it is assumed that sustained growth of a microcrack that eventually triggers a macroscopic failure by cleavage fracture requires a high stress level over a sufficiently large distance. This due to that a nucleated microcrack needs to propagate unhindered across several microstructural barriers, such as high angle grain boundaries before it can become a cleavage crack. This has been handled by the introduction of a non-local scalar stress measure which is formed over the volume defined by the radius L.

In the model by Kroon and Faleskog, the cumulative probability of failure by cleavage fracture is defined as

$$P_{\mathrm{f}} = 1 - \exp\left(-\int_{V} h_{\max} \frac{\mathrm{d}V}{V_0} \right), \tag{8}$$

where $h_{\max}$ is the maximum value of the random function experienced throughout the loading history, V is the volume of the structure, and $V_0$is the reference volume. The random function $h(\varepsilon_{\mathrm{e}}^{\mathrm{p}}, \bar{\sigma})$ is taken as

$$h\left(\varepsilon_{\mathrm{e}}^{\mathrm{p}}, \bar{\sigma}\right) = h_1\left(\varepsilon_{\mathrm{e}}^{\mathrm{p}}\right) h_2\left(\bar{\sigma}\right), \tag{9}$$

where

$$h_1\left(\varepsilon_{\mathrm{e}}^{\mathrm{p}}\right) = c\varepsilon_{\mathrm{e}}^{\mathrm{p}}, \tag{10}$$

$$h_1\left(\bar{\sigma}\right) = \exp\left(-\left(\frac{\eta\sigma_{\mathrm{th}}}{\bar{\sigma}} \right)^2 \right) - \exp\left(-\eta^2\right) \quad \text{for} \quad \bar{\sigma} > \sigma_{\mathrm{th}}. \tag{11}$$

In (10) and (11), $\varepsilon_{\mathrm{e}}^{\mathrm{p}}$ is the effective plastic strain, $\bar{\sigma}$ is a non-local scalar measure of stress, c, σ_{th} and η are material parameters. The parameter c is related to the nucleation of microcracks due to plastic straining, and the threshold stress σ_{th} is related to the largest microcrack available to partake in a cleavage process. The parameter η is related to the shape of the microcrack distribution and has been shown to have little influence in practical applications (Kroon & Faleskog, 2002).

The non-local scalar measure of stress is calculated from the non-local stress tensor defined by

$$\bar{\sigma}_{ij} = \frac{1}{V_{\mathrm{L}}} \int_{V_{\mathrm{L}}} \sigma_{ij}\left(\hat{\mathrm{X}} - \mathrm{X}\right) \mathrm{d}\hat{\mathrm{V}}, \tag{12}$$

where $\mathbf{X}$=(X_1, X_2, X_3) are the coordinates of the center of V_{L}. In this report, the non-local scalar measure of stress is taken as the non-local maximum principal stress $\bar{\sigma}_1$, calculated from $\bar{\sigma}_{ij}$.

Estimation of model parameters requires fracture tests at two different levels of crack tip constraint in order to yield accurate estimation. Parameter estimation based only on one set of fracture tests will yield ambiguous estimates of the model parameters (Faleskog, et al., 2004).

2 Constraint

2.1 Constraint parameters

Different constraint parameters and constraint assessment procedures have been developed; a J small scale yielding correction (SSYC), T-stress, Q-parameter, A2 three term solution, triaxiality parameter h, or applying the local approach model directly to the stress and strain fields ahead of the crack front to assess the effect of constraint. The local approach and SSYC currently have less applicability for engineering assessment of constraint effects on fracture due to the need of highly detailed elastic-plastic finite element analysis of the crack tip fields.

The crack-tip stress field in an isotropic elastic material can be expressed as an infinite power series, where the leading term exhibits a $1/\sqrt{r}$ singularity, the second term is constant with r, the third term is proportional to $\sqrt{r}$, and so on. Classical fracture mechanics theory normally neglects all but the singular term. In practice, only the first and second terms have an effect on the stress at the crack-tip. The second term can have a profound effect on the plastic zone shape and the stresses deep inside the plastic zone. The second term is defined by the *T*-stress.

The *T*-stress can be obtained from a straight forward elastic analysis. The *T*-stress is a non-singular stress component acting parallel to the crack surfaces, but gives also an approximation of the opening stress

$$\sigma_{ij} = \frac{K_I}{\sqrt{2\pi r}} f_{ij}\left(\theta\right) + T\delta_{1i}\delta_{1j}, \tag{13}$$

where K_I is the stress intensity factor based on linear elastic analyses, f_{ij} is a dimensionless function depending on specimen geometry and boundary conditions, and σ_{ij} is the stress tensor located at a point (r, θ) ahead of the crack front. In classical fracture mechanics theory, only the first term in Equation (13) is considered, and is a single-parameter description of the near-tip fields and describes the overall loading of the crack tip.

The *T*-stress is commonly expressed in terms of the biaxiality ratio β, which connects the stress intensity factor, K, with the *T*-Stress as

$$\beta = \frac{T\sqrt{\pi a}}{K_I} \tag{14}$$

The stress intensity can be written on the form

$$K_I = \sigma\sqrt{\pi a} f\left(\frac{a}{W}\right), \tag{15}$$

where σ is a remote stress, a is the crack length and f is a geometry and boundary condition dependent dimensionless function similar to Equation (13). By combining Equation (14) and (15), and assuming that the specimen fails close to the plastic limit load, an approximate *T*-stress solution related directly to material's yield strength can be determined.

$$\frac{T}{\sigma_{ys}} = \beta f\left(\frac{a}{W}\right) \tag{16}$$

This is an engineering friendly way to determine *T*-stress, since it can be connected to K_{Jc}.

In contrast to the *T*-stress, the *Q*-parameter is defined as the difference in stress between the HRR field and the actual stress at a specific location ahead of the crack normalized by the yield stress as

$$\sigma_{ij} = \left(\sigma_{ij}\right)_{HRR} + Q\sigma_{ys}\delta_{ij} \text{ for } r > J/\sigma_0 \text{ and } \left|\theta\right| \le \pi/2 \tag{17}$$

where $(\sigma_{ij})_{HRR}$ is the HRR stress field, and σ_{ys} is the yield stress. Q varies with distance to the crack-tip and with load. The Q-parameter is quite strongly dependent on load and geometry up to the limit load. Typically, the constraint deceases as the load increases. By determining the actual stress tensor σ_{ij} ahead of the crack with finite element analyses, Q is typically defined as

$$Q = \frac{(\sigma_{\theta\theta})_{FEA} - (\sigma_{\theta\theta})_{HRR}}{\sigma_0}, \text{ at } r = \frac{2J}{\sigma_0} \text{ and } \theta = 0 \tag{18}$$

where $\sigma_{\theta\theta}$ is the opening stress defined by a crack tip coordinate system. A third constraint parameter is the triaxiality parameter *h* defined as the ratio between hydrostatic stress and the von Mises equivalent stress, and is evaluated at a fixed position of the ligament, similarly to *Q*.

An extension to the basic definitions of *T*-stress and *Q*-parameters have been developed for situations of large scale yielding. During LSY of bending dominated specimens, the bending moment can impinge the crack-tip stress field and the constraint parameters can lose their validity. To eliminate the influence of bending, a bending modified constraint solution was introduced by adding a term to reflect the global bending stress and leading under fully plastic conditions to a value independent of applied loading (Zhu and Joyce 2012). However, the use of the bending modified Q is cumbersome and leads to 20 % more negative *Q* values. (Wallin 2011)

2.2 Connection between the different constraint parameters

Up to the limit load, the *T*-stress/σ_{ys} and the *Q*-parameter give approximately the same value for constraint. After the limit load, the *T*-stress/σ_{ys} becomes conservative relative to *Q*-parameter. Up to general yielding, both parameters can be used, but the *Q* tends to be mesh sensitive for small loadings and *T*-stress is more reliable. Beyond general yield *Q* is more reliable. For *Q* values < 0, the limit load *T*-stress /σ_{ys} and *Q* follow a linear relationship and are approximately equal. The error between the normalized *T*-stress and Q is small (~0.2). For positive constraint values, the error grows and the *Q* does not differ significantly from 0. A relation (~10 % accuracy) between the constraint parameters *h* and *Q* is

$$Q \approx h - 2 - \frac{E/\sigma_{ys}}{2295} - \frac{3.35}{N}. \tag{19}$$

2.3 Constraint parameters for brittle fracture and ductile fracture

The stress state ahead of the crack front controls cleavage fracture. Therefore, the *T*-stress/σ_{ys} and *Q* are considered viable parameters to describe constraint in brittle fracture conditions, as these are defined from the stress state. For ductile fracture, a more suitable measure to quantify the level of constraint are the Q_m and h parameters, since ductile fracture is typically controlled by void growth, and thus, is dependent on hydrostatic stress. The Q_m is the

hydrostatic stress definition of Q and is determined at initiation of ductile fracture or at another parameter. Q_m can differs from Q with ~10 %. Thus, the Q and T-stress/σ_{ys} give a rough approximation of the constraint also in the ductile regime. The Q and T-stress/σ_{ys} are both considered suitable for use in structural engineering assessments, since the parameters can be used to some extent both for analysis of brittle and ductile fracture.

For ductile materials, the plastic strains grow with decreasing constraint. Thus, the constraint effect is usually smaller for ductile fracture than for cleavage fracture controlled by the opening stress, **Figure 1**. [2]

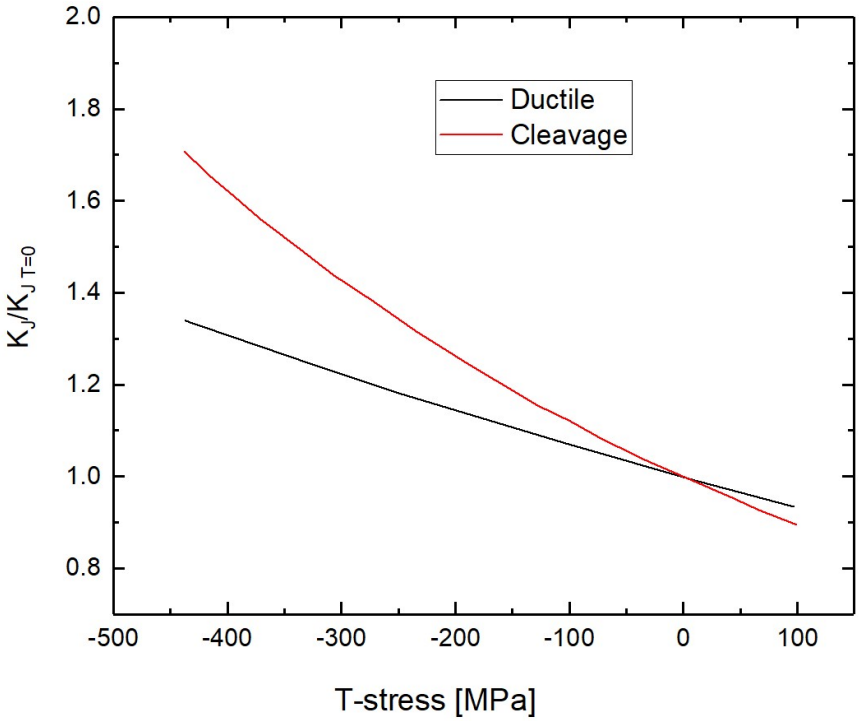

Figure 1. The effect of constraint on the fracture toughness. $K_{J\ T=0}$ referes to fracture toughness obtained with a high constrint specimen.

2.4 Effect of constraint on fracture toughness

The fracture toughness obtained from experiments is affected by the constraint of the chosen specimen. The difference in geometrical constraint for deeply cracked C(T) and SE(B) specimens has been observed to yield different fracture toughness and thereby also different T_0 for the same material (Wallin et al. 2001). The constraint is affected by the relative crack length (a/W), absolute ligament length, specimen configuration and load. Specimen thickness has also an effect on constraint, but only after the measuring capacity has been lost. The absolute ligament length (b) controls the measuring capacity of the specimen (Wallin 2011). Constraint loss affects both ductile, brittle fracture and crack arrest. In addition, in the ductile-to-brittle transition temperature regime, the fracture toughness is affected by the statistical weakest link size effect. The statistical weakest link size effect related to the specimen thickness, leads to an increase in fracture toughness with decreasing thickness and affects mainly the brittle fracture toughness properties. The statistical weakest link mechanism differs from the constraint effects and is therefore not described in this report in detail.

Effect of specimen and relative crack length:

Figure 2 shows the effect on specimen configuration on constraint. The constraint of SE(T) specimens is close to that of cracks in pipes. The deeply cracked SE(B) and C(T) have a high-constraint leading to a low fracture toughness. **Figure 3** shows the effect of relative crack length on constraint for SE(B), SE(T) and C(T) specimens. Generally, the shorter the crack, the smaller is the constraint, and consequently, the larger is the fracture toughness.

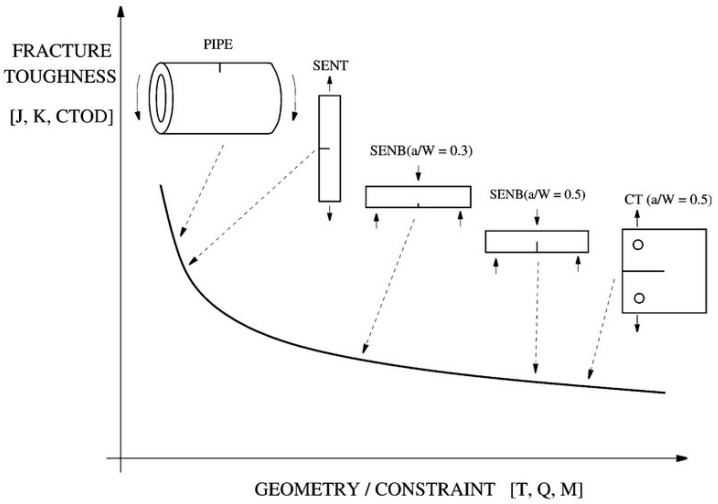

Figure 2. Deeply crack SE(B) and C(T) specimens provide a conservative estimate of fracture toughness. SENT = SE(T), SENB = SE(B), CT = C(T).

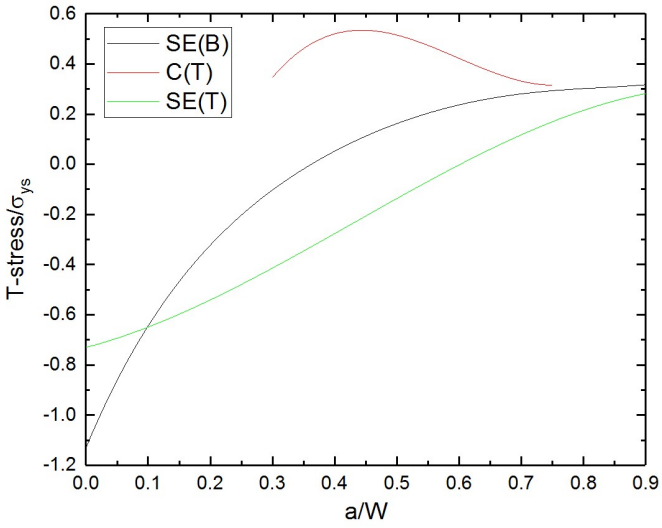

Figure 3. How constraint changes with relative crack length a/W for different specimens. Positive T-stresses are not directly comparable to the Q.

SE(B) specimens of different *a/W* ratios are normally used for characterizing the effect of constraint, since SE(B) specimens are routinely used. Crack lengths larger than $a/W > 0.45$ have only a marginal effect on the fracture toughness, but lower crack lengths lead to an increase in fracture toughness (ASTM E1820-15 2015). The problem with the use of the SE(B) specimen is that the constraint changes rapidly with *a/W*. Small variations in *a/W* can lead to large variations in constraint. C(T) specimens are not suitable for shallow flaw ($a/W < 0.4$) testing for three reasons. Firstly, the loads on the pins grow too large. Secondly, the specimen contains a moment of force that can cause the crack to deviate from the fatigue pre-crack plane, and can lead even to perpendicular crack growth relative to the fatigue pre-crack

plane. Thirdly, if constraint effects on the fracture toughness are of interest, the T-stress is positive over the entire interval of *a/W* indicating that loss of crack tip constraint does not occur for shallow flaws in a C(T) specimen.

Effect of absolute ligament length:

The absolute ligament length affects the measuring capacity of the specimen. After the specimen has lost its measuring capacity, the thickness of the specimen starts to affect the constraint. The effect of absolute ligament length on ductile and brittle fracture toughness properties differ. After the measuring capacity is reached, the fracture toughness increases in the brittle regime. The violation of the measuring capacity in ductile regime leads to a lower *J-R* curve and the measuring capacity appears to be proportional to the relative crack growth of the ligament (d*a*/*b*). (Wallin 2011)

In ASTM E1820, the maximum J-integral capacity for a specimen in the ductile regime is given by the smaller of the following

$$J_{max} = b_0 \sigma_{YS} / 10, \tag{20}$$

$$J_{max} = B \sigma_{YS} / 10, \tag{21}$$

where b_0 is the initial ligament and B is the thickness of the specimen.

The maximum crack extension capacity for a specimen is given by the following

$$\Delta a_{max} = 0.25 b_0. \tag{22}$$

The restrictions were determined from a large data base with fracture toughness specimens of different sizes. The $\Delta a_{\max}$ and $J_{\max}$ values correspond the point where the *J-R* curve for the smaller specimen deviates with 15 % from the median *J-R* curve for a large specimen. For specimens where the data did not deviate from each other, the end of test values were used to provide a conservative $J_{\max}$ and $\Delta a_{\max}$.

In ASTM E1921, the maximum K_{Jc} capacity of a specimen in the ductile-to-brittle transition region is given by

$$K_{Jc(\text{limit})} = \sqrt{\frac{E b_0 \sigma_{\text{YS}}}{30\left(1-\nu^2\right)}}, \tag{23}$$

where E is the Young's modulus and ν the Poisson ratio. The measuring capacity in the ductile-to-brittle region is defined as the largest macroscopic fracture toughness that is still descriptive of the effective crack driving force. At small *J*-integral values, a straight line describes the difference between the two specimen sizes, in accordance with the Master Curve size effect. FE analyses, focusing only on the behavior of the stress field, generally predict a lower measuring capacity for bend specimens than observed experimentally. The effective crack driving force is dependent on stress and strain distribution ahead of the crack and the fracture mechanism.

Effect of thickness on ductile materials:

For bend specimens, specimen thickness starts to affect constraint only after the specimen has lost the measuring capacity. Small difference in slimness and thickness produce only small differences in *J-R* curves. However, very slim and large enough specimens fail by shear, which lowers the *J-R* curves. For slim specimens the plane stress condition dominates, and a size-independent *J–R* curve can be obtained. The thickness can play also an effect on the *J-R* curves, if the specimens are not side-grooved. For plane side specimens, the crack can tunnel at the center resulting in an increase in the *J-R* curves. (Wallin 2011)

Effect of load:

Figure 4 shows the effect of load (expressed as *J*) on the constraint parameter *Q*. For short cracks, the constraint changes rapidly with the increasing load. Also for the longer cracks the constraint decreases with the increasing load, but not as fast. Polynomial equations were fitted to the *J-Q* curves, equations (24) to (28), so that the effect of load on constraint can be analyzed in section 2.6. The equations can be used for assessing the effect of load on the shape of the Master Curve or assessing the *Q* at a specific load.

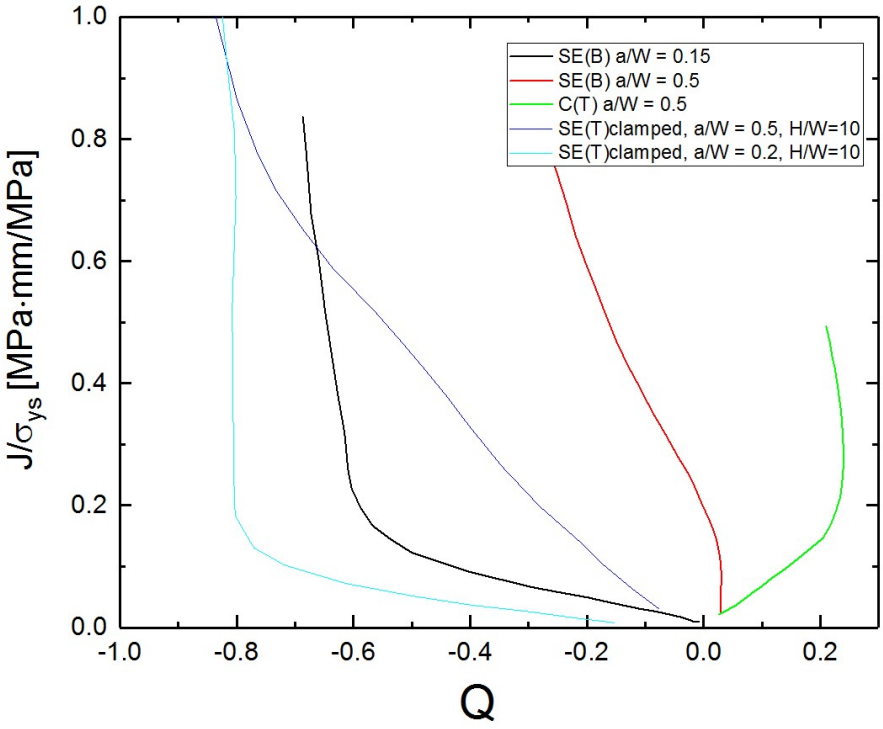

Figure 4. The effect of load on the constraint for different specimen geometries with b = 25.4 mm. and for materials with yield strength between 350 and 480 MPa *(Moattari and Sattari-Far 2017; Ruggieri 2017)*.

C(T) with $a/W = 0.5$

$$Q = 5\left(\frac{J}{\sigma_{YS}}\right)^3 - 6\left(\frac{J}{\sigma_{YS}}\right)^2 + 2.2\left(\frac{J}{\sigma_{YS}}\right) - 0.03 \qquad (24)$$

between $J/\sigma_{YS} = 0$ and 0.5 ($R^2 = 0.99$)

SE(B) with $a/W = 0.5$

$$Q = 1.1\left(\frac{J}{\sigma_{YS}}\right)^3 - 1.48\left(\frac{J}{\sigma_{YS}}\right)^2 + 0.1\left(\frac{J}{\sigma_{YS}}\right) + 0.02 \quad (25)$$

between J/σ_{YS}= 0 and 0.9 (R^2 = 0.99)

SE(B) with a/W = 0.15

$$Q = 16.4\left(\frac{J}{\sigma_{YS}}\right)^4 - 33\left(\frac{J}{\sigma_{YS}}\right)^3 + 23.3\left(\frac{J}{\sigma_{YS}}\right)^2 - 6.8\left(\frac{J}{\sigma_{YS}}\right) + 0.06 \quad (26)$$

between J/σ_{YS}= 0 and 0.8 (R^2 = 0.99)

SE(T) with a/W = 0.5, H/W = 10, Clamped

$$Q = 0.5\left(\frac{J}{\sigma_{YS}}\right)^2 - 1.3\left(\frac{J}{\sigma_{YS}}\right) - 0.03 \quad (27)$$

between J/σ_{YS} = 0 and 1 (R^2 = 0.99)

SE(T) with a/W = 0.2, H/W = 10, Clamped

$$Q = 27.7\left(\frac{J}{\sigma_{YS}}\right)^6 - 109.7\left(\frac{J}{\sigma_{YS}}\right)^5 + 174.3\left(\frac{J}{\sigma_{YS}}\right)^4 - 37.4\left(\frac{J}{\sigma_{YS}}\right)^3 + 55.4\left(\frac{J}{\sigma_{YS}}\right)^2 - 10.6\left(\frac{J}{\sigma_{YS}}\right) \quad (28)$$

between J/σ_{YS}= 0 and 0.7 (R^2 = 0.99).

Figure 5 shows results from testing of a weld metal. Testing was done with 4 mm thick miniature C(T) specimens size corrected to 25.4 mm. The load of the size corrected values varied between 0.01-0.04 MPa·mm/MPa. These values are located in the lower region in **Figure 4**. The comparison is made so that the load range practical for fracture toughness testing can be estimated. The median fracture toughness at T_0 is 100 MPa$\sqrt{m}$ corresponding to 0.06 MPa·mm/MPa. Median fracture toughness at T_0 + 50 °C is 211 MPa$\sqrt{m}$and corresponds to 0.31 MPa·mm/MPa.

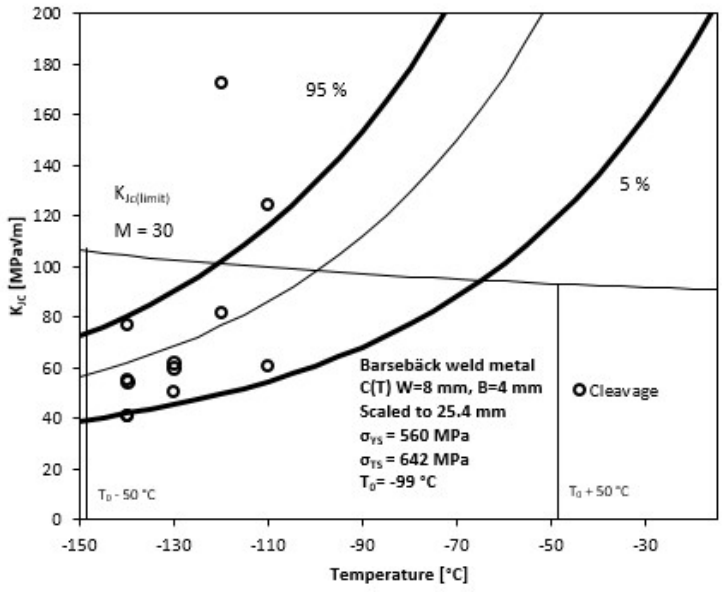

Figure 5. Master Curve analysis of the Barsebäck weld metal.

Figure 6 a shows the variation in constraint between a SE(B) and C(T) specimens with a/W = 0.5. The difference in Q is approximately 0.2 at J/σ_{YS} = 0.3. The difference in constraint between a SE(B) specimen with a/W = 0.5 and SE(T) specimen with a/W = 0.5 is of the same order. The SE(B) specimens with a/W = 0.15 and SE(T) specimen with a/W = 0.2 have a significant effect on constraint. **Figure 6** b shows the variations in T-stress for various configurations. The difference in T-stress/σ_{ys} for SE(B) and C(T) specimens with a/W = 0.5 is ~0.35. **Figure 7** shows the rate of change in Q as a function of J/σ_{YS}. The change in Q is large for SE(B) specimens with a/W = 0.15 and SE(T) specimens with a/W = 0.2.

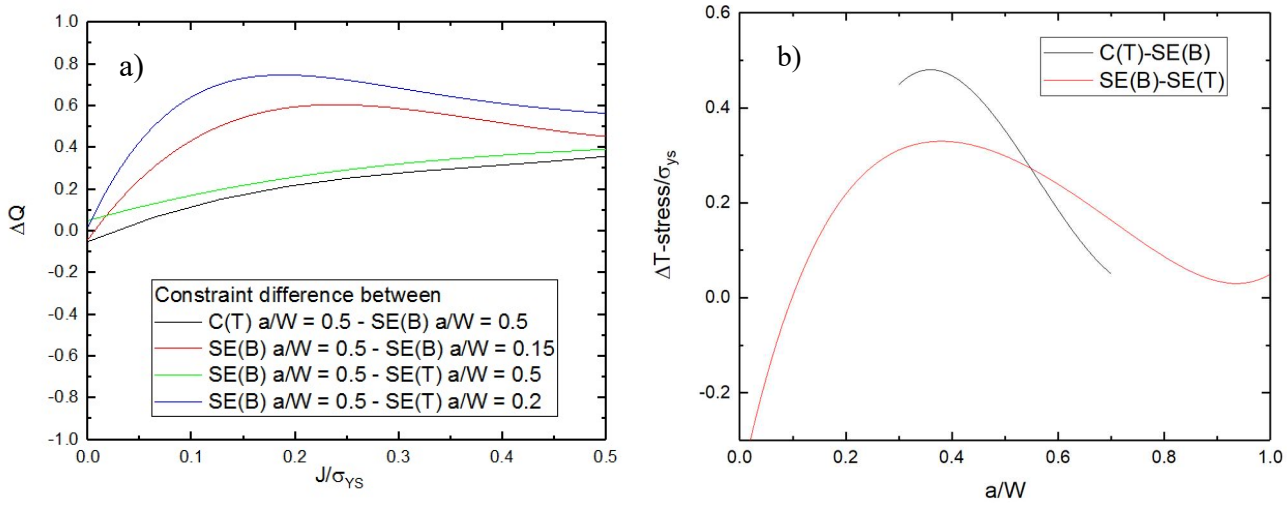

Figure 6. Difference in constraint between various geometries and crack lengths, a) Q-parameter and b) T-stress.

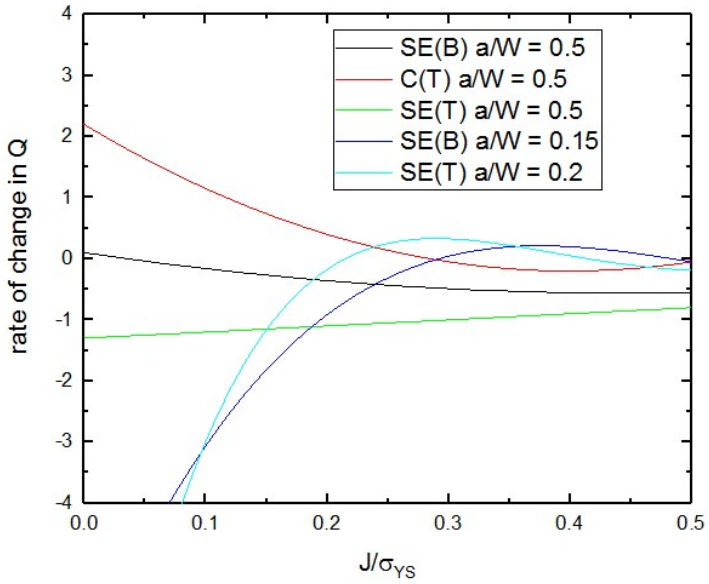

Figure 7. Rate of change in Q for different specimens and crack lengths.

Figure 8 shows the effect of constraint for the median Master Curve. The K_{Jc} is transformed first to J (**Figure 8** *b)*, then to J/σ_{YS} (**Figure 8** c), and finally to Q with equations (24) to (28) (**Figure 8** d). **Figure 8** d) shows the change in Q for the different geometries as a function of T-T_0. T-T_0 = 0 is associated to 100 MPa$\sqrt{\text{m}}$. At 100 MPa$\sqrt{\text{m}}$, the Q for C(T) and SE(B) specimens with a/W = 0.5 is between 0 and 0.1, whereas for shallow cracked specimens the constraint is between -0.4 and -0.6. The variations in Q are caused by the sensitivity to load in the validity range of the master curve. A higher load is required to fracture a specimen as the temperature increases. The difference between Q determined at T_0 -50 °C and T_0 +50 °C is large. However, the T_0 determined at T_0 + and - 50 °C does not differ as much. Thus, it is not completely evident how the Q-parameter should be used and more work is required to clarify this issue.

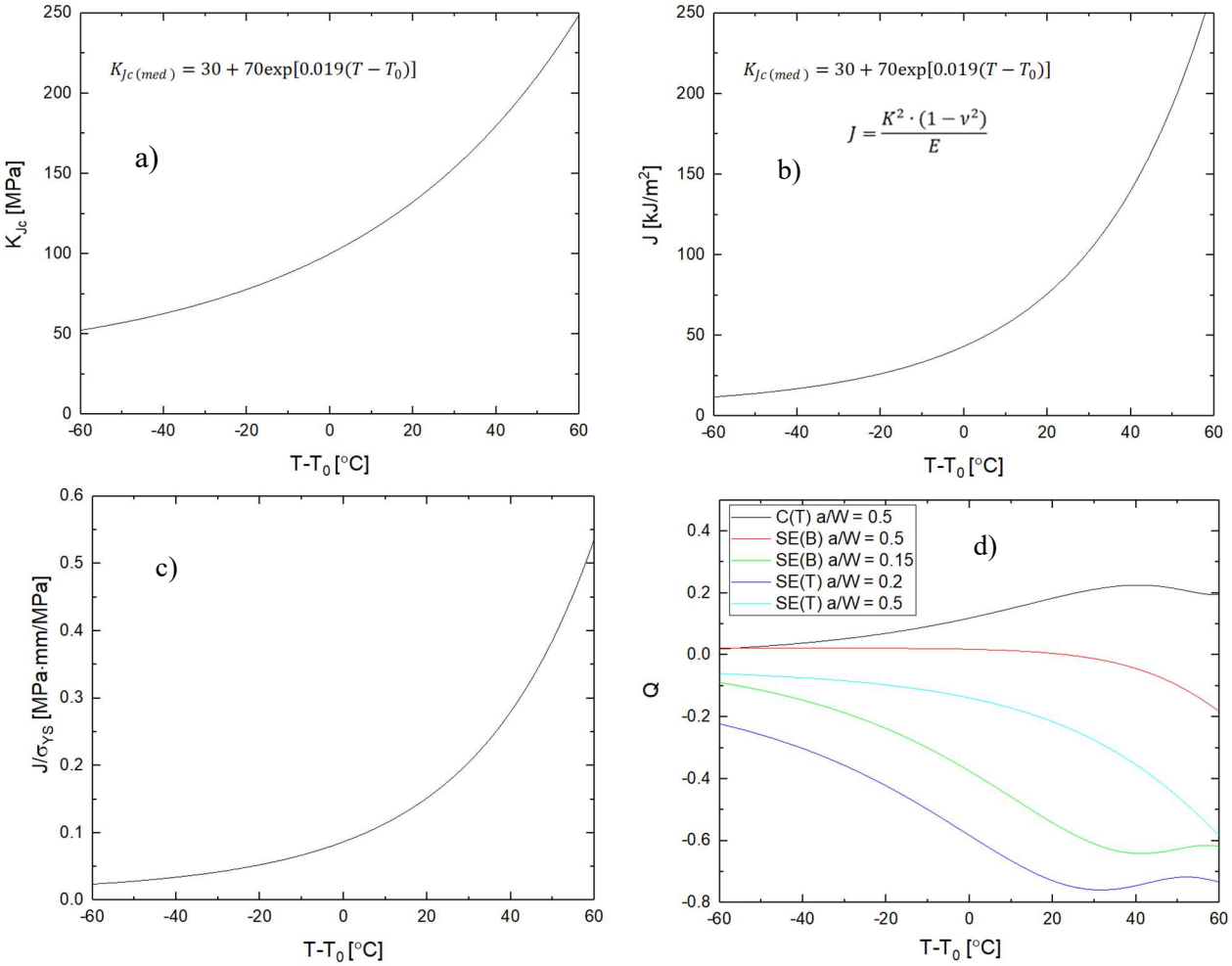

Figure 8. a) Median Master Curve, b) median Master Curve transformed to J c) J is normalised with σ_{YS} = 500 MPa d) J/σ_{YS} transformed to Q with equations *(24) to (28)*). The equations do not account for the change in strength with changing temperature.

Figure 9 shows the decrease in constraint along a straight crack front (Garwood 2018). The specimen exhibits a constraint loss at the edges close to free surface. To avoid constraint loss at the edges, side-grooves are typically used in fracture toughness specimens.

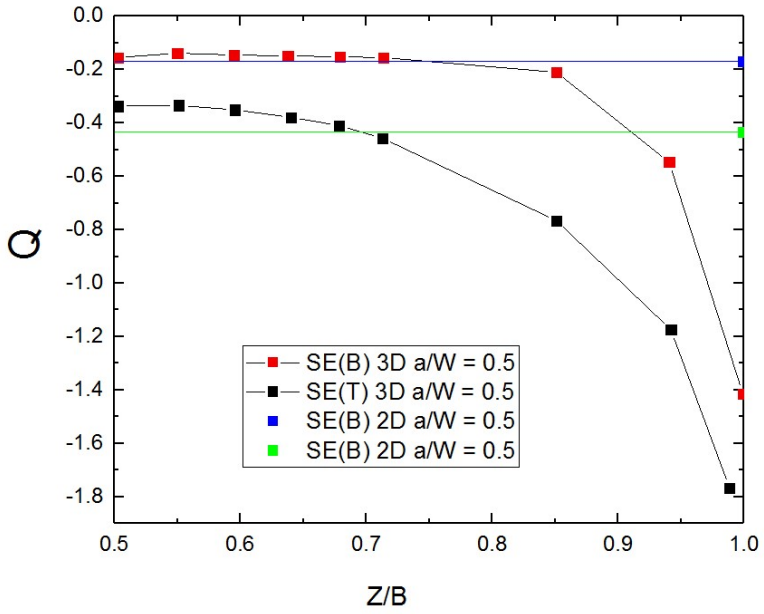

Figure 9. Variation of Q along the crack front. Q was determined at limit load. Note that the data is plotted from the specimen mid-plane where symmetry prevails.

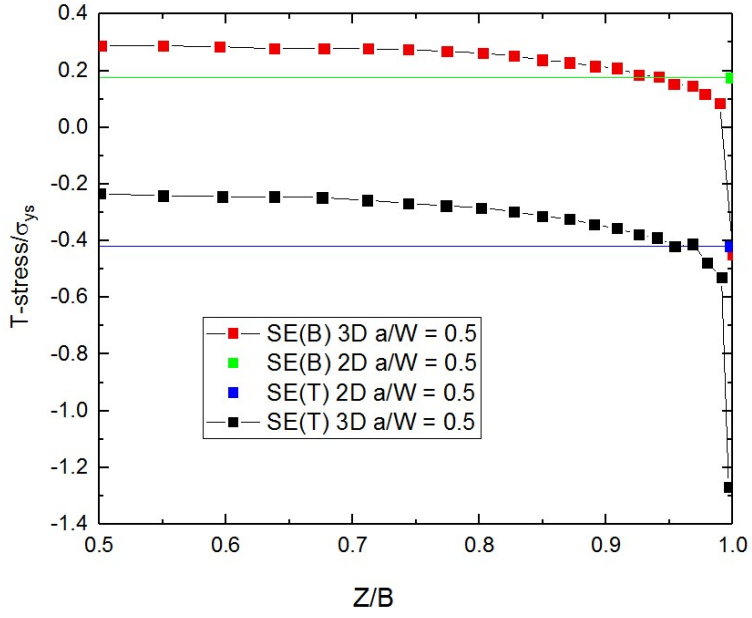

Figure 10. Variation of T-stress along the crack front. Note that the data is plotted from the specimen mid-plane where symmetry prevails.

2.5 Predicting the effect of constraint on T_0 and J_{1mm}

2.5.1 Constraint and T_0

The latest engineering procedure for assessment of the effect of constraint on T_0 has been developed by Moattari & Sattari-Far (Moattari and Sattari-Far 2017) based on the Q-parameter as

$$\Delta T_0 = T_0 - T_0^{ref} = 48.62(Q - Q_{ref}). \tag{29}$$

The Moattari & Sattari-Far constraint dependence is compared to the *T*-stress dependence developed by Wallin (equations (4) and (5)) in **Figure 11**. The dependency developed by Wallin is conservative relative to the Moattari & Sattari-Far dependence.

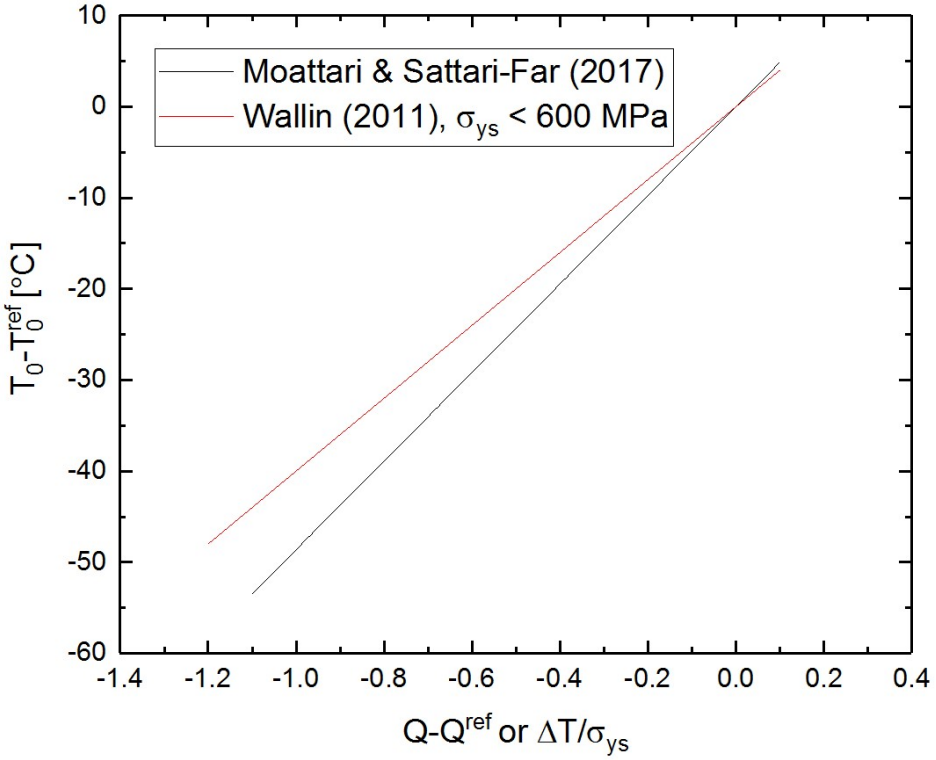

Figure 11. The effect on change in constraint on T_0.

The Moattari & Sattari-Far dependence was developed by calculating a reference constraint parameter for a high-constraint 1T C(T) specimen with a crack of $a/W = 0.5$ and determining a reference T_0 value for the same geometry. After that the Q and T_0 for a low constraint geometry was determined. Furthermore, the Moattari & Sattari-Far dependence was determined based on normalised load (J/σ_{ys})-constraint curves, resulting in yield stress insensitive curves. This modification enables calculation of the Q-parameter at any arbitrary temperature in the transition region.

However, determination of the Q is not as straight forward, since constraint is dependent on the load. Moattari & Sattari-Far solved the problem by determining two T_0-Q dependencies at two different loads. The other dependence was determined for Q at 100 MPa$\sqrt{\text{m}}$ corresponding to median fracture toughness at T_0 and the other for Q at 211MPa$\sqrt{\text{mm}}$ corresponding to median fracture toughness at T_0 + 50 °C, Figure 13. Figure 12 shows that a more conservative estimate of the T_0-Q dependence is obtained with Q determined at 211 MPa$\sqrt{\text{m}}$. The low yield strength at the higher temperature further decreases the slope of the T_0-Q dependence.

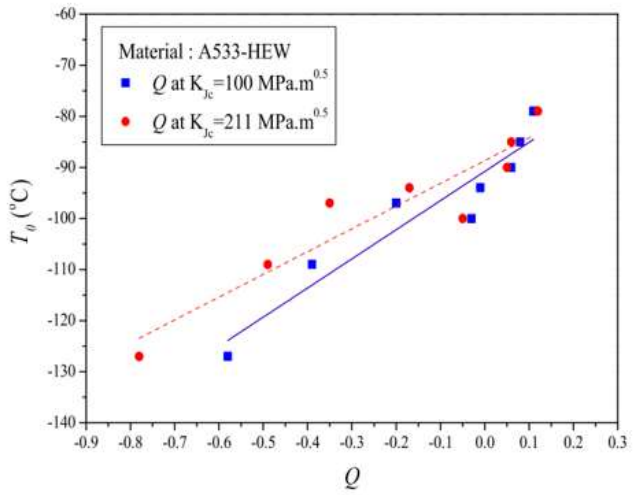

Figure 12. The difference in the slope of the constraint-T_0 dependence for Q determined at 100 MPa$\sqrt{m}$ and at 211 MPa$\sqrt{m}$. The Q determined at a larger load gives a smaller effect of Q on T_0.

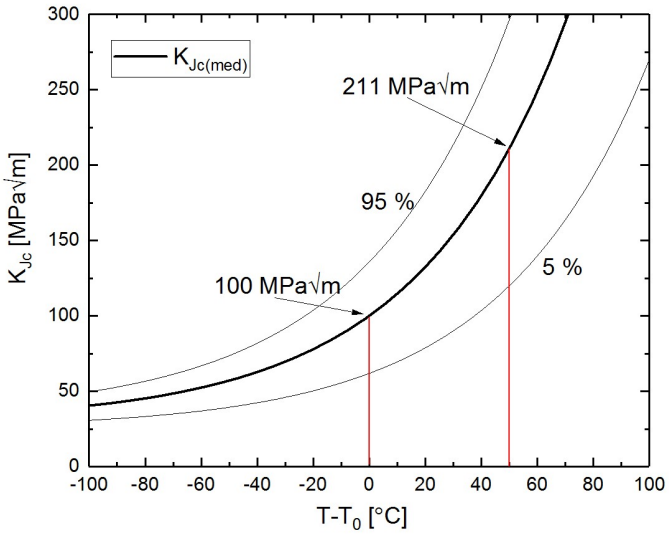

Figure 13. The Master Curve. The median and average load required to cause fracture at T_0 is 100 MPa$\sqrt{m}$and at T_0 + 50 °C 211 MPa$\sqrt{m}$.

Table 1 summarizes the materials, range of the constraint, specimens, crack lengths, T_0 range and yield strengths of materials used for developing the T_0 and constraint dependencies by Wallin and Moattari & Sattari-Far. The dependencies are dependent on the strength of the material and are valid in a range between 300 to 600 MPa. Wallin (2011) noticed that the dependence changes for materials with a yield strength above 600 MPa.

Further development work is required for the dependencies. The applicability of the dependencies for high strength materials, and the effect of the load at which constraint is determined for a specific test needs further research. The dependencies should also be validated for more materials of different strengths, since the constraint in the transition region is affected by the strength of the material. This way a formula (based on an extensive database) to assess the effect on constraint on T_0 can be developed for structural integrity analysis. This database could also be used for irradiated materials, since irradiation results into an increase in the yield strength. Development work is also required for selecting the

right type of specimen configuration for characterization of the effect of constraint, so that the experimental uncertainties can be reduced and significant effect of constraint can be observed.

Table 1. The conditions accounted for in the T0-constraint dependencies developed by Moattari & Sattari-Far and Wallin. *The T0-constraint dependence changes for materials with yield strength above 600 MPa.

Reference	Materials	Constraint range	Specimens and crack length	T_0 range [°C]	Yield strength at test temperature [MPa]
Moattari & Sattari-Far (2017) (Moattari and Sattari-Far 2017)	A533-HEW, A533 GrB, A508, 18MND5, 22NiMoCr37, A516 Gr70	Q-parameter; -0.9 - 0.2, determined at 211 MPa$\sqrt{m}$	C(T) (a/W = 0.5), SE(B) (0.1 < a/W < 0.5), Biaxial Bend (a/W = 0.1), CC(T) (a/W = 0.7),	-142 < (T_0 or T_{0q}) < -30	300 < YS < 640
Wallin (2011) (Wallin 2011)	A533B, A508	T-stress/YS; -0.85 - 0.4, determined at limit load	C(T), SE(B), SE(B), Biaxial, SC(T), SE(T), DE(T), CC(T)	-165 < (T_0 or T_{0q}) < 50	300 < YS < 600 and *(600 < YS < 850)

2.5.2 Constraint and J_{1mm}

The J-R curves can be described by $J_{1mm} \cdot \Delta a^m$. J_{1mm} is dependent on constraint whereas m is less sensitive to the constraint. In the ductile regime, the constraint has been observed to have a small effect on the initiation toughness, but the effect on the *J-R* curve can be larger. The effect of constraint on J_{1mm} can be predicted with

$$\frac{J}{J_{T>0}} \approx \left\{ exp - \left(\frac{T - stress - 100\,MPa}{1500\,MPa} \right) \right\}^2 , \text{ for } T_{stress} \leq 100\ MPa, \tag{30}$$

which should be used with caution since the effect of constraint on the *J-R* curves is dependent on the ductile fracture mechanism. If the ductile process is controlled by shear stresses, the decrease in constraint can have a decreasing effect on the tearing resistance. The equation is valid for materials controlled by hydrostatic stresses that control the void growth, and thus, crack growth.

Equation (30) is based on *T*-stress and not *T*-stress/σ_{ys}. The problem with applying the *Q* and *T*-stress/σ_{ys} constraint parameters for ductile materials is that the parameters are inversely related to the yield strength that is inversely related to strain hardening. A low yield stress material has typically a high strain hardening capacity. This reduces the sensitivity to geometrical constraint. For materials with high yield stress, the strain hardening is typically low leading to more localized plasticity and a higher sensitivity to geometrical constraint.(Wallin 2011)

2.6 Constraint of cracks in structures

Real cracks in a structures are three dimensional in shape. In structural integrity analyses, the cracks are approximated as elliptical. **Figure 14** a) shows an elliptical surface crack in a plate loaded in tension and simultaneous bending, and **Figure 14** b) and **Figure 15** show characteristic dimensions applied for describing the dimensions of a surface crack. Both the stress intensity and constraint varies along the crack front, and in case of a thermal shock event the temperature will vary along the crack front. **Figure 16** shows the variation of the *J*-integral along the crack front for an elliptical surface crack in a plate loaded in tension and assuming elastic plastic material behavior. The *J*-integral is largest in the central region. For long cracks (*a/c* =0.2), the dependence in **Figure 16** differs only close to the surface from a more accurate analysis accounting for the biaxial loading. Biaxial loading has a larger effect on semi circular flaws (*a/c* =1). (Wallin 2011)

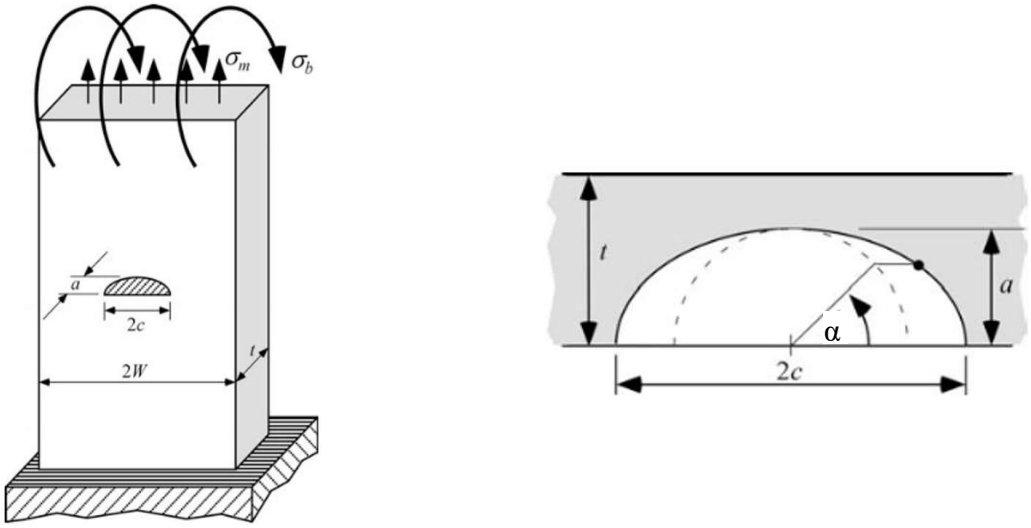

Figure 14. a) A plate with a surface crack under a tensile and a bending load. b) The characteristic features for identifying an elliptical surface crack; t is the thickness, 2c is the length of the crack opening and a is the crack depth. The location along the crack front can be determined with α determined through a circular virtual flaw. The location along the crack front can also be determined with the actual angle Φ.

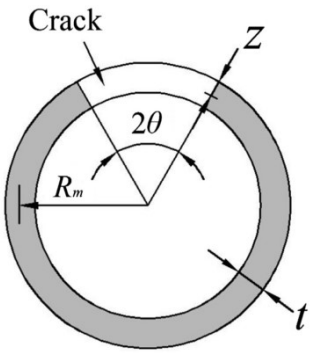

Figure 15. The length of the crack opening in a pipe can be determined with angle θ.

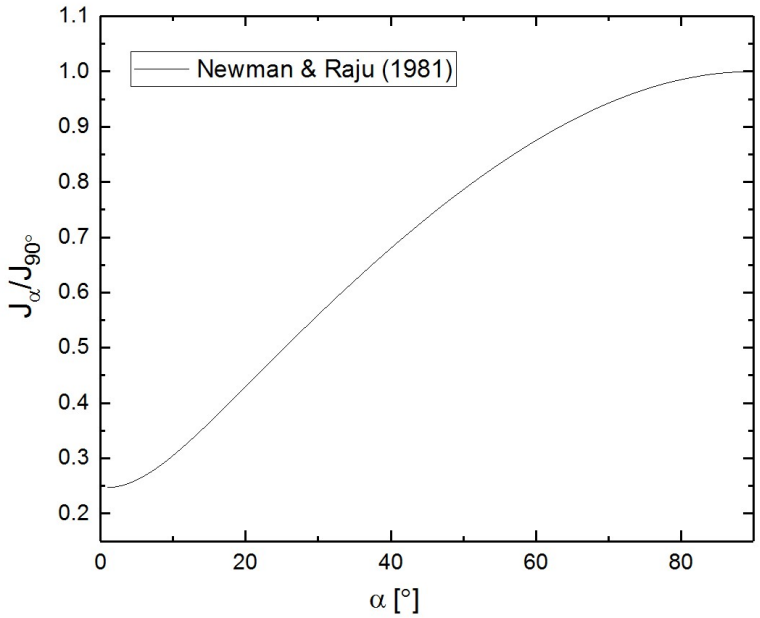

Figure 16. The normalized J-integral ahead of an elliptical flaw along the crack front. *(Anderson 2005)*

The constraint ahead of an elliptical surface crack can be estimated with

$$Q = (-0.5 \pm 0.1)\frac{\sigma}{\sigma_{ys}} \text{ for } \frac{\sigma}{\sigma_{ys}} = 0.5 - 1.1, \tag{31}$$

for long cracks (a/c = 0.2) of both deep (a/t = 0.5) and shallow flaws (a/t = 0.2) (Wallin 2011). The equation applies for both uniaxial and biaxial loading. The stress normalized Q is relatively constant ahead of the deepest location of the crack. By assuming a load of $\frac{\sigma}{\sigma_{ys}} = 1$, the effect of the constraint difference on T_0 for a C(T) specimen with a/W = 0.5 and a component with an elliptical flaw is roughly -25 to -30 °C according to equation (29). The constraint predicted by Equation (31) deviates from the actual constraint at angles smaller than the apparent angle α of 30°. This corresponds to an actual angle Φ of 7°. Closer to the surface the constraint can be higher due to biaxial loading.

Figure 17 shows the effect of constraint on the median/average Master Curve for a C(T) specimen with a/W = 0.5 and a low constraint SE(T) specimen with a/W = 0.2. The constraint of a SE(T) specimen is similar to that of a shallow crack in a pipe. Based on the constraint difference, the T_0 decreases with ΔT_{0Q} = -25 °C, **Figure 11** and the median Master Curve moves to the left.

The constraint can also affect the shape of the Master Curve due to the sensitivity of Q to J. The difference in Q for a conventional SE(B) specimen and a low constraint SE(T) specimen as a function of J was determined with equations (25) and (27). The effect of this constraint difference, $\Delta Q(J)$, on the Master Curve was assessed by inserting the $\Delta Q(J)$ equation and equation (29) in the median Master Curve formula, equation (32). With these equations, the effect of $\Delta Q(J)$ on the shape of the Master Curve can be solved iteratively. Consequently, **Figure 17** shows (the green curve) that the median Master Curve can be steeper for a low-constraint SE(T) specimen.

$$K_{Jc(med)} = 30 + 70\exp\left[0.019\left[T - \left(T_{0,ref} + 48.62Q(J)\right)\right]\right] \quad (32)$$

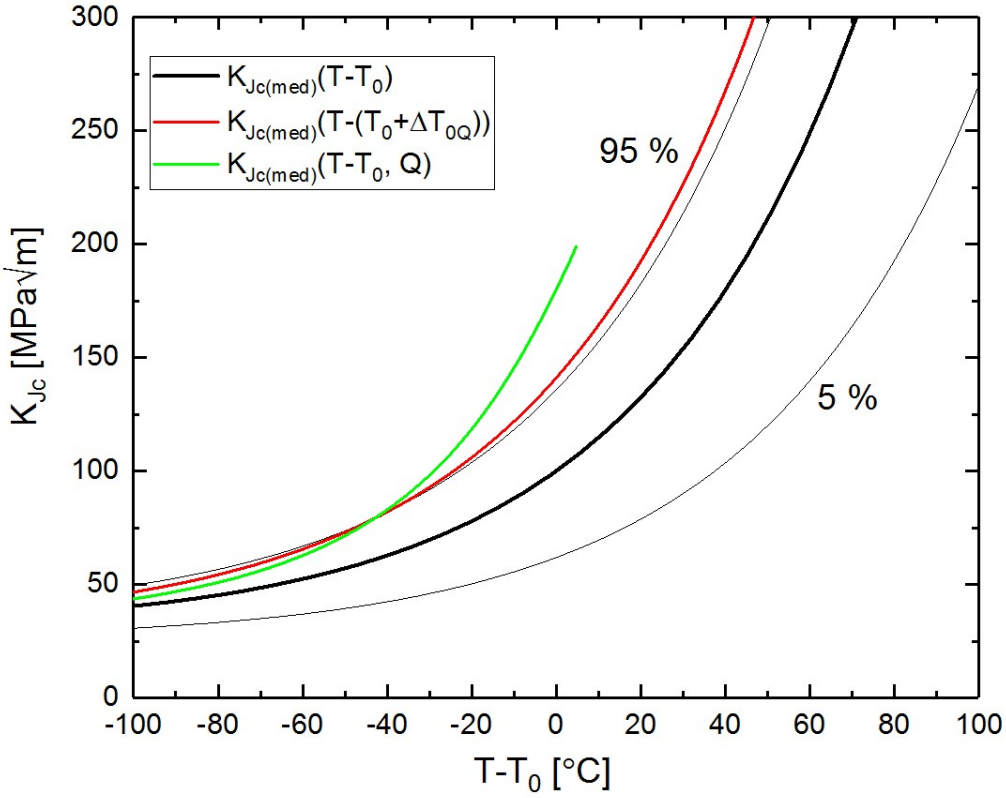

Figure 17. The effect of constraint on the mean/median Master Curve.

In real conditions for real cracks, the probability of brittle fracture is, in addition to the constraint, also affected by the crack front length and by possible ductile crack growth, loading rate and the temperature difference ahead of the crack. These topics are outside the scope of this work. (Wallin 2007)

3 Modelling of constraint and specimen selection

3.1 Predictions of size and constraint effects on fracture toughness

Here the conformity of the two models reviewed in Section 1.2 will be explored with respect to two datasets pertaining to constraint effects on cleavage fracture from the literature. The first set is taken from Faleskog et al. (Faleskog, et al., 2004) where an A508-steel with a T_0= 44 ˚C was tested at three temperatures T = {-30, 25, 55} ˚C using SEN(B)-specimens with a W = 40 mm and varying crack sizes as a/W = {0.5, 0.25, 0.1}.

The second set is taken from Rathbun et al. (Rathbun, et al., 2006) where an A533-steel with T_0= -93 ˚C was tested at T = -91 ˚C in order to study size effects on cleavage fracture toughness using SEN(B)-specimens by keeping a/W = 0.5 constant but varying W and B/W. The specimens selected from the Rathbun dataset were W = {25.4, 12.7, 6.4} mm with corresponding B/W = {5, 2.5, 1.25}.

Models of the fracture tests for evaluation of the failure probability according to Equation (8) were set up as finite element models. These were generated using meshes containing 27 000-35 000, 20 noded hexahedral elements with quadratic shape functions and reduced integration. Due to symmetry, only a quarter of the three point bend specimens were modelled with 12-15 elements through the thickness of the model. A high mesh density was used in the close vicinity of the crack front in order to resolve the stress and strain fields for the probabilistic calculations of the weakest link model. In all simulations, the elastic modulus E and Poisson's ratio v were taken as 210 GPa and 0.3, respectively. The elastic-plastic material was assumed to obey the J_2 flow theory of plasticity with isotropic hardening. Tensile tests data from the experimental programs in (Faleskog, et al., 2004) and (Rathbun, et al., 2006) were fitted to a power law hardening relation.

As mentioned above, model parameters of the non-local weakest link model demands to be estimated from calibration datasets, where two sets with differing crack tip constraint are needed. In all the datasets presented here, the sets chosen for calibration have the largest difference in crack tip constraint within the dataset and are thus most eligible for parameter estimation. Predictions of the failure probability from the master curve methodology are based on the T_0 and the yield stress σ_Y of the material, specimen thickness B, and the T-stress for which the solution of a SEN(B)-specimen was taken from (Wallin, 2001).

The probability of failure was evaluated from the master curve through (1) and from finite element models of the fracture test through (8) and can be seen in Figures 18 - 21, where also rank probability data from the experiments within each set is shown. Generally, it can be said that the results from the non-local weakest link model conforms better to the experiments studied in this report than the master curve. However, the non-local weakest link model demands a lot more in input data than the master curve methodology, i.e. elastic-plastic flow data, more extensive calibration datasets, detailed finite element solutions, etc. The strength of the master curve methodology is that it is a versatile engineering method which is easy to use and that it is capable of predicting the temperature dependence, something which is still lacking in the non-local weakest link model. This is also more clearly shown in **Figure 18** (T=-30 ˚C) and **Figure 20** (T=55 ˚C) where the master curve predictions conforms well with

the experiments at $P_f = 0.8$ and 0.3 for the deeply cracked specimens. This gives a prediction that evens out over the temperature range. It should also be noted that the dataset $W = 6.4$ mm associated with the Rathbun dataset well violates the specimen measurement capacity according to ASTM E1921 (ASTM International, 2016).

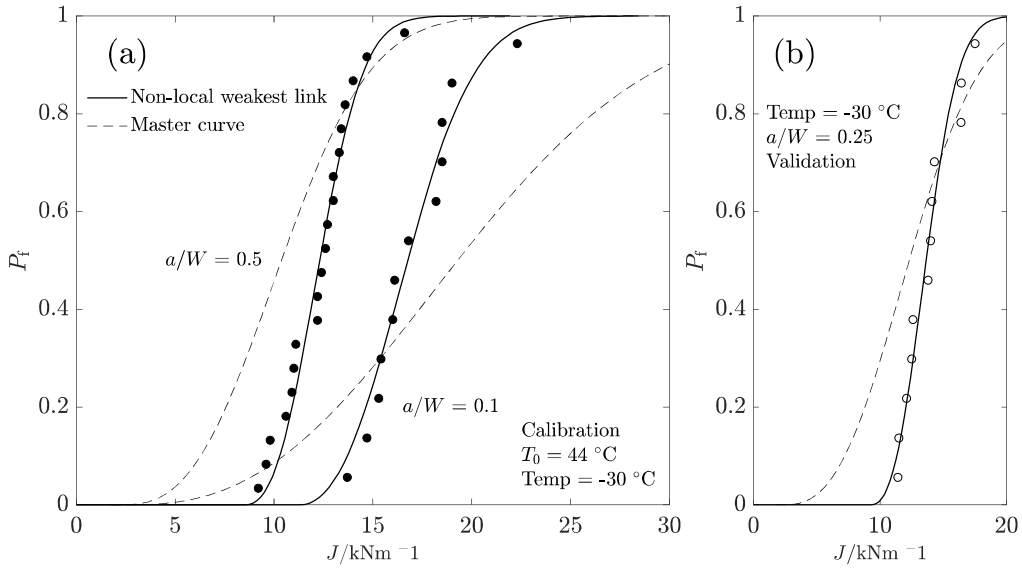

Figure 18. Comparison of predictions of the failure probability and ranked experimental data for the Faleskog T = -30 ˚C dataset, (a) Calibration sets for the non-local weakest link model, (b) Validation set for the non-local weakestlink model.

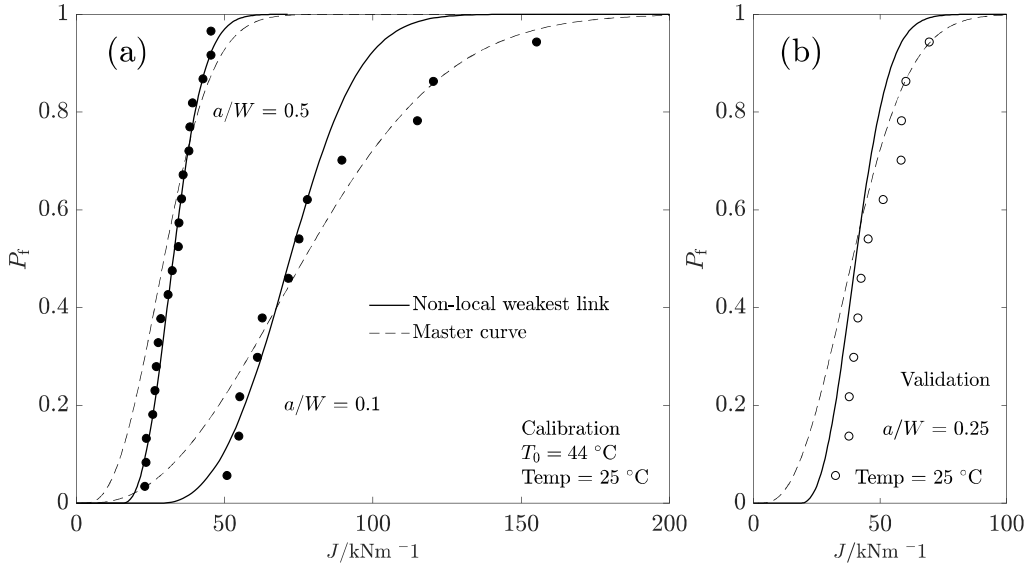

Figure 19. Comparison of predictions of the failure probability and ranked experimental data for the Faleskog T = 25 ˚C dataset, (a) Calibration sets for the non-local weakest link model, (b) Validation set for the non-local weakestlink model.

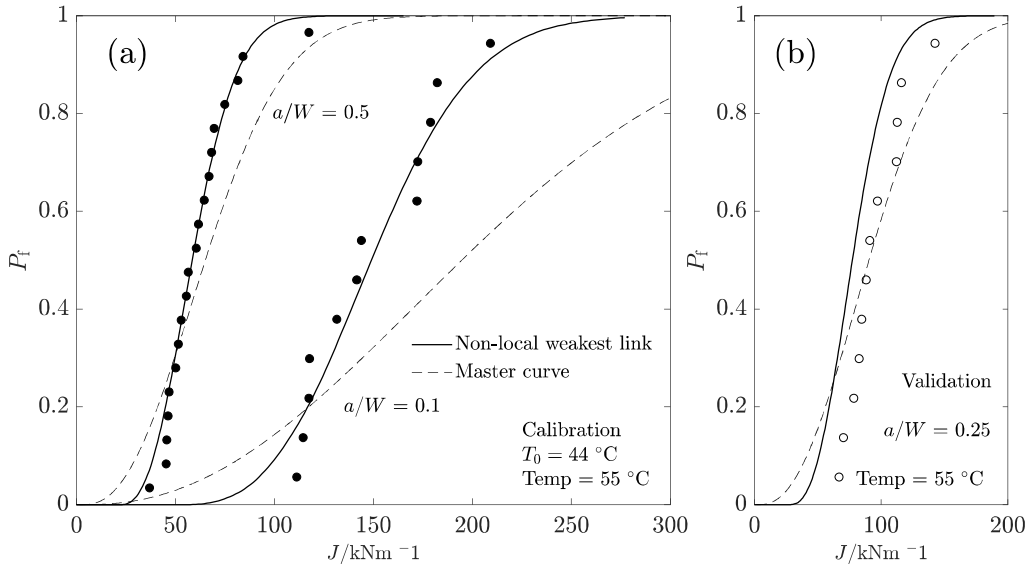

Figure 20. Comparison of predictions of the failure probability and ranked experimental data for the Faleskog T = 55 ˚C dataset, (a) Calibration sets for the non-local weakest link model, (b) Validation set for the non-local weakestlink model.

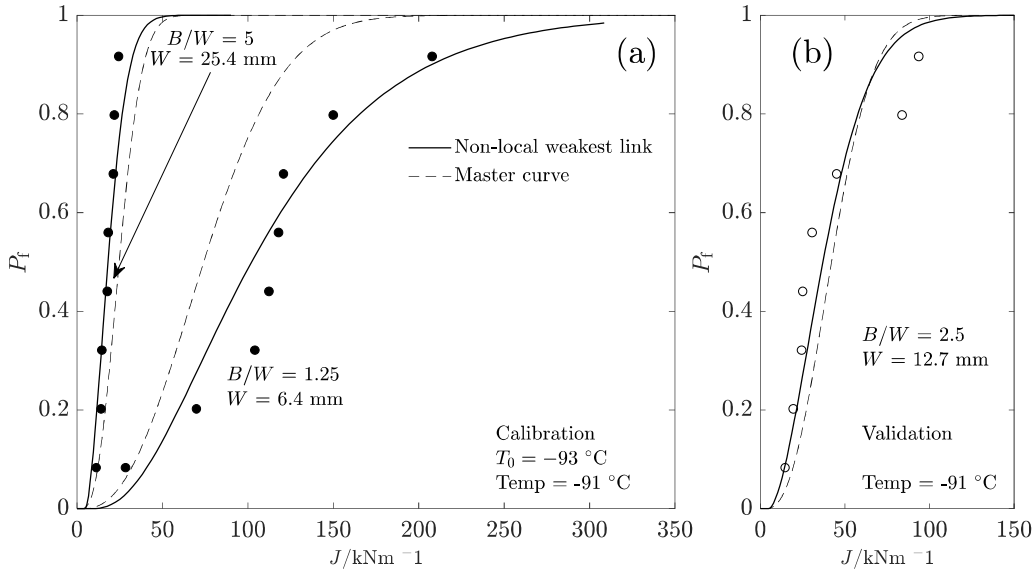

Figure 21. Comparison of predictions of the failure probability and ranked experimental data for the Rathbun dataset, (a) Calibration sets for the non-local weakest link model, (b) Validation set for the non-local weakestlink model.

3.2 Selection of specimen configuration for constraint testing

Several factors have been identified as important in the process of selecting specimens that are viable for testing of the effect of constraint on the cleavage fracture toughness, among these are:

- Material availability,
- specimen measurement capacity,
- manufacturability of specimens,
- ensured difference in constraint between specimens.

With these factors in mind, the models detailed above have been used to predict the necessary bounds on specimen size, testing temperature, and potential risks associated with constraint testing.

The temperature dependence of the yield σ_Y and ultimate tensile stress σ_{UTS} used in the calculation of the measurement capacity of the specimens is taken from British Standard (BSI Standards Publication, 2013) and is written on the form

$$\sigma_Y(T) = \sigma_Y(T = 25\,^{\circ}\mathrm{C}) + \frac{10^5}{(491 + 1.8T)} - 189, \tag{33}$$

$$\sigma_{UTS}(T) = \sigma_{UTS}(T = 25\,^{\circ}\mathrm{C})\left(0.7857 + 0.2423\exp\left(-\frac{T}{170.646}\right)\right), \tag{34}$$

which are valid on the interval $-194\ ^{\circ}\mathrm{C} < T < 25\ ^{\circ}\mathrm{C}$, where T is the temperature.

3.2.1.1 C(T) and SEN(B)-specimens

The compact tension C(T) and the single edge notch bend SEN(B) specimens are two types of specimens that have been rigorously analyzed and used for fracture testing. Both specimen types can be used for high constraint testing and are well suited for use with the master curve methodology. However, it has been shown that the C(T)-specimen yields a slightly higher T_0 (more conservative) due to having a higher geometrical constraint than the SEN(B)-specimen (Wallin, et al., 2001). This, along with a smaller material usage is the main advantages of the C(T)-specimen. The downside is that low constraint testing is impossible, which is well explained by the fact that the T-stress remains high for crack depths that are possible to test. Shallow crack testing may result in deviating crack paths and too high load levels on the loading pins.

In the remaining part of this section, model parameters from the Faleskog T = 25 ˚C dataset are used. The parameters pertaining to the master curve are T_0 = 44 ˚C, and a yield stress σ_Y = 666 MPa (average of R_{P02} and σ_{UTS}). The parameters pertaining to the non-local weakest link model $c/V_0 = 157.80 \cdot 10^{10}$ 1/m^3, σ_{th}= 1551.8 MPa, and L = 150 µm. For the constraint correction of the master curve the yield stress independent correction where A = 40 ˚C has been used throughout this section.

By employing both the master curve methodology and the non-local weakest link model (parameters from Faleskog T = 25 ˚C), it is shown in **Figure 22** how shallow flaw testing of C(T)-specimens is predicted to not result in loss of constraint. The fracture toughness from the non-local weakest link model is taken at a failure probability of 50 %. This clearly

indicates that the state of high constraint is preserved in a C(T)-specimen for all practical crack depths.

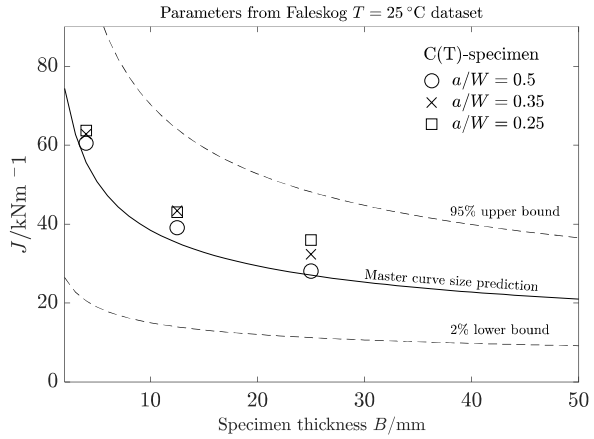

Figure 22. Predictions of the fracture toughness in a C(T) from the master curve methodology (solid and dashed lines) and the non-local weakest link model (symbols)

The SEN(B)-specimen is well suited to achieve a state of loss of crack tip constraint. The effect of crack size and specimen thickness on the fracture toughness of a SEN(B)-specimen has been explored using both the non-local weakest link model and the master curve methodology in **Figure 23**. The effects can be seen through that the fracture toughness is greatly increased for shallow cracks in comparison to deeply crack specimens. A good conformity is shown between the two models where the open symbols from the non-local weakest link model represent the fracture toughness at a failure probability of 50 % and the solid line is the 50 % master curve prediction.

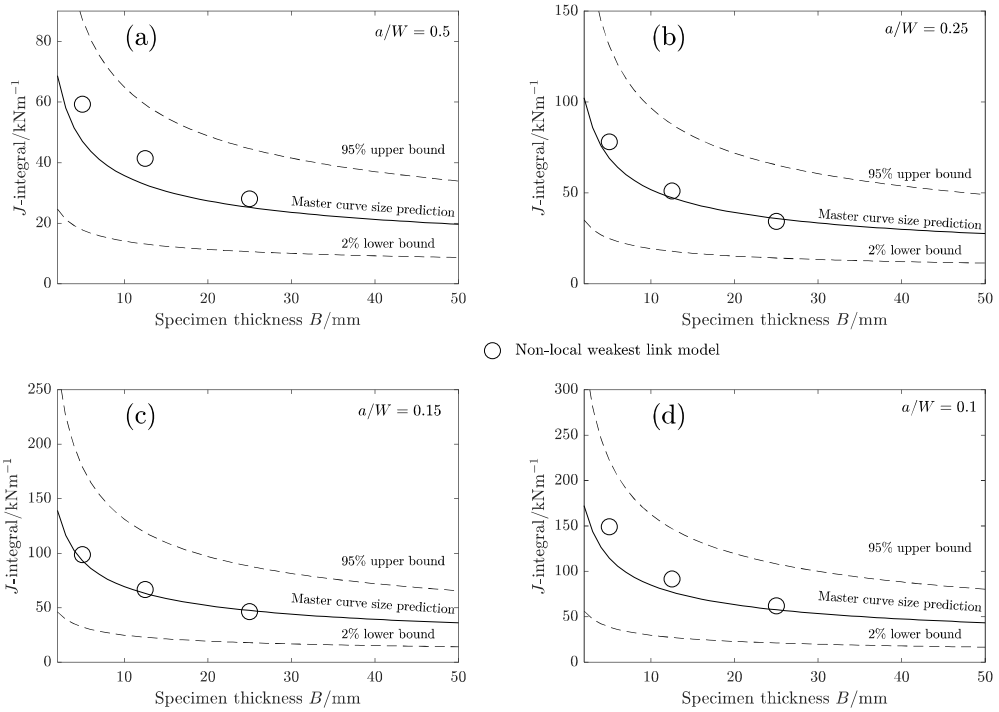

Figure 23. Predictions of the fracture toughness from the master curve methodology (solid and dashed lines) and the non-local weakest link model (symbols). Effects of varying crack depths and specimen thickness (a) a/W = 0.5,
(b) a/W = 0.25, (c) a/W = 0.15 and (c) a/W = 0.1.

From the analysis carried out here, it is can be seen that the predictions of the master curve and the non-local weakest link model gives are similar in this case with respect to crack depth and thickness.

The specific case of constraint testing using small specimens will now be addressed. In the case of a limited supply of material, fracture testing for the cleavage fracture toughness can be carried out using small specimens (Wallin, et al., 2001), (Yamamoto, et al., 2015). It is pertinent to take several precautions when testing small specimens, for instance, the temperature window of getting valid tests is shrinking with diminishing specimen size, indicating that a greater number of specimens might be needed in order to have a valid test series. In the case of testing with loss of constraint, more variables are introduced into the test and it is therefore sensible to carry out all of the tests (high and low constraint) at the same temperature, given that this temperature can be chosen based on T_0 so that the temperature and censoring requirements of ASTM E1921 can be fulfilled. Thus making master curve analysis of the data possible. Analysis of the data using the non-local weakest link model requires tensile test data at the fracture test temperature.

Due to handling and other practical reasons (such as measuring capacity), specimens below W = 8-10 mm are deemed too small. It is here assumed that a W = 10 mm and B = 5 mm will be suitable for fracture testing. In **Figure 24** predictions of the failure probability for a high constraint C(T)-specimen, and a low constraint SEN(B)-specimen with a/W ={0.5 and 0.15} respectively, at T = 25 ˚C from both the non-local weakest link model and the master curve methodology can be seen, the measuring capacity of the specimens is also shown. The upper

tail of the toughness distribution is not covered by the measuring capacity, indicating that either a lower temperature or a larger specimen needs to be used. The two models yields very similar predictions for this choice of parameters,. As the non-local weakest link model lacks in being able to model the temperature dependence, the master curve methodology will hereon be used to find suitable parameters for constraint testing using small specimens.

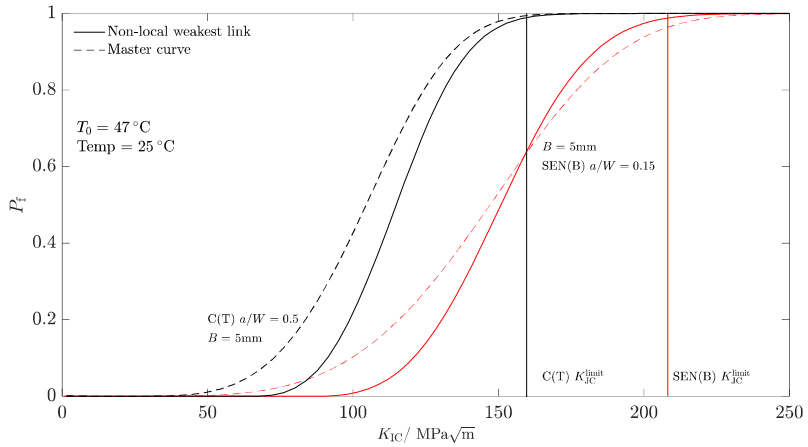

Figure 24. Predictions of the failure probability of a high constraint C(T) specimen with a/W = 0.5, and a low constraint SEN(B)-specimen with a/W = 0.15 at a temperature of $\mathbf{T - T_0 = -19}$ ˚C using both the master curve methodology and the non-local weakest link model. The measuring capacity of the specimens is added as vertical lines.

In order to satisfy the bounds of the measuring capacity of the specimen at $W = 10$ mm, the temperature is lowered to $T - T_0 = -30$ ˚C which results in the predicted failure probability shown in **Figure 25**. At this temperature, the entire toughness distribution fits within the bounds of the specimen measuring capacity. If more safety is needed with respect to the measuring capacity, the temperature can be lowered further without violating the temperature bounds in (ASTM International, 2016).

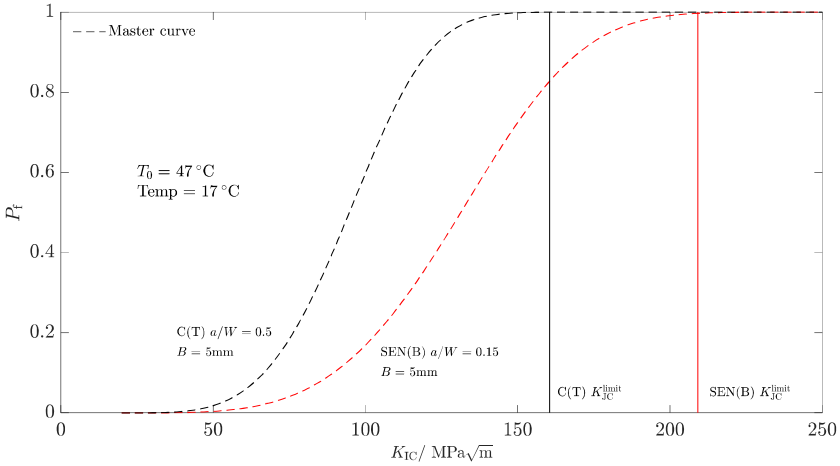

Figure 25. Predictions of the failure probability of a high constraint C(T) specimen with a/W = 0.5, and a low constraint SEN(B)-specimen with a/W = 0.15 at a temperature of 10 ˚C using the master curve methodology. The measuring capacity of the specimens is added as vertical lines.

3.2.1.2 Risks related to testing for constraint effects on fracture toughness

Fracture testing using small specimens of a limited amount of material carries some potential risks that may need to be accounted for. The manufacturing imposes a difficulty in producing short cracks due to problems in estimating crack size during the pre-fatigue process using the CMOD-compliance method. However, this can be remedied on a SEN(B)-specimen by using a front face strain gauge from which the crack size can be estimated. The strain gauge should be applied at a distance of $0.125W$ from the crack plane, as indicated in **Figure 26**. The signal is used to calculate a strain-compliance C which is used in the following expression

$$U = C\frac{EBW^2}{1.5s}, \qquad \text{if } U > 0.9365 \text{ then } U = 0.9365, \tag{35}$$

where E is the elastic modulus of the material. The value of U is then used in the following polynomial to estimate the crack size

$$\frac{a}{W} = 0.177 - 0.4039U + 0.5604U^2 - 0.3532U^3. \tag{36}$$

The expression supplied here is valid for specimens with a span of $s = 4W$ and is only be valid for shallow cracks as the expression in (36) becomes zero for cracks larger than $0.177W$. The accuracy of the expression will diminish for crack sizes larger than $0.15W$, which is regarded

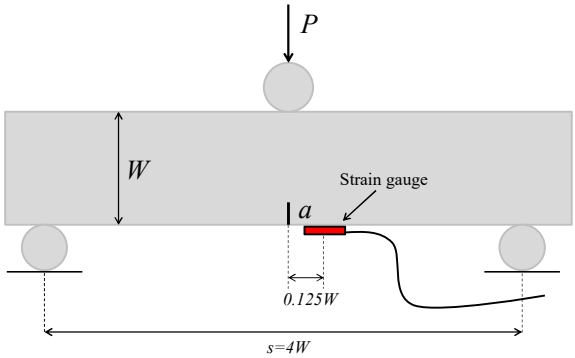

Figure 26. Illustration of placement of strain gauge for crack size estimation in the special case of shallow cracks.

as an upper bound for this method.

It should be noted that for small specimens (W = 10 mm), as explored above, then the strain-compliance method for estimating crack size needs to be altered due to that $0.125W$ is too close to the crack plane for a strain gauge to be practically applied. This will be remedied by extending the above method to a variable gauge position, however, this is not covered in this report.

If for example weld material is to be tested, there is a risk that the material exhibits a degree of inhomogeneity. In the master curve methodology, this can be speculatively described by the above reviewed bimodal master curve. By adding a low value of $T_{01} = 7$ ˚C to the already existing $T_{02} = 44$ ˚C and a probability of occurrence of $p_a = 0.45$ a bimodal master curve can artificially produced to be used a speculative tool. Also, it is speculated that the T-stress adjustment of the master curve will apply to only the lower of the two T_0 values, since the

toughness values stemming from this part of the distribution will be subjected to a larger degree of plastic deformation and thereby also a more significant loss of constraint. Continuing the analysis and applying it to the specimens that were found suitable from the unimodal master curve analysis, the graph of failure probability in **Figure 27** is obtained. It can clearly be seen that the specimen measuring capacity will not embrace the entire toughness distribution. To remedy this, two options exist where either the specimen size is increased or that the testing temperature is decreased, or a combination of the two. Both of these options are included in **Figure 28** and **Figure 29**.The fracture toughness as function of temperature for $W = \{7, 5\}$ mm is shown in **Figure 30**.

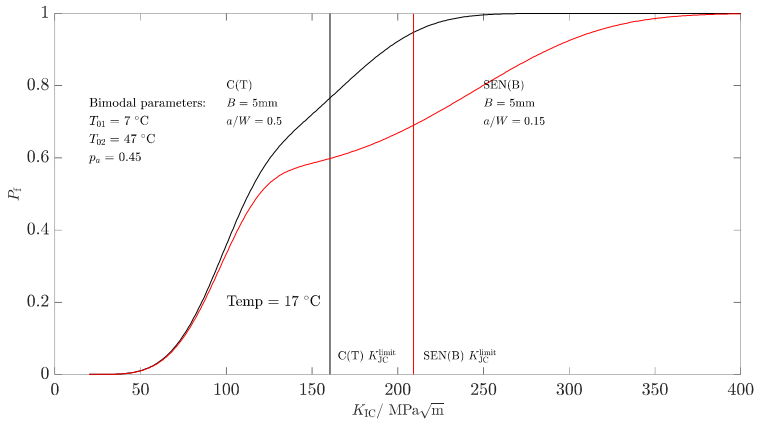

Figure 27. Predictions of the failure probability of a high constraint C(T)-specimen with a/W = 0.5 and a low constraint SEN(B)-specimen with a/W = 0.15 at a temperature of 10 ˚C using the bimodal master curve methodology. The measuring capacity of the specimens is added as vertical lines.

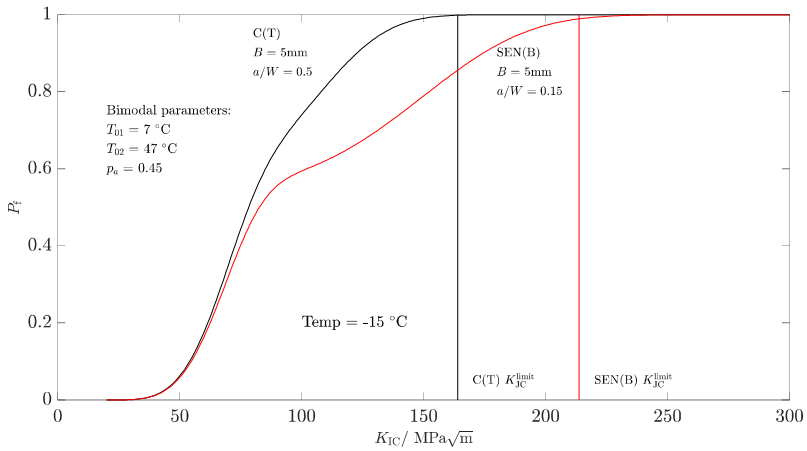

Figure 28. Predictions of the failure probability using the bimodal master curve methodology, effect of decreased temperature. The measuring capacity of the specimens is added as vertical lines.

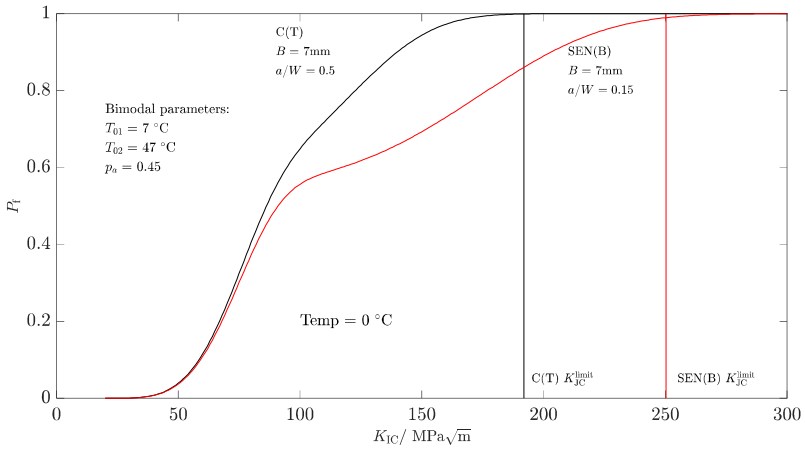

Figure 29. Predictions of the failure probability using the bimodal master curve methodology, effect of increased specimen size and a slightly lowered temperature. The measuring capacity of the specimens is added as vertical lines.

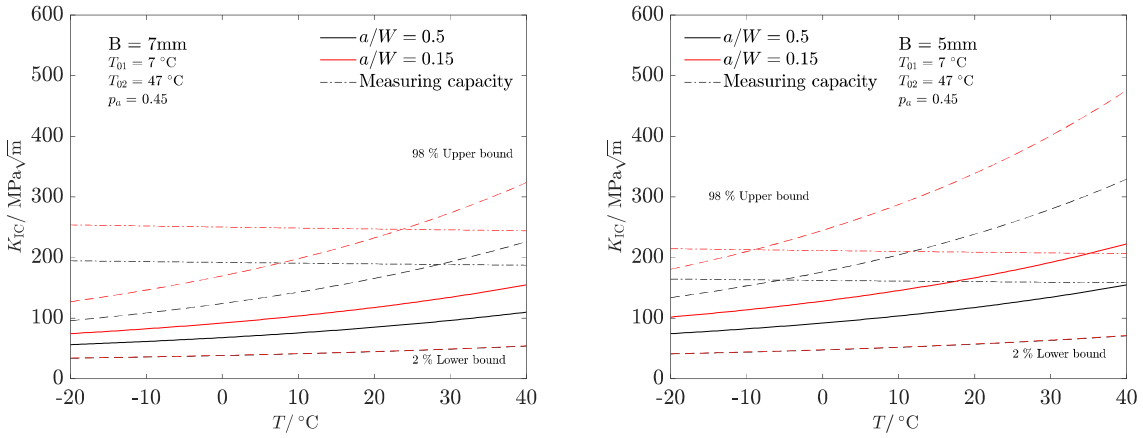

Figure 30. Prediction of fracture toughness as a function of temperature by using the bimodal master curve methodology. The measuring capacity is included as dashed-dotted lines in specimen specific color.

4 Concluding remarks

In Section 2, the constraint methodology was reviewed. The different constraint parameters were discussed and compared. The effect of constraint on fracture toughness was described. Engineering friendly methods for assessing the effect of constraint on T_0 were presented. The constraint difference between an elliptical surface crack and a conventional fracture toughness specimens was estimated to cause a 25-30 °C shift in T_0.

In Section 3, two models for predicting the probability of failure were briefly reviewed and applied to datasets from the open literature. This showed the generally better predictions of the experiments of the non-local weakest link model, but as the master curve methodology carries the capability of predictions across varying temperatures it was used in the final estimation of specimen size and temperature requirements. Potential risks such as pre-cracking problems and bimodal tendencies were also addressed in this report.

It was found that C(T) and SEN(B) specimens as high and low constraint configurations of size W = 10 mm and B = 5 mm will most likely be appropriate for testing of constraint effects on fracture toughness in the case of a limited availability of material.

Acknowledgements
Pål Efsing is acknowledged for the project management work.

NKS conveys its gratitude to all organizations and persons who by means of financial support or contributions in kind have made the work presented in this report possible.

The writing of this paper was partly funded by project LOST (Long term operational aspects of structural integrity) that is part of SAFIR2018 (The Finnish Research Programme on Nuclear Power Plant Safety 2015 - 2018).

References

Anderson TL (2005) Fracture mechanics: Fundamentals and applications, 3rd edn. Taylor & Francis Group, LLC.

ASTM E1820-15 (2015) Standard test method for measurement of fracture toughness. ASTM International, West Conshohocken, USA

ASTM International (2016) Standard Test Method for Determination of Reference Temperature, T0, for Ferritic Steels in the Transition Range, West Conshohocken: ASTM International.

BSI Standards Publication (2013) Guide to methods for assessing the acceptability of flaws in metallic structures, London: The British Standards Institution.

Faleskog, J., Kroon, M. & Öberg, H. (2004) A probabilistic model for cleavage fracture with a length scale - parameter estimation and predictions of stationary crack experiments. Engineering Fracture Mechanics, Volume 71, pp. 57-79.

Garwood SJ (2018) The effect of a low constraint geometry on measured T0 values for a nuclear reactor pressure vessel ferritic steel. 1–8

Hohe, J., Friedmann, V., Wenck, J. & Siegele, D. (2008) Assessment of the role of micro defect nucleation in probabilistic modeling of cleavage fracture. Engineeing Fracture Mechanics, Volume 75, pp. 3306-3327.

Hohe, J., Hardenacke, V., Luckow, S. & Siegele, D. (2010) An enhanced probabilistic model for cleavage fracture assessment accounting for local constraint effects. Engineering Fracture Mechanics, Volume 77, pp. 3573-3591.

International, A. (2016) Standard Test Method for Determination of Reference Temperature, T0, for Ferritic Steels in the Transition Range, West Conshohocken: ASTM International.

Kroon , M., Faleskog, J. & Öberg, H. (2008) A probabilistic model for cleavage fracture with a length scale - Parameter estimation and predictions of growing crack experiments. Engineeing Fracture Mechanics, Volume 75, pp. 2398-2417.

Kroon, M. & Faleskog, J. (2002) A probabilistic model for cleavage fracture with a length scale - influence of material parameters and constraint. International Journal of Fracture, Volume 118, pp. 99-118.

Moattari M, Sattari-Far I (2017) Modification of fracture toughness Master Curve considering the crack- tip Q-constraint. Theor Appl Fract Mech 90:43–52 . doi: 10.1016/j.tafmec.2017.02.012

Rathbun, H. J., Odette, G. R., Yamamoto, T. & Lucas, G. E. (2006) Influence of statistical and constraint loss size effects on cleavage fracture toughness in the transition - A single variable experiment and database. Engineering Fracture Mechanics, Volume 73, pp. 134-158.

Ruggieri C (2017) Low constraint fracture toughness testing using SE(T) and SE(B) specimens. Int J Press Vessel Pip 156:23–39 . doi: 10.1016/j.ijpvp.2017.07.003

Wallin, K. (2001) Quantifying Tstress controlled constraint by the master curve transition temperature T0. Engineering Fracture Mechanics, Volume 68, pp. 303-328.

Wallin, K. (2011) Fracture toughness of engineering materials - Estimation and application. Croydon: EMAS Publishing.

Wallin, K., Nevasmaa, P., Laukkanen, A. & Planman, T. (2004) Master curve analysis of inhomogeneous ferritic steels. Engineering Fracture Mechanics, Volume 71, pp. 2329-2346.

Wallin, K., Planman, T., Valo, M. & Rintamaa, R. (2001) Applicability of miniature size bend specimens to determine the master curve reference temperature T0. Engineering Fracture Mechanics , Volume 68, pp. 1265-1296.

Yamamoto, M. et al. (2015) International Round Robin Test on Master Curve Reference Temperature Evaluation Utilizing Miniature C(T) Specimen. Small Specimen Test Techniques ASTM STP 1576, Volume 6, pp. 53-69.

Zhu XK, Joyce JA (2012) Review of fracture toughness (G, K, J, CTOD, CTOA) testing and standardization. Eng Fract Mech 85:1–46

Appendix 3 - NKS-R BREDA-RPV

RESEARCH REPORT

VTT-R-00041-19

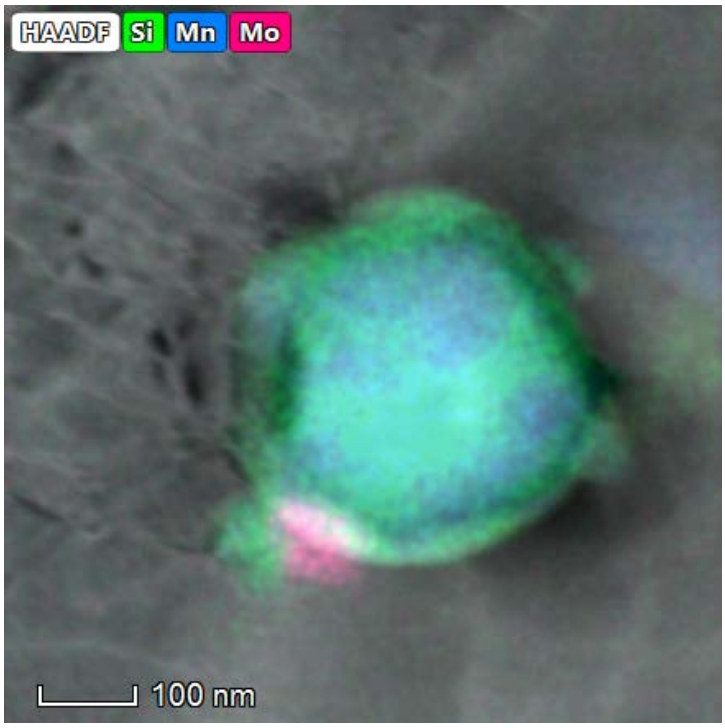

Microstructural characterization of non-irradiated Barsebäck RPV material: Transmission Electron Microscopy Study

Authors: Unto Tapper

Confidentiality: Restricted to SAFIR2018 and BREDA

Report's title

Microstructural characterization of non-irradiated Barsebäck RPV material: Transmission Electron Microscopy Study

Customer, contact person, address	Order reference
SAFIR2018, project THELMA	SAFIR 24/2017, 8.3.2017
Project name	**Project number/Short name**
Thermal ageing and EAC research for plant life management	117761 / THELMA
Author(s)	**Pages**
Unto Tapper	16/
Keywords	**Report identification code**
Pressure vessel steel, TEM, secondary particles	VTT-R-00041-19

Summary

Scanning transmission electron microscopy and X-ray spectroscopy was used to study second phase elemental composition in a Barsebäck RPV weld metal specimen. Five different frames were used to have an overview of the particulate material in the specimen. In addition, TEM foils were used to determine particle size distribution (PSD) using SEM.

Based on obtained elemental maps, four different types of particles by size and composition were observed:

1. Large oxide particles, with a size larger than 100 nm, whose composition is dominated by oxygen, aluminium and manganese.
2. Small Mo-rich particles with a size less than ~150 nm.
3. Small Mn-rich particles with a size less than ~150 nm.
4. Elongated Cr-rich particles that were located near or in the grain boundaries.

The Mo-rich particles are most probably carbides, although carbon was not detected here. The reason may be the used magnification, and the Mo-rich particles should be analysed using higher magnifications for confirmation of C.

The PSD had mean particle size 257 nm with 154 nm standard deviation. Median size was 246 nm indicating rather well peaked, non-lognormal PSD.

The results will be compared to further investigations in the SAFIR2022 BRUTE project, where the same material is investigated in irradiated condition.

Confidentiality	Restricted to SAFIR2018 and BREDA

Espoo 11.1.2019

Written by	Reviewed by	Accepted by
Unto Tapper Senior Scientist	Ulla Ehrnstén Principal Scientist	Sami Penttilä Research team leader

VTT's contact address

Kivimiehentie 3, P.O. Box 1000, FI-02044 Espoo

Distribution (customer and VTT)

SAFIR 2018 reference group 5, SAFIR2018 home page, BREDA advisory board, authors, YVL database, VTT archive (signed).

Preface

This report is a part of the SAFIR2018 THELMA project (Thermal ageing and EAC research for plant life management) and the work package on characterization of pressure vessel steel materials, and summarize results from transmission electron investigations on B2 weld metal.

As part of the larger BREDA-project (Barsebäck Research & Development Arena), mechanical testing of non-irradiated RPV material has been performed within the SAFIR2018 LOST project (Long term operation aspects of structural integrity project). The specimens used for testing were miniature C(T) specimens cut from Charpy type impact test specimens. The tested miniature C(T) specimens were then subject to microstructural characterization in the SAFIR2018 THELMA project. A separate report has been written on the microstructural results.

The specimens were delivered to the SAFIR2018 LOST project by Ringhals Ab, which is greatly appreciated. Also the funding from VYR (State nuclear waste fund), Technical Research Centre for Finland VTT, NKS (Nordisk Kärnsäkerhet) and Ringhals Ab is highly appreciated.

Further work is planned on irradiated and thermally aged B2 materials in the SAFIR2022 BRUTE project.

Espoo 15.1.2019

Authors

Contents

1. Introduction

This work is a part of the SAFIR 2018 THELMA, Thermal ageing and EAC (environmentally assisted cracking) research for plant life management, project, Work Package 3 “Microstructural characterization of reactor pressure vessel (RPV) steels”. In this work Barsebäck Unit 2 (B2) RPV non-irradiated reference state materials, i.e., base material (BM), heat-affected zone (HAZ) and weld metal (WM) was studied. The weld metal is a high-Ni material, and similar to the RPV weld metal in most Nordic NPPs. These investigations are a part of a larger entity, the Barsebäck REsearch&Development Arena, BREDA, aiming at an increased understanding of the correlation between surveillance data and data from the actual RPV weld after operation. An improved understanding of factors affecting brittle fracture initiation is another goal and this study serve this goal.

The investigations were performed on specimens, which were tested in the SAFIR 2018 LOST, Long term operational aspects of structural integrity, project. The studied materials are a part of the B2 surveillance program. The results from microstructural and fractography investigations have been reported in [1].

This report summarize the results obtained from Scanning Transmission Electron Microscopy and X-ray analyses carried on a HAZ specimen BGQ5.1. The elemental composition of selected particles were determined via elemental mappings in spectrum imaging mode where for each pixel in the image an X-ray spectrum was recorded. By using this method it is possible to obtain elemental composition of the individual particles by annotating the particle are in the image and integrating corresponding X-ray spectra in spectrum image data cube.

2. Material and specimen preparation

The specimen for transmission electron microscopy (TEM) analysis of elemental compositions of individual second phase particles was a heat affected zone (HAZ) specimen BGQ-1 used in SEM characterisation of the specimen. However, the specimens for this investigation was cut from the weld metal in the sample. A total of six approximately 300 mm thick foils were cut from the specimen using CBN blade equipped diamond wheel saw (Figure 1). The foils were then manually polished on both sides using # 1200 grit size SiC grinding paper prior to punching 3 mm diameter disks. The punched disks were polished to ~100 nm thickness before final thinning in Struers Tenupol™ twinjet electropolisher. A two mm mask and a solution of 7% perchloric acid in methanol at 45°C was used in Tenupol for final thinning.

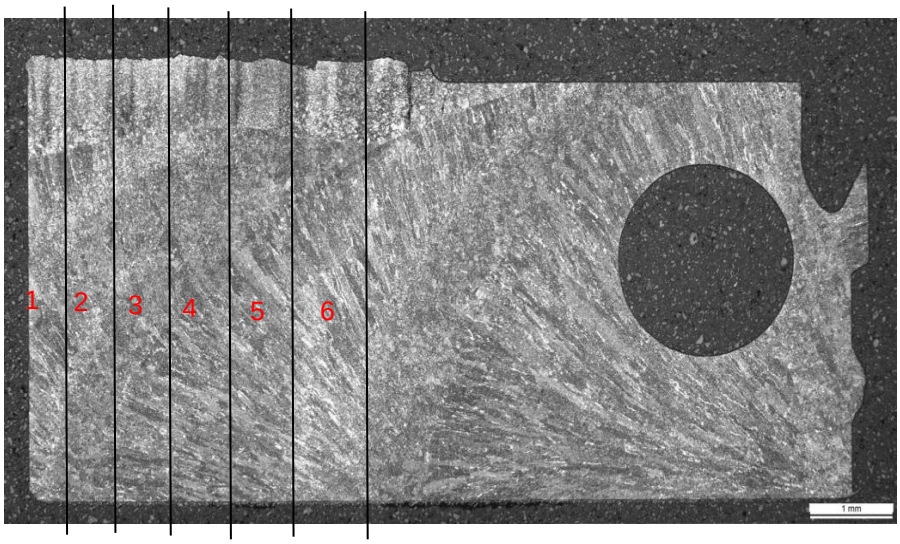

Figure 1. SEM specimen BGQ-1 used in the TEM analyses. Vertical lines indicate foils cut-out from the moulded SEM specimen. Foils 2 and 3 were used in the analyses.

3. Experimental

TEM analyses were conducted using a FEI TALOS F200X 200 kV field emission microscope in scanning mode (STEM). Electron imaging was done using a High Angle Annular Dark Field Detector (HAADF) which is providing images with atomic number contrast (some contrast due to diffraction is however visible depending on experimental conditions, e.g. camera length, convergence angle of the beam).

Energy dispersive X-ray spectra for elemental composition analyses were collected in “Spectrum Imaging” (SI) mode, where for each pixel in the image, an X-ray spectrum is recorded. Elemental composition analysis for individual particles were then post analysed by integrating X-ray spectra covering the particle area using an annotation tool provided by the software (Velox™). The X-ray detector (Super-X) in Talos is a special 4-detector assembly provided by Bruker/FEI.

Five different areas from the BGQ5.1 specimen were collected using 256x256 pixel resolution at modest magnifications (i.e. x100k – x400k range) to maximise the number of particles in the collected frames. Collection time varied between 15 to 30 minutes at ~1 nA probe current (measured from the “screen”).

Elemental composition of selected particles were determined by using annotation tool provided Velox software. The software integrates pixel wise corresponding X-ray spectra within annotated particle area. Quantification of elemental composition is then performed on the integrated spectrum. Iron was omitted from the quantification to better indicate composition of the analysed particles.

In addition to the STEM analysis, second phase particle size distribution was estimated from the SEM images obtained from two BGQ5.1 TEM foils. Particle size refers to an equivalent diameter of a disk that has the same area than the particle in the image. The microscope used in the analysis was a Zeiss 540 Crossbeam FEG SEM. Two TEM foils (BGQ5.1.2 and BGQ5.1.3) were used for particle size measurements and total of 130 individual particles were analysed.

4. Results

4.1 STEM and EDS results

Several particles were observed in the first frame, Figure 2. Both elongated and more spherical particles were observed. Based on the X-ray mapping and semi-quantitative results, Figure 3 and Table 1, the particles are of three types. These are, 1) one Mn- and Al-rich oxide particle containing also Mg, Si, Ti, Ni and Mo, which seems to be a combination of two overlapping particles 2) Mn-rich particles containing also C, Cr and Ni, and 3) Mo-rich particles containing also Mn and Ni. Based on the X-ray mapping, most of the Ni-signal comes from the matrix, and is not coupled with any specific particle.

Frame 2 contains spherical particles, Figure 4. Based on the X-ray mapping, Figure 5, and the semi-quantitative EDS-results, Table 2, almost all particles are Mn- and Al-rich oxide particles, containing also Mg, Si and Ti. They are thus similar with the type 1 particles above, although Mo was not detected in the particles in frame 2, further confirming that the Mn-Al-rich particle in frame 1 consists of two particles, one of which is Mo-rich. One of the particles in frame 2 is a Mo-rich particle, similar to the type 3 particle in frame 1.

Frame 3 contains also mainly spherical particles, Figure 6. The particles are of two distinctively different sizes. Based on the X-ray mapping, Figure 7, and the semi-quantitative EDS-results, Table 3, the larger particles are Mn- and Al- rich oxides, similar to type 1 in frame 1. The composition of the smaller particles was not determined, but based on the maps, they are mainly Mo- or Cr-rich.

Frame 4 is high-magnification frame of a spherical oxide, Figure 8, Figure 9 and Table 4. The X-ray map clearly shows that the particle is surrounded by a carbon rim. Further, the distribution of Si and Ti is uneven in the particle, suggesting that the particle is a conglomerate.

Frame 5 contain numerous particles, Figure 10. Based on the X-ray maps and the semi-quantitative EDS-results, the two larger particles are type 1 oxides, while the smaller particles partly Mn-rich and partly Cr-rich, Figure 11 and Table 5.

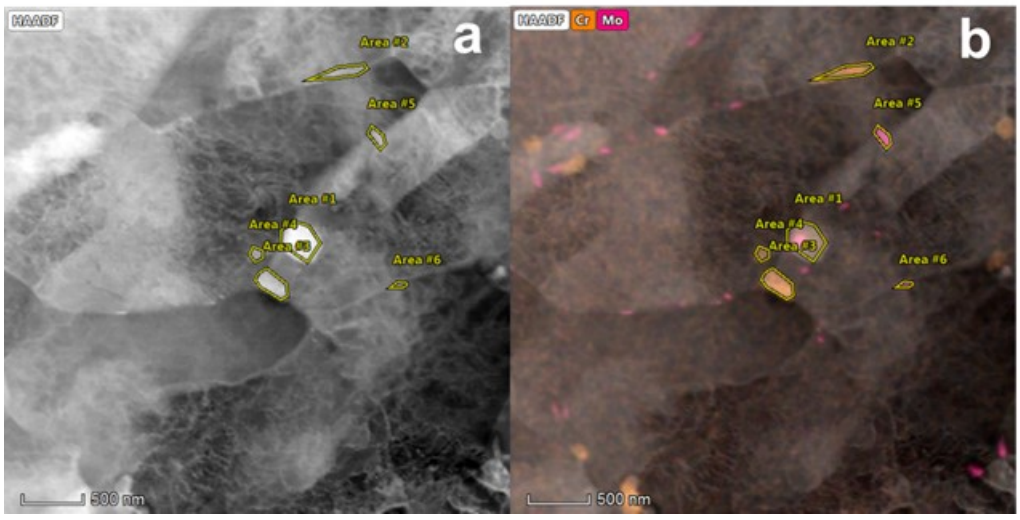

Figure 2. STEM/HAADF image of specimen BGQ5.1, frame #1. In a) is a HAADF image with annotated particle areas used for elemental composition determination. Note that some particles are not visible in HAADF image a) but in b) e.g. several Cr- and Mo-rich particles are visible based in the corresponding X-ray maps.

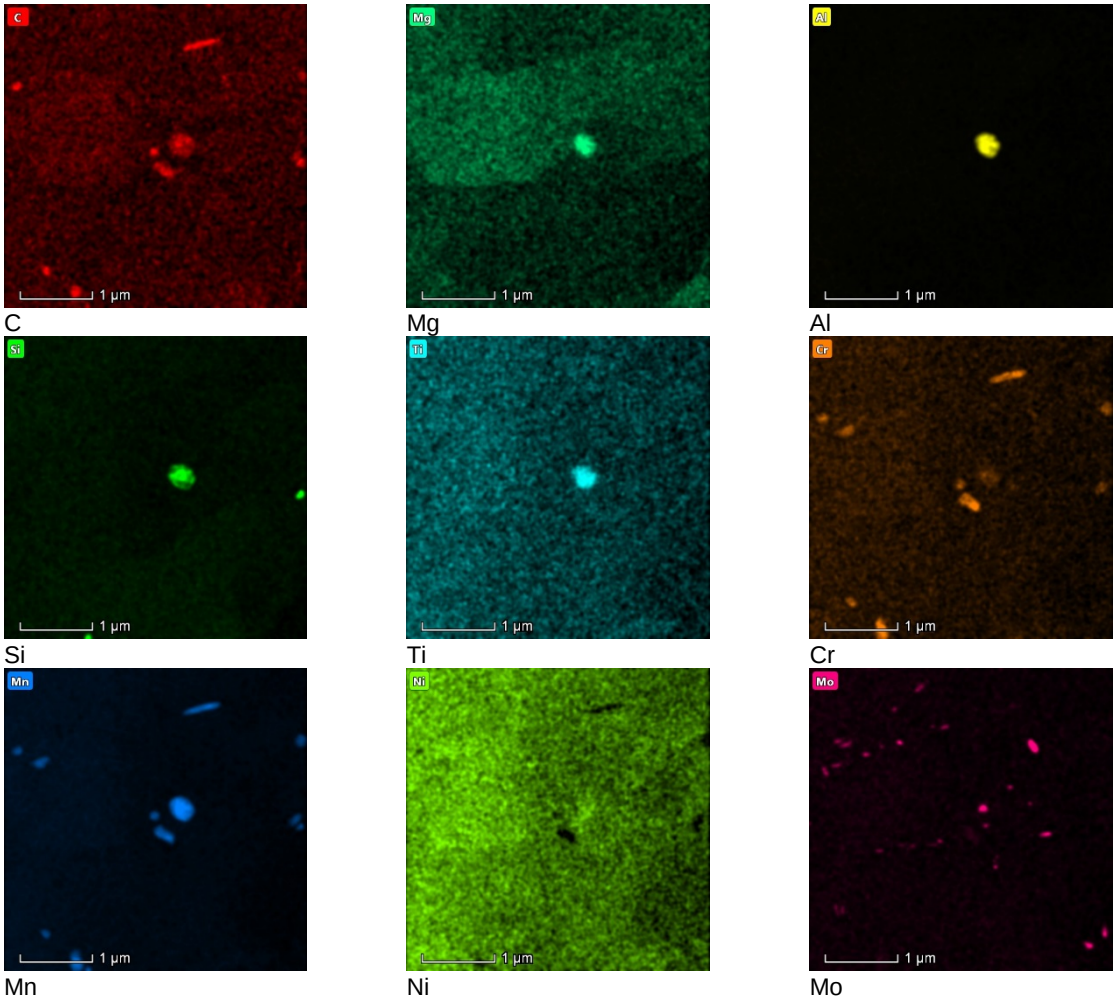

Figure 3. X-ray maps for identified elements in frame #1. Ni map shows that Ni is not coupled with particulate material but rather is a matrix element.

Table 1. Elemental composition for the particles annotated in Figure 1.

Area	C K	O	Mg K	Al K	Si L	Ti K	Cr K	Mn K	Ni K	Mo K
1[a]	-	36.76	0.74	22.01	5.55	0.94	0.50	27.52	2.47	3.52
2	-	3.41	-	-	-	-	10.92	75.36	4.42	4.44
3	7.88	3.29	-	-	-	-	11.69	67.56	3.74	4.02
4	10.66	4.04	-	-	-	-	6.68	63.36	6.49	5.59[b]
5	-	3.84	-	-	-	-	2.16	12.36	5.39	74.45
6	-	4.66	-	-	-	-	2.33	17.72	6.89	63.77

[a] Mo-rich particle ”under” larger particle. [b] Sulphur possible, Mo K-lines missing but clear peak at Mo L-line/S K-line. S content less than 1 % (0.82 %) if calculated as sulphur.

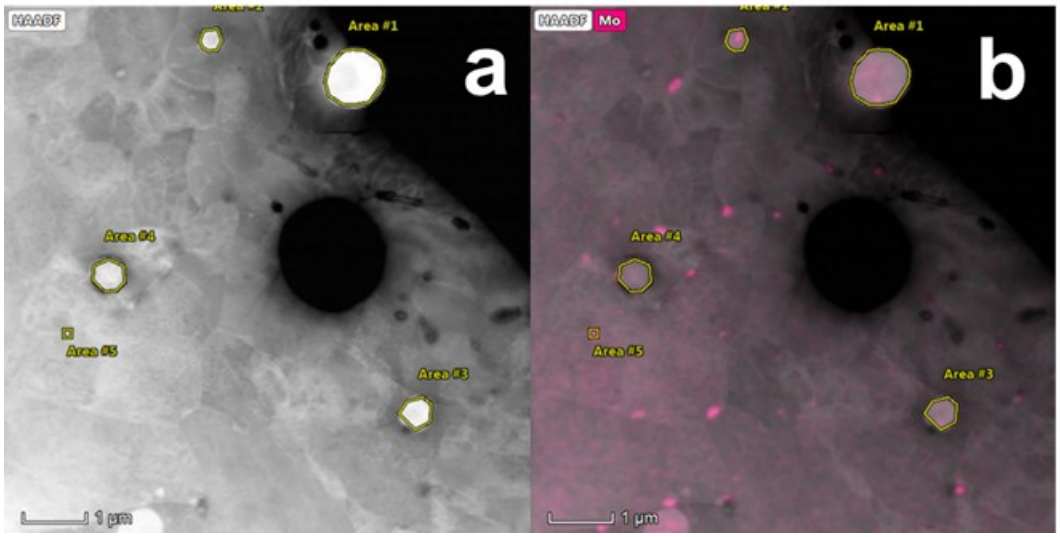

Figure 4. STEM/EDS spectrum imaging map of BGQ5.1specimen, frame #2. In a) is a HAADF image with annotated particle areas used for elemental composition determination. Note that some particles are not clearly visible in HAADF image (Fig.1a) but X-ray mapping (Fig 1b) shows several Mo-rich particles.

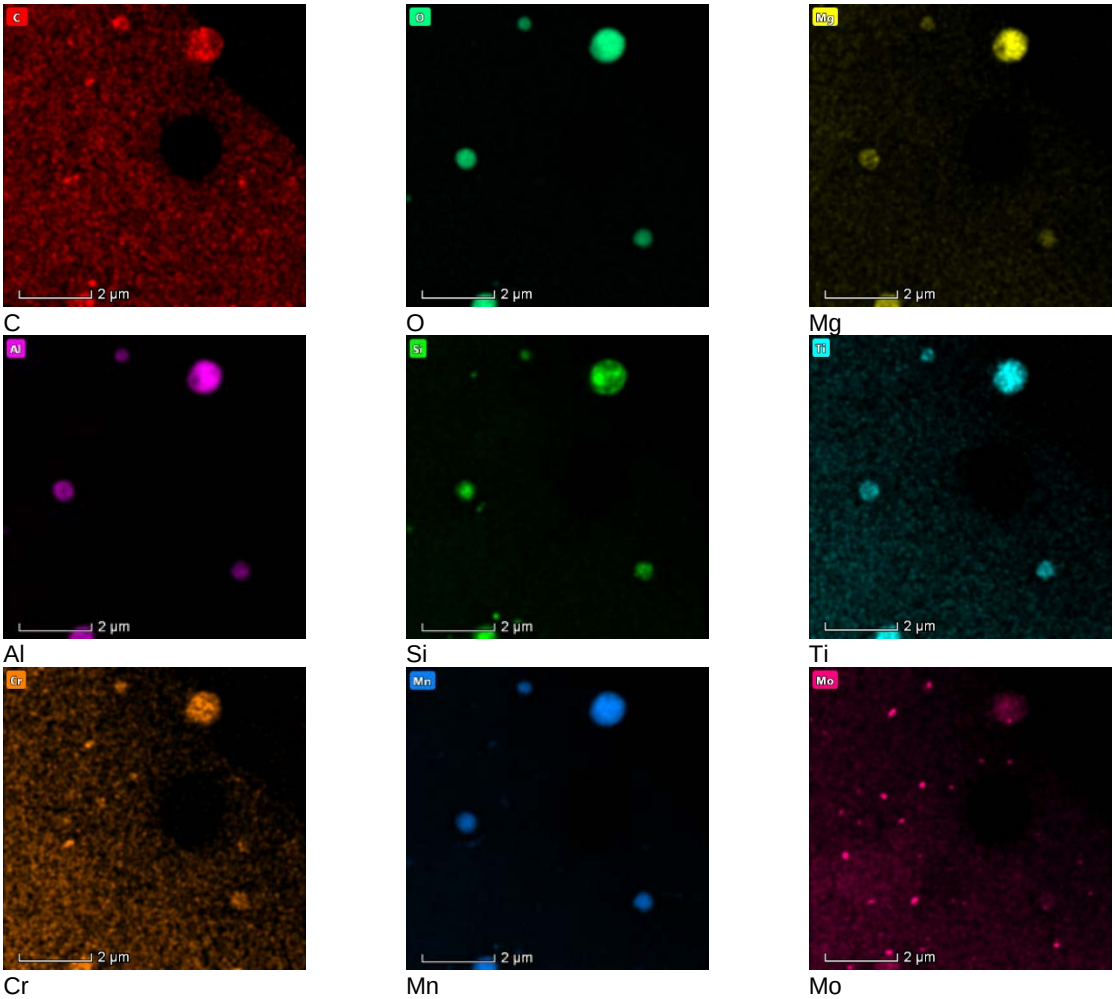

Figure 5. Elemental maps for frame #2. Large particles appear to be oxides, while the small particles are Mo-rich.

Table 2. Elemental compositions for the particles indicated in Fig. 4a.

Area	C K	O K	Mg K	Al K	Si L	Ti K	Cr K	Mn K	Fe K	Ni K	Mo K
1	-	34.54	1.99	27.25	5.59	0.21	-	28.22	-	-	-
2	-	35.55	0.85	23.50	3.97	1.35	-	31.75	-	-	-
3	-	32.29	0.83	21.38	6.44	1.40	-	35.53	-	-	-
4	-	38.19	0.96	25.53	6.24	1.30	-	26.67	-	-	-
5[a]	-	-	-	-	-	-	-	-	-	8.97	91.19

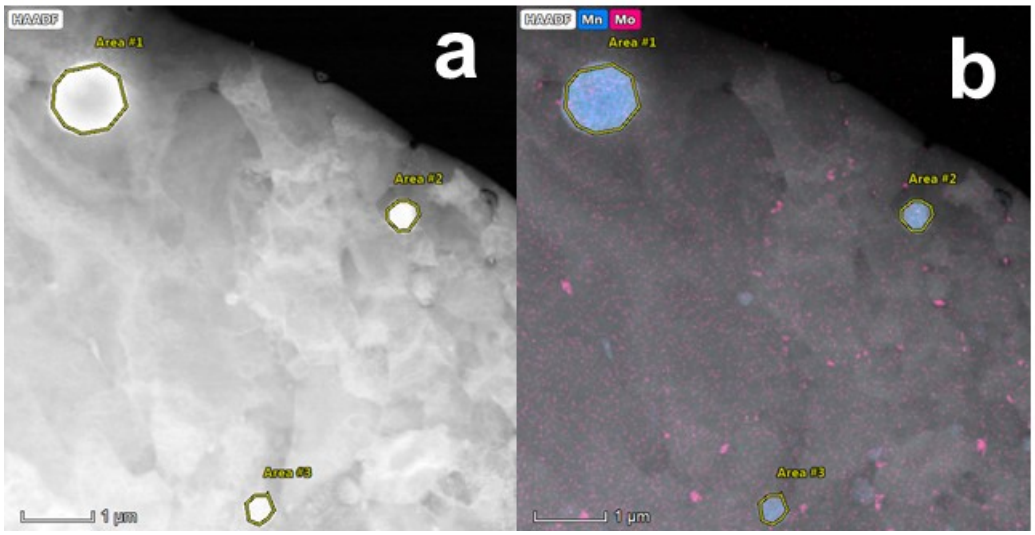

Figure 6. STEM/EDS spectrum imaging map of BGQ5.1specimen, frame #3. In a) is a HAADF image with annotated particles used in composition analysis. Several Mo-rich particles are visible based on X-ray signal (Fig. 1b).

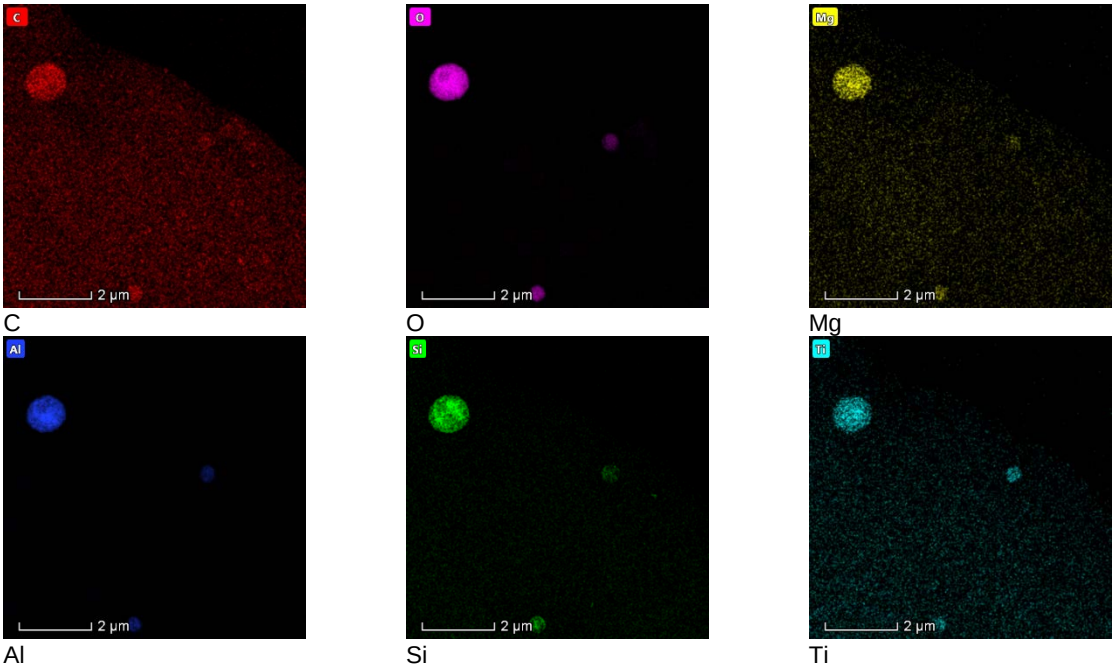

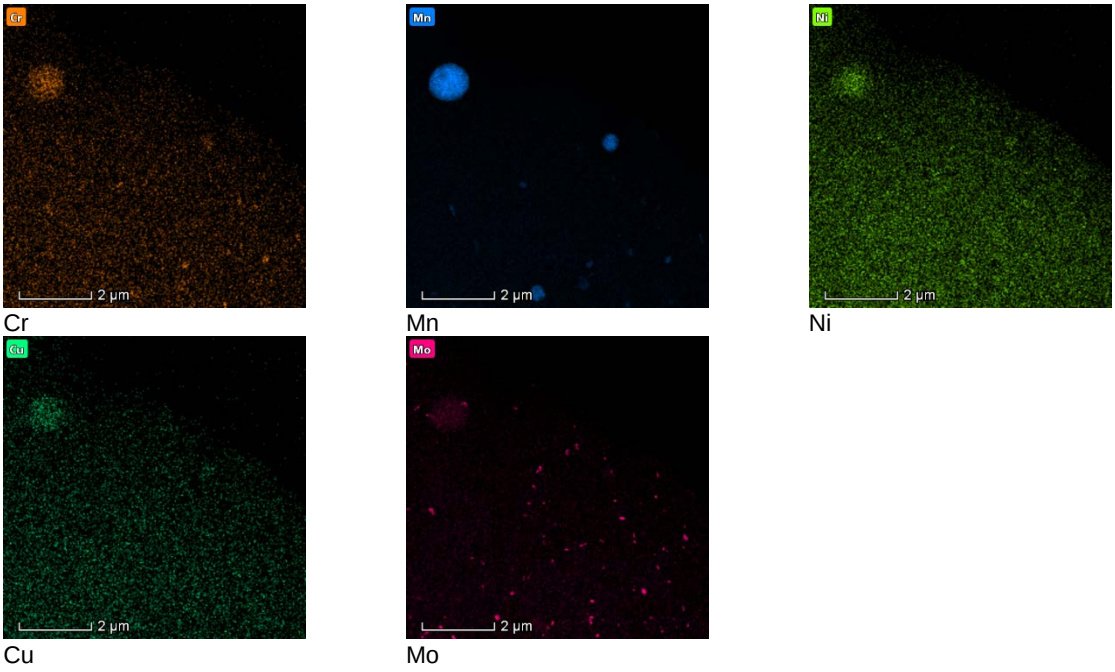

Figure 7. Elemental maps from frame #3. Typical, large particles in micrometre size-range with major components O, Al and Mn. Cr and Ti (as well C) maps show mainly statistical fluctuation. However, Ti and Cr seem to be present in large particles.

Table 3. Elemental composition of particles indicated in Figure 6.

Area	C K	O K	Mg K	Al K	Si L	Ti K	Cr K	Mn K	Ni K	Cu K	Mo K
1	-	34.19	1.05	26.15	6.16	1.39	-	28.87	1.11	0.26	-
2	-	26.46	-	19.55	3.05	2.29	-	44.35	1.84	-	-
3	-	36.58	1.11	20.64	6.17	1.05	-	30.45	2.17	-	-

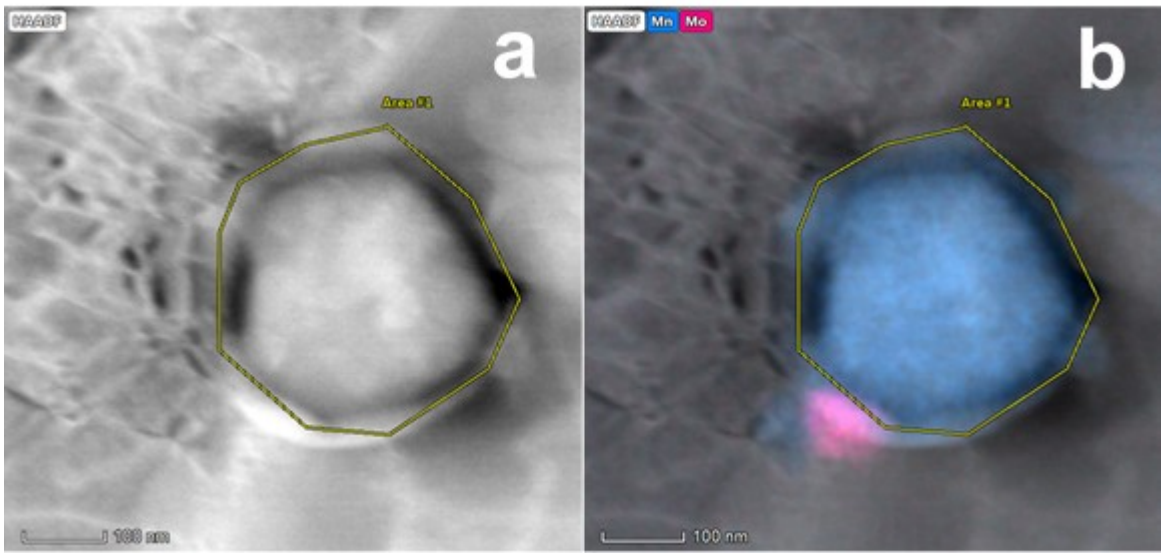

Figure 8. STEM/EDS spectrum imaging map of BGQ5.1 specimen, frame #4. In a) is shown HAADF image with an annotated particle area used for elemental composition determination. The Mo-rich particle in the lower left corner (Fig. 8b) is left out from chemical composition analysis.

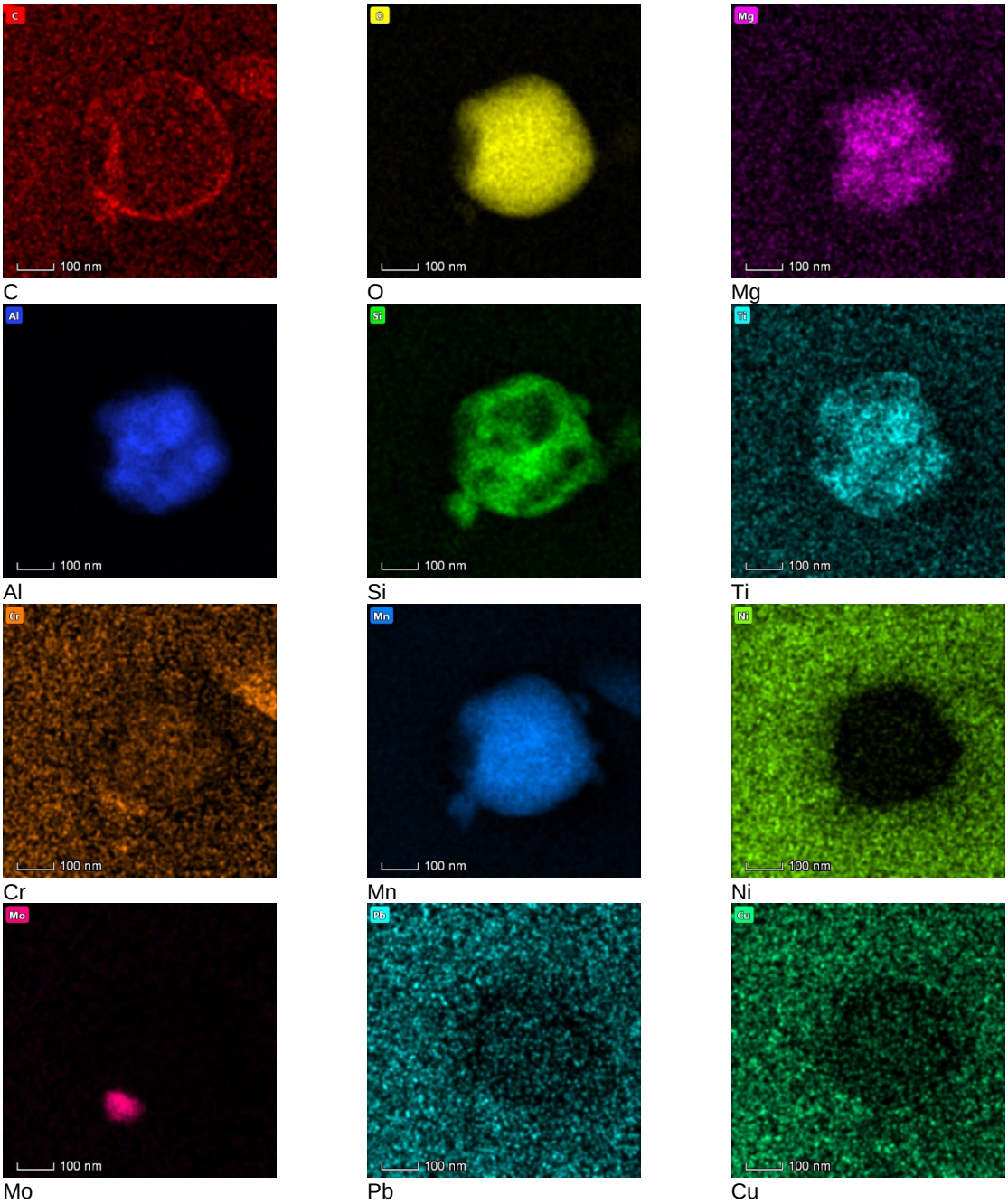

Figure 9. Elemental maps for frame #4. A carbon rim surrounds the oxide particle. Si and Ti maps show non-even distribution within the particle. Weak Pb and Cu peaks were also present but their maps indicate mainly statistical fluctuations.

Table 4. Chemical composition of the particle in Figure 8.

Area	C K	O K	Mg K	Al K	Si L	Ti K	Cr K	Mn K	Fe K	Ni K	Cu K	Mo K
1	1.27	36.63	0.92	21.31	6.77	1.22	-	30.84	-	0.16	0.10	0.34

Pb L-line peaks visible but not quantified by the software.

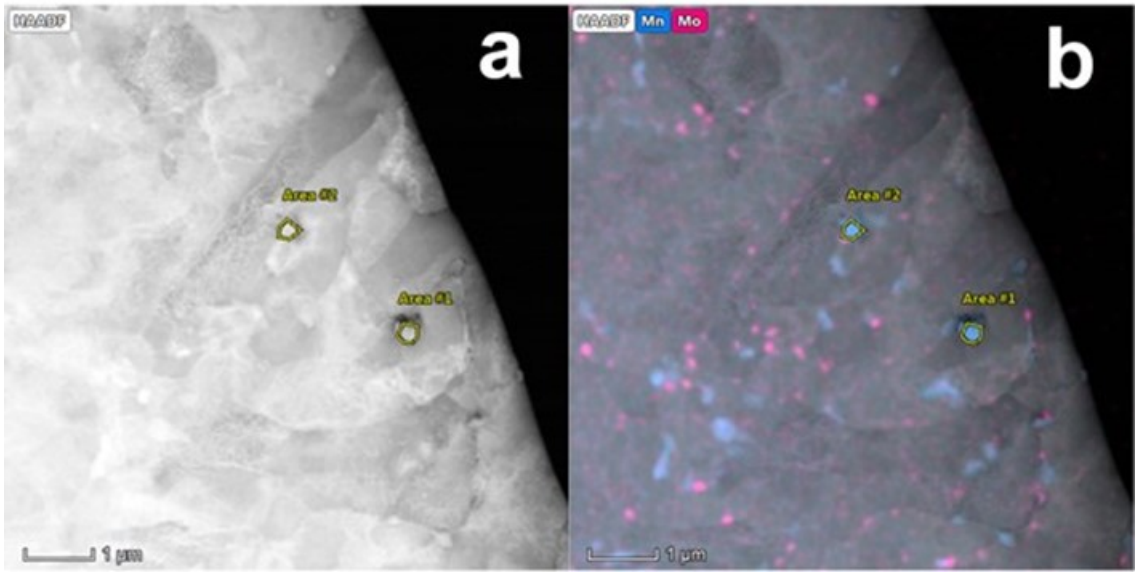

Figure 10. TEM-images from frame #5. In this area, several small Mn- and Mo-rich particles were observed. Analysed Mn-rich (Area #1 and Area #2) particles appeared to be coupled with presence of O and Al.

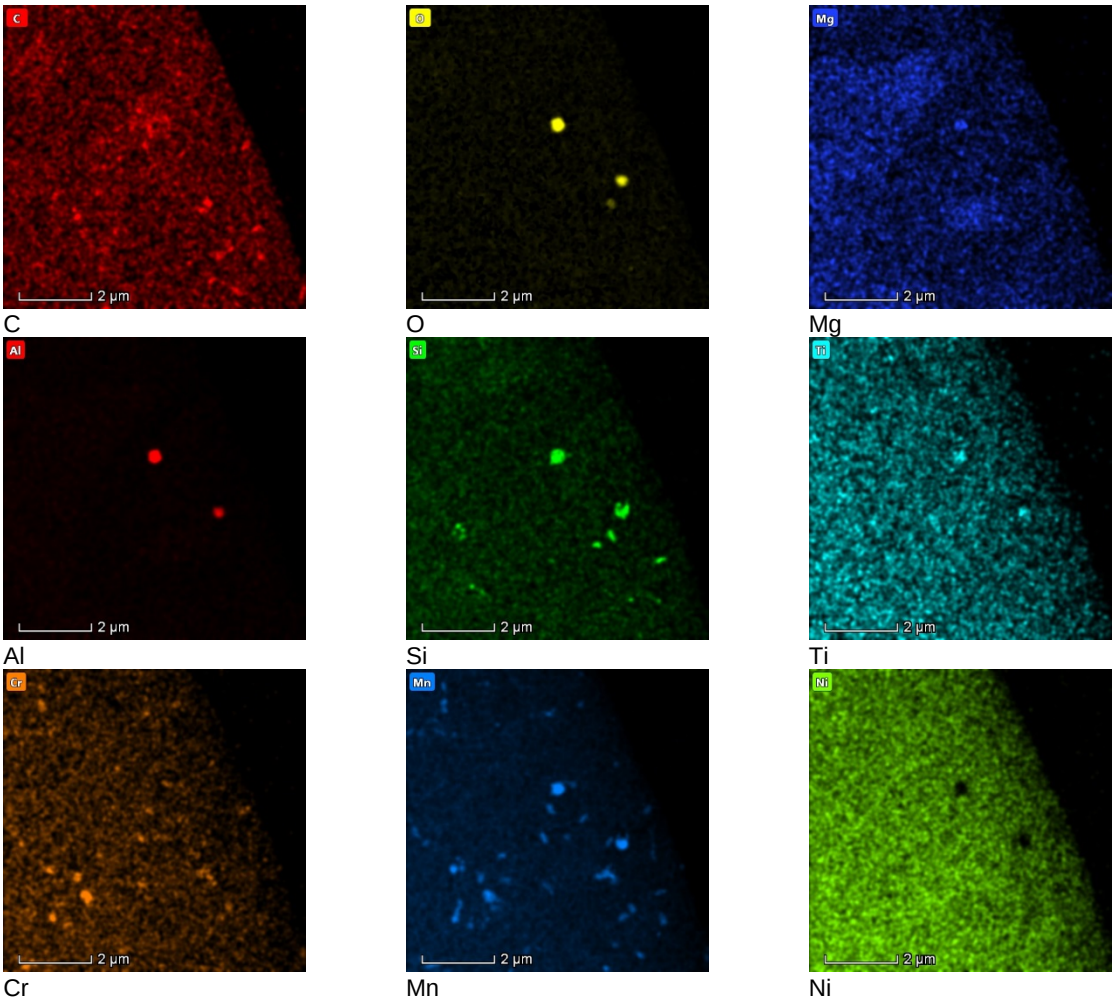

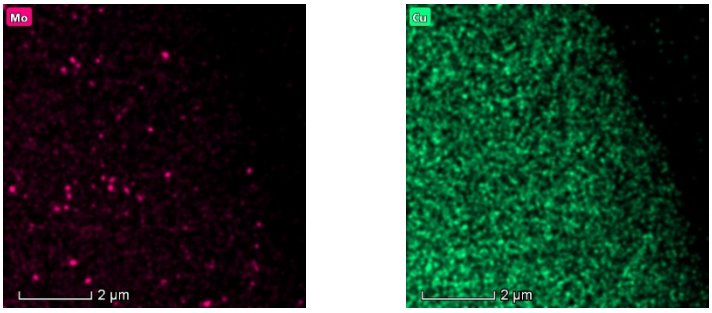

Mo Cu

Figure 11. Elemental maps from frame 5. Mg, Ni and Cu maps indicate only statistical fluctuation. Again, Mo-rich particles are not related with any other detected element and Mn is coupled with O, Al as well as Si and Ti. Cr is somewhat coupled with Mn-rich particles.

Table 5. Chemical composition of the particles indicated in Figure 10.

Area	C K	O K	Mg K	Al K	Si L	Ti K	Cr K	Mn K	Fe K	Ni K	Mo K
1	-	31.46	0.64	15.05	8.06	1.84	-	41.22	-	-	0.83
2	-	36.24	1.31	22.35	6.53	1.37	-	30.70	-	-	1.25

4.2 Particle size distribution

Several SEM images (~100) were obtained from TEM foils BGQ5.1.2 and BGQ5.1.3 to estimate second phase particles size distribution (PSD). One typical SEM micrograph used in the PSD determination is in Figure 12. In-lens detector with 15 keV electrons and 157 pA probe current were used for imaging at x5000 magnification. High-contrast in-lens secondary electron detector was used to collect size distribution micrographs. The number of pixels in the micrographs is 2048 x 2018 pixels.

Particle sizes were analysed using Digital Micrograph™ software by Gatan Inc. Totally 130 particles were analysed. The benefit of using SEM rather than TEM for particle size distribution measurements can be explained comparing Figure 12 to Figure 13: The TEM image is decorated with complex contrast structures greatly impeding particle extraction by grey scale thresholding. Such phenomena is not present in SEM.

The PSD had mean particle size 257 nm with 154 nm standard deviation. The median size is 246 nm indicating rather well peaked, non-lognormal PSD. It is known from microstructural investigations, that RPV weld can contain also particles in µm-scale, but the density of these is probably too small for any of these to be included in randomly prepared specimens.

The results show that the use of TEM foils in SEM to determine PSD of the second phase particles is a useful approach for PSD. In TEM, the number of particles that can be used in PSD determination is rather limited and a large number of specimens is needed to gather enough particle data. This is, of course, depending on the particle size of interest, which in this case is rather large in TEM-terms and therefore especially feasible for SEM.

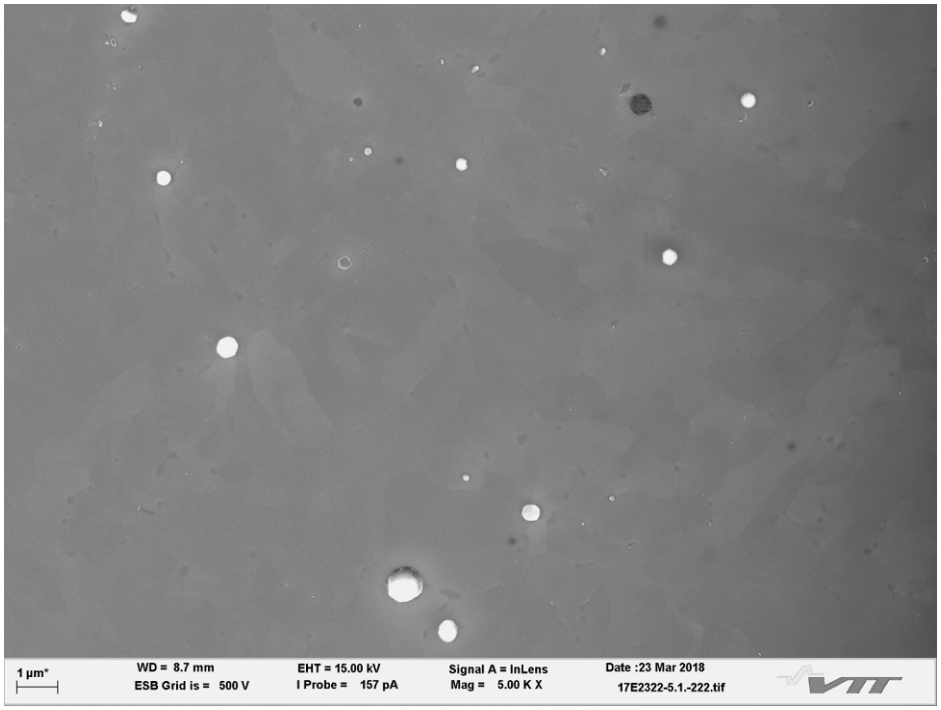

Figure 12. SEM image of the BGQ5.1.2 specimen showing several second phase particles. As compared to the TEM-picture in Figure 13, particles are often hidden under strong diffraction contrast features and therefore not readily analysed by software for particle size analysis.

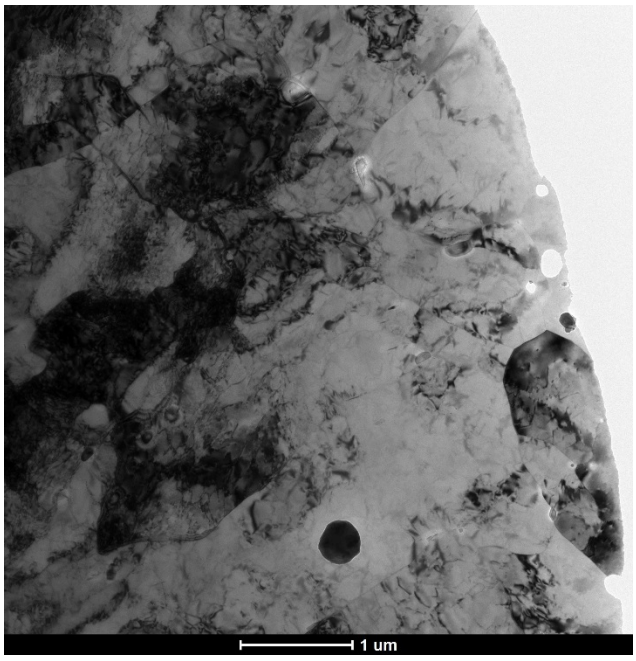

Figure 13. TEM image of the specimen BGQ5.1.2. Only few microns from the electropolished thin edge is possible to use in TEM analyses. Specimen becomes non-electron transparent within few microns from the specimen edge.

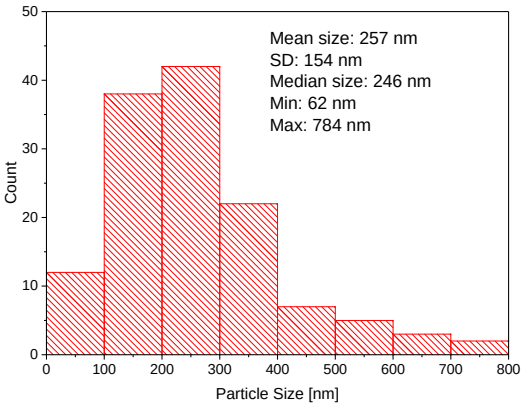

Figure 14. Particle size distribution measured from the SEM images. Mean particle size is 260 nm and median size 246 nm. SD 154 nm is the standard deviation of the mean.

5. Summary and discussion

Scanning transmission electron microscopy and X-ray spectroscopy was used to study second phase elemental composition in a Barsebäck RPV metal specimen prepared from heat affected zone (HAZ). Five different frames were used to have an overview of the particulate material in the specimen. In addition, TEM foils were used to determine particle size distribution (PSD) in specimen BGQ5.1 using SEM.

The elemental composition determination was conducted using TEM in scanning mode (STEM). The Talos instrument has better lateral resolution in STEM mode than in TEM mode. Therefore, use of STEM is preferred as it provides more versatile approach to individual particle analysis and is not resolution limited (the VTT TEM has atomic resolution in STEM mode).

Based on obtained elemental maps, four different major types of particles by size and composition were observed:

1. Large oxide particles, with a size larger than 100 nm, whose composition is dominated by oxygen, aluminium and manganese.

2. Small Mo-rich particles with a size less than ~150 nm.

3. Small Mn-rich particles with a size less than ~150 nm.

4. Elongated Cr-rich particles that were located near or in the grain boundaries. Otherwise, Cr was present in low concentrations and elemental maps are dominated by statistical fluctuation of chromium peak intensity.

Overlap of the Mo L-line and S K-line hampers identification of the elements separately. As the Mo K-line(s) were visible except in one case, the Mo/S peak was analysed as Mo.

The Mo-rich particles are most probably carbides, but here carbon was not possible to associate with Mo-rich particles. The reason may be the used magnification, and the Mo-rich particles should be analysed using higher magnifications for confirmation of C.

The PSD had mean particle size 257 nm with 154 nm standard deviation. Median size was 246 nm indicating rather well peaked, non-lognormal PSD. Based on the present understanding, use of TEM foils in SEM to determine PSD of the second phase particles is a

useful approach for PSD. In TEM, the number of particles that can be used in PSD determination is rather limited and a large number of specimens is needed to gather enough particle data.

References

[1] Lydman, J. Microstructural characterization of non-irradiated Barsebäck RPV base material and weld metal. VTT research report VTT-R-05125-18, 19.12.1.2018. 154p.